LUND UNIVERSITY

FACULTY OF ENGINEERING LTH

MASTER OF SCIENCE THESIS

Beamforming Solutions for Efficient Link Setup and Link Maintenance in Millimeter Wave Communication Systems

Authors:
Hesham SHARKAS (h.sharkas@ieee.org)
Haruhi ECHIGO (h5haruhily@gmail.com)

Academic Supervisor:
Professor Buon Kiong LAU

Industry Supervisor:
Dr. Dzevdan KAPETANOVIC

Examiner:
Associate Professor Fredrik RUSEK

A collaboration between

Department of Electrical and Information Technology
Huawei Lund Research Center

June 25, 2019

Printed in Sweden
Tryckeriet i E-huset, Lund

Abstract

Millimeter wave (mmWave band) technology has gained a lot of attention in 5G communications, due to large amounts of spectrum being available in the mmWave frequency range. However, mmWave links suffer from severe free-space loss and atmospheric absorption. Beamforming, which generates directed beams with strong gain using multiple antennas, is one promising solution towards these challenges.
In this thesis, we focus on designing beamforming weights (a codebook) to synthesize a new beam type, referred to as the "*Slepian*" beam. The width of the Slepian beam is tuneable, which enables the creation of a wider main-lobe with small side-lobes than the conventional Discrete Fourier Transform (DFT) beam. This makes it possible to optimize the beam for some optimization criteria. In particular, the interest is on the optimization of spectral efficiency and outage capacity over the coverage area (i.e., an angular sector). Using the Slepian beam, the angular space can then be quantized into sub-regions, where each sub-region is covered by a shifted version of the beam. Using wider beams to cover wider sub-regions instead of narrower sub-regions reduces the overhead on both the beam tracking and beam sweeping algorithms, with the latter achieving a reduced initial access time. The new codebook is then used for beam sweeping, and the beam sweeping algorithm implemented and evaluated in this work is hierarchical beam sweeping. Simulation results and capacity analysis verify that the proposed codebook design improves spectral efficiency and outage capacity.

Acknowledgements

We would like to express our deep gratitude to Dr. Dzevdan our supervisor in Huawei Lund Research Center for all the trust and patience he gave us throughout this thesis work, as well as for all the guidance and support he provided during both the research and the writing, besides his valuable revision as the first reader of this thesis. We thank all our colleagues in Huawei Lund Research Center who inspired us in our research. Working for Huawei Lund Research Center, not only developed and enhanced our research skills, but also boosted our ping-pong skills, which make our experience there all the more memorable.

Nevertheless, we also would like to express our sincere thanks to Professor Buon our supervisor in Lund University for all the care he gave us, and directing us. We acknowledge him as the second reader of this thesis, and we are gratefully indebted to him for his very valuable revision and comments on this thesis. We thank all our professors in Lund University for professionally teaching us the latest knowledge in the field of Communication Systems. Studying at Lund University, School of Engineering (LTH) was a fun knowledge-rich journey, and is valuable in our resumes.

Hesham and *Haruhi*

Preface

This thesis is the joint work of two students (Hesham and Haruhi), and the individual contribution of each student is specified in this section. The table below lists the chapters and appendices of the thesis, and how each student has contributed to them. For completeness, the contribution of the industrial supervisor (Dzevdan) is also stated in the table.

Chapter/ Appendix	**Contributions in research**	**Contributions in writing**
Abstract	Hesham and Haruhi	Hesham and Haruhi
Chapter 1	Technical Background, HW Architecture - Hesham Objective, Problem Definition - Dzevdan	Hesham Hesham and Haruhi
Chapter 2	Antenna Array Architecture - Hesham and Haruhi Synthesis Methods - Hesham Beam Sweeping - Hesham and Haruhi	Hesham
Chapter 3	Codebook Design - Hesham and Haruhi Angular/Phase Domains - Hesham and Haruhi Slepian Beam - Hesham and Haruhi Properties of the Slepian Beam - Hesham Comparing Slepian to other Synthesizers - Hesham Minimum Squared Error as a Metric - Haruhi	Hesham and Haruhi Hesham and Haruhi Hesham and Haruhi Hesham Hesham Hesham
Chapter 4	All sections of Capacity Analysis - Hesham	Hesham
Chapter 5	Simulation done on *System Simulator* - Dzevdan	Hesham
Chapter 6	Conclusion and Future Work - Hesham	Hesham
Appendix A	Calculations - Hesham	Hesham
Appendix B	Calculations - Hesham	Hesham
Appendix C	Calculations - Hesham	Hesham

Popular Science Summary

In future 5G systems that apply millimeter waves, an important requirement for mobile devices is fast connection to a tower. This can be either the setup of an initial connection, or the re-connection after the loss of the current connection. This requirement implies that the mobile device should find a strong enough incoming signal from the tower as fast as possible. This thesis project aims at solving this problem by designing a so-called codebook and algorithms that make use of it. They can be used in future 5G mobile phones to enable the phones to direct their signal towards (or receive the tower signal from) a certain direction, so they can establish the best wireless link with the tower. For example, imagine that you are in a dark room, and want to check the time on a clock hanging on the wall. Using a bulb will illuminate not only the clock, but the whole room, whereas using a flashlight can illuminate the clock only, but with a brighter light ray, and avoid sending the light everywhere unnecessarily. In wireless networks, this example translates into that the mobile focuses its radiated power towards the tower upon transmission, which increases the power gain and avoids disturbing other devices in the system. Similarly, it also translates into the mobile focusing its receiving beam in the direction of the desired signal from the tower, increasing its receiving gain and also avoiding interference from other devices that transmit at the same time. Phone manufacturers enable this feature by equipping the phone with multiple antennas that can collaborate to form a narrower beam and steer the beam to scan the surrounding space. In particular, this happens in the receiving path by capturing the same signal in all the antennas, and weighting each signal from each antenna with some weight that changes the signal's amplitude and/or phase, resulting in that the signals that come out of different antennas add up in the desired direction, and cancel one another otherwise. These sets of weights are stored in a codebook that represents different beam widths and directions. The techniques that decide the values of these weights are called beam synthesizers. Many beam synthesizers have been proposed in the past. In this thesis project, we propose a new beam synthesizer, and compare it with other beam synthesizers analytically and by system simulation. The results show that the new beam synthesizer gives significant data rate improvements under certain interference scenarios. The comparison is done against a metric called signal to noise and interference ratio (SINR) as well as the data rate. SINR is an indication of how much power of the desired signal has been delivered, relative to how much power of non-desired interferences plus noise is collected. The beam design as well as the system simulation were done in MATLAB.

Keywords: 5G, Beamforming, Beam Management, Beam Searching, Beam Sweeping, Codebook, Initial Access, MIMO, Millimeter Wave, Precoding, Slepian Beam, Synthesizer.

Contents

List of Figures x

List of Tables xi

List of Abbreviations xiii

List of Symbols xiii

1 Introduction 1
- 1.1 Technical Background . . . 1
- 1.2 Hardware Architecture . . . 3
- 1.3 Objective and Motivation . . . 4
- 1.4 Problem Definition . . . 4
- 1.5 Limitations . . . 4
- 1.6 Structure of the Thesis . . . 4

2 Theory 5
- 2.1 Antenna Array Architecture . . . 5
- 2.2 Synthesis Methods . . . 6
  - 2.2.1 DFT . . . 7
  - 2.2.2 Binomial . . . 8
  - 2.2.3 Dolph-Chebyshev . . . 8
- 2.3 Beam Sweeping . . . 9
  - 2.3.1 Exhaustive Beam Sweeping . . . 9
  - 2.3.2 Iterative Beam Sweeping . . . 10

3 Methodology I: Codebook Design and Optimization 13
- 3.1 Codebook Design . . . 13
  - 3.1.1 Sweeping Algorithm . . . 13
  - 3.1.2 Formulating Beam Pattern Optimization Problem . . . 14
- 3.2 Introducing Slepian Beam as a Solution of the Optimization Problem . . . 15
  - 3.2.1 Moving from the Angular Domain to the Phase Domain . . . 16
  - 3.2.2 Slepian Beam . . . 17
  - 3.2.3 Properties of the Slepian Beam . . . 20

3.2.3.1 Scanning of Parameter W_v . . . 20
3.2.4 Comparing the Slepian Beam with other Beam Synthesizers . . 22
3.2.4.1 Slepian and DFT . . . 25
3.2.4.2 Slepian and Binomial . . . 25
3.2.4.3 Slepian and Chebyshev . . . 27
3.3 Selection of Free Parameters . . . 28
3.3.1 Minimum Squared Error as a Metric . . . 31

4 Methodology II: Capacity Analysis 35
4.1 Mean Capacity Bounds . . . 37
4.1.1 Upper Bound . . . 37
4.1.2 Lower Bound . . . 37
4.1.3 Approximation . . . 38
4.1.4 Relation between Upper/Lower Bounds and the Approximation 39
4.2 Comparison of Capacity Bounds . . . 40
4.3 Outage Capacity . . . 44

5 Simulation Results 45
5.1 Simulation Environment . . . 45
5.2 Simulation Figures . . . 46
5.2.1 Exhaustive/Hierarchical Beam Sweeping . . . 47
5.2.2 Slepian/DFT at UE . . . 49
5.2.3 Slepian/DFT at UE and BS . . . 50
5.2.4 Inter-Site Distance Effect . . . 55
5.2.5 Carrier Frequency Effect . . . 56
5.3 Simulation Results Summary . . . 57

6 Conclusion and Future Work 59
6.1 Conclusion . . . 59
6.2 Future Work . . . 60

A Integration of the Square of a Radiation Pattern in the Phase Domain 61

B Integration of the Inverse of a Radiation Pattern in the Phase Domain 63

C Mean Capacity Upper Bound of the DFT Beam in the Phase Domain 65

References 67

List of Figures

2.1 Conversion between Cartesian and spherical coordinate systems 6
2.2 yz-plane placed UPA 7
2.3 DFT synthesizer's radiation pattern 8
2.4 Binomial synthesizer's radiation pattern 9
2.5 Dolph-Chebyshev synthesizer's radiation pattern 10
2.6 Exhaustive beam sweeping procedure 11
2.7 Iterative beam sweeping procedure 12

3.1 Angular and phase domains 17
3.2 Maximization of area under the radiation pattern for a target region . . . 19
3.3 Slepian beam weights scan versus W_v 22
3.4 The Slepian beam radiation pattern scans versus W_v in the phase domain 23
3.5 The Slepian beam radiation pattern scans versus W_v in the angular domain 24
3.6 Phase distribution of the incoming signal and an interfering signal 25
3.7 Radiation patterns of DFT/binomial beams for different numbers of antenna elements. 26
3.8 Radiation patterns of a ULA that uses Slepian/DFT beams 26
3.9 Radiation patterns of a ULA that uses Slepian/binomial beams 27
3.10 Radiation patterns of Chebyshev beams for different attenuation values . 28
3.11 Radiation patterns of a ULA that uses Slepian/Chebyshev beams (7 antenna elements) 29
3.12 Radiation patterns of a ULA that uses Slepian/Chebyshev beams (10 antenna elements) 29
3.13 Radiation patterns of a ULA that uses Slepian/Chebyshev beams (16 antenna elements) 30
3.14 Radiation patterns of Slepian beams for different number of antenna elements. 30
3.15 Squared Error of Slepian using different number of antenna elements. . . 32
3.16 Slepian beam pattern of a UPA with $M_v = M_h = 6$, and $W_v = W_h = 0.25$. 33
3.17 Slepian beam pattern of a UPA with $M_v = M_h = 8$, and $W_v = W_h = 0.2$. 34

4.1 An arbitrary beam showing signal/interference regions. 36
4.2 Capacity and capacity bounds of the Slepian versus interference power. . 41

4.3 Comparison between capacity of Slepian beam and different beam synthesizers in a noise limited scenario ($M = 3$) 42
4.4 Comparison between capacity of Slepian beam and different beam synthesizers in a noise limited scenario ($M = 8$) 43
4.5 Comparison between capacity of Slepian beam and different beam synthesizers in an interference limited scenario ($M = 5$) 43

5.1 Exhaustive/hierarchical beam sweeping, 16 beams codebook at the UE . 48
5.2 Exhaustive/hierarchical beam sweeping, 81 beams codebook at the UE . 48
5.3 Slepian beams vs DFT beams at the UE. 64 DFT beams at the BS 50
5.4 Slepian beams vs DFT beams at the UE. 256 DFT beams at the BS . . . 51
5.5 Slepian beams vs DFT beams at the UE. 256 DFT beams at the BS . . . 51
5.6 Slepian beams vs DFT beams at UE side. 64 Slepian beams at BS 53
5.7 Slepian beams vs DFT beams at UE side. 256 Slepian beams at BS . . . 54
5.8 Slepian beams vs DFT beams at UE side. 256 Slepian beams at BS . . . 54
5.9 Slepian beams vs DFT beams at UE and BS 55
5.10 Slepian beams vs DFT beams at ISD = 80 meters 56
5.11 Slepian beams vs DFT beams at ISD = 200 meters 57
5.12 Slepian beams vs DFT beams at f_c = 5 GHz 58
5.13 Slepian beams vs DFT beams at f_c = 28 GHz 58

List of Tables

5.1 Simulation setup 46

List of Abbreviations

3GPP	**3**rd **G**eneration **P**artnership **P**roject
5G	**5**th **G**eneration cellular network technology
AoA	**A**ngle **o**f **A**rrival
BS	**B**ase **S**tation
CDF	**C**umulative **D**istribution **F**unction
CHB	**CH**e**B**yshev beam
CRS	**C**ell **R**eference **S**ignal
DFT	**D**iscrete **F**ourier **T**ransform
DL	**D**own **L**ink
DPSWF	**Discrete P**rolate **S**pheroidal **W**ave **F**unction
EVD	**E**igen**V**alues **D**ecomposition
IA	**I**nitial **A**ccess
ICT	**I**nformation and **C**ommunications **T**echnology
ISD	**I**nter **S**ite **D**istance
LB	**L**ower **B**ound
LOS	**L**ine **o**f **S**ight
mmWave	**M**illi**m**eter **W**ave
MSE	**M**inimum **S**quared **E**rror
NR	**N**ew **R**adio
O2I	**O**utdoor to **I**ndoor
PDF	**P**robability **D**ensity **F**unction
RF	**R**adio **F**requency
Rx	**R**eceiver
SE	**S**quared **E**rror
SINR	**S**ignal to **I**nterference and **N**oise **R**atio
SLP	**SL**e**P**ian beam
SNR	**S**ignal to **N**oise **R**atio
SS	**S**ynchronization **S**ignal
SVD	**S**ingular **V**alues **D**ecomposition
TR	**T**echnical **R**eport
Tx	**T**ransmitter
UB	**U**pper **B**ound
UE	**U**ser **E**quipment
UL	**U**p **L**ink
ULA	**U**niform **L**inear **A**rray
UMa	**U**rban **Ma**cro
UMi	**U**rban **Mi**cro
UPA	**U**niform **P**lanar **A**rray
UT	**U**ser **T**erminal

List of Symbols

Symbol	Name	Unit
$\mathbf{0}_{M\times N}$	$M \times N$ all zeros matrix	–
$\mathbf{1}_{M\times N}$	$M \times N$ all ones matrix	–
$\mathbf{a}$	steering vector	–
$\mathbf{a}_h$	steering vector of horizontal direction	–
$\mathbf{a}_v$	steering vector of vertical direction	–
AF	array factor	–
$\overline{C}$	mean capacity	bits/s/Hz
d_h	horizontal separation distance	m
d_v	vertical separation distance	m
$\mathbb{E}$	the expectation operator	–
f_c	carrier frequency	Hz
G	array gain (of radiation pattern)	–
$\mathbf{I}_{M\times M}$	$M \times M$ identity matrix	–
I_R	radiation pattern inside interference region	–
j	imaginary number ($\sqrt{-1}$)	–
k	wave number	m^{-1}
M_h	number of horizontal elements	–
M_v	number of vertical elements	–
N_0	noise variance	W
P_I	received power of interference signal	W
P_s	received power of desired signal	W
S_R	radiation pattern inside desired signal region	–
$\mathbf{v}$	weighting vector	–
$\mathbf{v}_h$	weighting vector of horizontal direction	–
$\mathbf{v}_v$	weighting vector of vertical direction	–
$\mathscr{B}$	region in the angular space	rad^2
ϕ	azimuth	rad
θ	zenith (elevation)	rad
λ	wavelength	m
λ_{max}	maximum eigenvalue of a matrix	–
ρ	transmitted signal power to noise power ratio	–

Chapter 1
Introduction

This chapter gives the technical background of this thesis work, and introduces the type of hardware platform that can make use of the new beam synthesizer proposed and evaluated in this thesis. After that, the problem definition, the motivation of the work, and the thesis objective are elaborated. General limitations and simplifications that are considered in this work are then listed. Finally, the structure of the thesis is introduced.

1.1 Technical Background

United States can increase its GDP by $100 billion with an increase of 10 additional broadband lines per 100 individuals (i.e., total of 30 million lines) [1]. Similarly EU Commission reported that 50 % of the economic growth in the European Union is driven by Information and Communications Technology (ICT) [1], [2]. Broadband Communications is regarded as a potent stimulus of economy [1]. To satisfy the expected growth in capacity demand, advanced 5G services are anticipated to provide significantly higher peak data rates and capacity than 4G networks [3].

Future 5G cellular systems are expected to support communication in mmWave frequencies (i.e., frequencies above 28 GHz), since those frequency contain a lot of unoccupied spectra which have good potential to provide very high data rates to users [4]. However, mmWave communication comes with a lot of new challenges that were not present in previous cellular deployments, such as high path loss, less signal scattering, rapid channel variation due to movement, rotation, blockage, etc. [4], [5]. One way to overcome high path loss in mmWave frequencies is to transmit and receive with high gain beamforming. For this, both the base station (BS) and the user equipment (UE) are equipped with several antenna elements.

To understand the high path loss in mmWave, the propagation characteristics at these frequencies were studied in [4] using theory and measurements in an anechoic chamber. The study uses the Friis transmission equation given by [6]

$$P_r = P_t + G_t + G_r + 20\log\left(\frac{c}{4\pi R f}\right)[dBm], \tag{1.1}$$

where P_r is the receive power in unobstructed free space, P_t is the transmit power, G_t and G_r are the transmit and receive antenna gains, respectively, R is the distance between the

transmitter and the receiver in meters, f is the carrier frequency, and c is the speed of light. For isotropic radiator and receiver (i.e., $G_t = G_r = 1$), the received power can be seen as inversely proportional to the frequency squared [4]. However, according to the *energy continuity equation*, changing frequency should not change delivered power. In fact, antenna gains are proportional to the frequency squared, given a fixed physical aperture size [4], [6], and assuming the antennas are perfectly matched for all frequencies. This was introduced in [6] as below

$$P_r = P_0 A_{eff} \tag{1.2}$$

where P_0 is the power flow per unit area of the incident field at the antenna. A_{eff} is the effective area of the antenna and from (1.2) is proportional to its power gain [6]. The effective area, however, is proportional to the square of the wavelength for common types of tuned radiators[1] [6], i.e., the antenna aperture shrinks as frequency increases [5].

Keeping a relatively fixed aperture size at a higher frequency increases the antenna gain, which can then compensate for the high path loss. One way to keep a fixed aperture size is using an array of antennas. The effective area of broadside arrays was found to be approximately equal to the actual area occupied by the array [6], [7]. The small wavelengths of mmWave frequencies facilitate the use of a large number of antenna elements in a compact form [4]. This antenna configuration is suitable for integration into the often compact UE. Not only does the usage of arrays increases power gain, but it also allows' highly directional beams to be synthesized, leading to large array directivity gains [4], which is called beamforming. As a conclusion, the study results in [4] reveals that the key parameters characterizing the propagation properties of the mmWave bands, such as the path loss exponent, are comparable to those of typical cellular frequency bands when the transmit and receive antennas are used to produce beamforming gains. Interestingly, the study in [5] expects the path loss to even decrease quadratically with increasing frequency for constant aperture sizes at both the transmit and receive antennas.

Beam alignment is another requirement when beamforming is used. Beamforming systems in mmWave frequencies need to find suitable transmit/receive directions at the transmitter and the receiver so that the communication link can be established and maintained. Typically, this is accomplished by using beam sweeping algorithm for the establishment of the connection - known as initial access (IA) - and using a beam tracking algorithm for the maintenance of the connection. Both algorithms use predefined and stored synthesized beam weights known as a *beam codebook*. Therefore, a well designed codebook is essential for efficient beam sweeping and beam tracking algorithms. An efficient beam sweeping algorithm is one that can find the best beam pair within a short time.

In this regard, algorithms from prior work were considered for beam sweeping. Exhaustive beam search was discussed in [8], [9]. In this algorithm, the BS sends reference signals using its different beams and the UE receives each of these reference signals using all its different beams. After performing measurements with these beam pairs (Tx/Rx beam pairs), the UE reports to the BS which transmit beam it prefers and records its

[1] These include radiators such as half-wavelength dipole. However, reflectors such as parabolic reflectors and horn are not included, as their effective areas are independent of frequency, and depend only on the projected area of the reflector.

own preferred one. Iterative (or hierarchical) beam searching [9], [10] first uses wide beams by BS and UE to find the best beam faster, and then further divide the beams to narrower beams before repeating the best beam search. This approach can be used to substantially reduce the number of measurements. The hybrid technique for IA proposed in [11] modifies on iterative beam searching by reversing the roles of BS/UE in the second searching stage, where the UE sends repeatedly on the uplink (UL) its preferred transmit beam, and BS receives on narrow beams and selects the one with the highest SINR. This further reduces IA time because the UE does not need to report measurements in the second stage.

As discussed above, narrow beams have high directivity gain and achieve higher link budget, however, they also increase IA time and complicate beam tracking. On the other hand, wider beams have less directivity gain and achieve less link budget, but they reduce IA time and simplify beam tracking. To find a beam width that balances between the two factors, a beam synthesizer that has adjustable beam width is required. Paper [12] proposed such beams by defining an ideal - but not achievable - beam, then finding the closest achievable beam to it using numerical search methods. In this thesis work, we start from the definition of the ideal beam in [12], formulate an optimization problem that leads to a new adjustable-width beam synthesizer. The properties of this beam synthesizer is investigated. The synthesizer is then used to generate codebooks with different sizes that are later evaluated in a MATLAB-based *System Simulator* for its impact on system performance.

1.2 Hardware Architecture

Beamforming can be processed either in the digital (refers to processing in the baseband) or analog (refers to processing in the RF) domains. Baseband processing needs a dedicated RF-chain for each antenna element, which is expensive and power consuming [4], but it allows for flexibility and better utilization of the spatial degrees of freedom (such as spatial multiplexing, spatial diversity, and beamforming gain) [13]. On the other hand, analog processing needs only an analog phase-shifter and/or gain controller for each antenna element [4], [12], and all are processed using a single RF-chain. This makes it cheaper and less power consuming, but less utilization of the spatial degrees of freedom is possible (only beamforming gain).

Hybrid beamforming is also used to balance between good utilization of the spatial domain on one hand, and reasonable cost and power consumption on the other hand [13]–[15]. In this case, every antenna element is connected to a phase-shifter and/or gain controller. In addition to that, groups of antennas are connected to different RF-chains. Number of RF-chains and number of antenna elements per RF-chain vary from design to design.

In this thesis, the considered hardware is one RF-chain, in addition to a phase-shifter and gain controller for every antenna element. Thus, analog beamforming is used and it is the expected setup during IA.

1.3 Objective and Motivation

The main objective of this thesis is to design a beamforming codebook that reduces IA time, and at the same time still achieves a relatively high link budget. Providing good solutions to this problem is of high importance to industry, and they can be implemented in future products to give good performance.

1.4 Problem Definition

The challenge is to minimize the time needed to perform beam sweeping at the UE side for IA, but still doing it in an efficient way that keep a relatively high link budget. It can also be seen as achieving a higher link budget given a fixed IA time. This is directly related to the connection establishment time, on one side, and the quality of the established link on the other side.

1.5 Limitations

The below limitations apply to this thesis:

- Mutual coupling among array elements is not considered.
- Antenna elements of arrays are considered to have isotropic radiation pattern. This applies to all the calculations in Chapters 2, 3 and 4. In Chapter 5, the simulation environment *System Simulator* uses isotropic radiation for antenna elements at the User Terminal (UT), but directive antenna elements at the BS. More details about setup of *System Simulator* can be found in Table 5.1.
- Phase domain is used instead of angular domain.

1.6 Structure of the Thesis

The rest of this thesis is organized in the following way. Chapter 2 provides review of theories that are essential background knowledge in order to achieve the goal of this thesis, as well as need to be reviewed by the reader before diving into the proposed solutions. Chapters 3 and 4 propose the methodology to solve the problem. Chapter 3 shows how the problem is formulated into an optimization problem and solved, and it further discusses the solution. In addition, the solution is further analyzed in Chapter 4. Chapter 5 shows the simulation results of this thesis work, and compares them to what was known/considered before. Finally, Chapter 6 summarizes and concludes this work, and suggests several research ideas as future work.

Chapter 2
Theory

This chapter presents the theoretical basis of this research work, and it needs to be reviewed by the reader in order to properly understand our proposed solutions. It starts by describing the antenna array architecture and the theory behind it. Then, some of the most common beam synthesizers are surveyed. Finally, two beam sweeping techniques widely considered for 5G are introduced.

2.1 Antenna Array Architecture

A uniform linear array (ULA) is a multi-antenna configuration where a number of identical antenna elements are placed along one dimension with equal separation distances. This form of antenna can resolve signals along one dimension in the space, but not two (i.e. either azimuth or zenith).
A uniform planar array (UPA) has elements placed along two dimensions, and can resolve signals coming from two dimensions in space. Separation distances between antenna elements are equal over each dimension.
In this thesis, array placement follows the 3GPP specification as follows;

- The conversion between Cartesian and spherical coordinate systems is shown in Figure 2.1. Angle $\phi \in [\frac{-\pi}{2}, \frac{\pi}{2}]$ refers to the *azimuth*, and angle $\theta \in [0, \pi]$ refers to the *zenith*. These ranges cover the hemisphere in front of the array (the positive direction of the x-axis). For UPA, the other hemisphere is just a mirror of the same radiation pattern and usually blocked due to the ground plane/phone material. For this reason, the space that this thesis is dealing with is defined as, $\mathscr{B}_{\phi,\theta} = [\frac{-\pi}{2}, \frac{\pi}{2}] \times [0, \pi]$.
- UPA is placed in the yz-plane in Cartesian coordinate with the x-axis pointing towards the broadside direction ($\phi = 0^o$ and $\theta = \frac{\pi}{2}$), as shown in Figure 2.2.

Based on this geometry, the phase differences between the elements when an impinging wave arrives at the UPA can be expressed by a steering vector. The steering vector of the horizontal direction (i.e., a ULA placed along the y-axis) is

$$\mathbf{a}_h(\phi,\theta) = \begin{bmatrix} 1 & e^{-jkd_h \sin\phi \sin\theta} & e^{-2jkd_h \sin\phi \sin\theta} & \dots & e^{-(M_h-1)jkd_h \sin\phi \sin\theta} \end{bmatrix}^T \tag{2.1}$$

whereas the steering vector of the vertical direction (i.e., a ULA placed along the z-axis) is

$$\mathbf{a}_v(\theta) = \begin{bmatrix} 1 & e^{-jkd_v \cos\theta} & e^{-2jkd_v \cos\theta} & \dots & e^{-(M_v-1)jkd_v \cos\theta} \end{bmatrix}^T \tag{2.2}$$

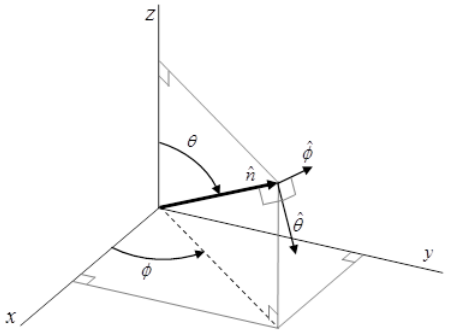

Figure 2.1: Conversion between Cartesian and spherical coordinate systems [Image source: 16].

where λ is the wavelength and k is the wave number and $k = 2\pi/\lambda$. M_v and M_h are the numbers of vertical and horizontal antenna elements (number of rows and columns as indicated in Figure 2.2), respectively. The resulting steering vector for the UPA is expressed using Kronecker product

$$\mathbf{a}(\phi,\theta) = \mathbf{a}_v(\theta) \otimes \mathbf{a}_h(\phi,\theta) \tag{2.3}$$

The weighting vector applied to the UPA is chosen to be of the same form as in (2.3). This weighting vector is what we refer to as a *"beam"* in this thesis and it is expressed as follows

$$\mathbf{v} = \mathbf{v}_v \otimes \mathbf{v}_h \tag{2.4}$$

where

$$\mathbf{v}_v = \begin{bmatrix} v_{v,0} & v_{v,1} & v_{v,2} & \cdots & v_{v,M_v} \end{bmatrix}^T \tag{2.5}$$

$$\mathbf{v}_h = \begin{bmatrix} v_{h,0} & v_{h,1} & v_{h,2} & \cdots & v_{h,M_h} \end{bmatrix}^T \tag{2.6}$$

2.2 Synthesis Methods

Throughout this thesis, we assume isotropic[1] antenna elements. Moreover, mutual coupling among array elements is neglected.
The array factor of a beam shows how a beam applied to an array influences the total radiation field, and it is given by

$$\begin{aligned} AF(\phi,\theta;\mathbf{v}) &= \sum_{m_v=0}^{M_v-1}\sum_{m_h=0}^{M_h-1} v_{m_v}^* v_{m_h}^* e^{-m_v jkd_v \cos\theta} e^{-m_h jkd_h \sin\phi \sin\theta} \\ &= \mathbf{v}^H \mathbf{a}(\phi,\theta) \end{aligned} \tag{2.7}$$

[1] This assumption applies to all the calculations in Chapters 2, 3 and 4. In Chapter 5, the simulation environment *System Simulator* uses isotropic radiation for antenna elements at the UT, but directive antenna elements at the BS. More details about setup of *System Simulator* can be found in Table 5.1.

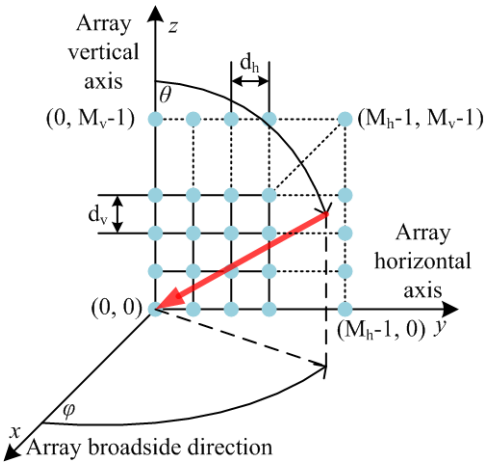

Figure 2.2: yz-plane placed UPA

The array directivity gain (or radiation pattern) is given by [12]

$$\begin{aligned} G(\phi,\theta;\mathbf{v}) &= \left|AF(\phi,\theta;\mathbf{v})\right|^2 = \left|\mathbf{v}^H\mathbf{a}(\phi,\theta)\right|^2 \\ &= \left|(\mathbf{v}_v \otimes \mathbf{v}_h)^H(\mathbf{a}_v(\theta)\otimes\mathbf{a}_h(\phi,\theta))\right|^2 \\ &= \left|(\mathbf{v}_v^H\mathbf{a}_v(\theta))(\mathbf{v}_h^H\mathbf{a}_h(\phi,\theta))\right|^2 \\ &= \left|(\mathbf{v}_v^H\mathbf{a}_v(\theta))\right|^2\left|(\mathbf{v}_h^H\mathbf{a}_h(\phi,\theta))\right|^2 \end{aligned} \tag{2.8}$$

where for the UPA, the array gain can be seen as a product of two ULA array gains. This will be used throughout this thesis to simplify calculations.
The selection of the weighting coefficients $\mathbf{v}_v$ and $\mathbf{v}_h$ controls the radiation pattern. Three common pattern synthesizers are described below.

2.2.1 DFT

In the DFT synthesizer, all the weights have the same magnitude of unity, and differ only in phase. It is given by

$$\mathbf{v}_{DFT} = \frac{1}{\sqrt{M_vM_h}}\mathbf{a}(\phi_0,\theta_0) \tag{2.9}$$

where ϕ_0 and θ_0 are the desired locations of the peak of the radiation pattern in azimuth and zenith, respectively. To normalize the total beam power regardless of the number of antenna elements, the weighting vector is normalized by its Frobenius norm, where $\|\mathbf{a}\|_2 = \sqrt{M_vM_h}$. The normalization ensures that $\|\mathbf{v}_{DFT}\|_2^2 = 1$.
The DFT radiation pattern shows the highest possible peak value which is equal to M_vM_h, but it also shows high side-lobes levels [17]. Figure 2.3 shows a DFT array radiation pattern.

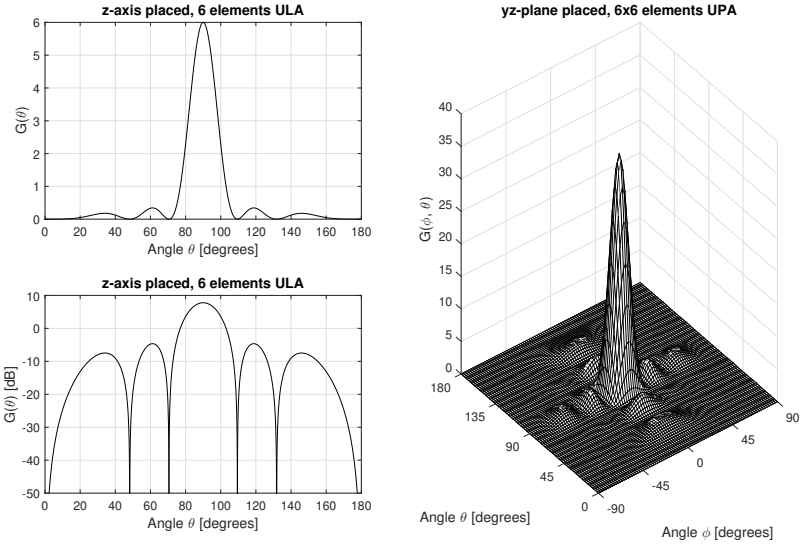

Figure 2.3: DFT synthesizer's radiation pattern.

2.2.2 Binomial

In the steering vector of a vertical[2] ULA (2.8), variable substitution may be used where $z = e^{-jkd_v \cos\theta}$. This makes the array factor of the vertical ULA a polynomial of z of degree $(M_v - 1)$. Binomial beam synthesizer places all the zeros of this polynomial at $\theta = 0$, equivalent to $z = -1$, giving a radiation pattern with no side-lobe, but a rather wide main-lobe [18]. The weighting vector $\mathbf{v}_v$ is obtained by expanding $(z+1)^{M_v-1}$ (this formula places all zeros at $\theta = 0$), then using the coefficients of the resultant polynomial as the weighting vectors, which are the same as in Pascal's triangle. The same approach is applied to the horizontal ULA, with the variable substitution $z = e^{-jkd_h \sin\theta \sin\phi}$. The weighting vector $\mathbf{v}$ of the UPA can be calculated using (2.3), and then normalized by its Frobenius norm, to ensure $\|\mathbf{v}\|_2^2 = 1$. Figure 2.4 shows a binomial array radiation pattern.

2.2.3 Dolph-Chebyshev

Dolph-Chebyshev synthesizer has radiation pattern with the narrowest main-lobe for a given side-lobe level [18]. It is the solution of an optimization problem that minimizes the side-lobe level. Let us assume θ_0 is the angle of the peak of the main-lobe and $\theta_m,\ m = 1,2,...,M-1$ are the angles of the peaks of the side-lobes. The optimization problem is written as below

$$\underset{\mathbf{v}_v:\ \|\mathbf{v}_v\|_1 \le 1}{\operatorname{argmin}} \left\{ \max_{m:\ \left|\mathbf{v}_v \mathbf{a}_v(\theta_0)\right| = 1} \left\{ \left|\mathbf{v}_v \mathbf{a}_v(\theta_m)\right| \right\} \right\} \tag{2.10}$$

[2]This applies also to a horizontal ULA using $z = e^{-jkd_v \sin\phi \sin\theta}$

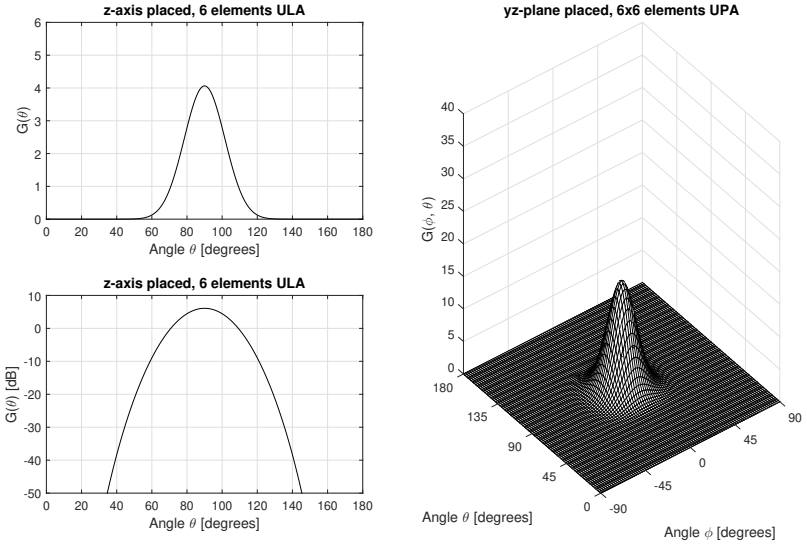

Figure 2.4: Binomial synthesizer's radiation pattern.

It targets to minimize the maximum side-lobe's peak. Under the constrain on the $l_1 - norm$, all side-lobe peaks become the same level in order to minimize the maximum one. Figure 2.5 shows a Dolph-Chebyshev array radiation pattern.

2.3 Beam Sweeping

Section 2.2 has shown some techniques for generating directive beams. This section shows how to sweep beams, searching for the direction with the largest SINR. To minimize computational complexity in the UE, a predefined codebook of weights (targeting predefined angles) is stored in the UE memory. The selection of the weights must guarantee coverage of the whole space $\mathscr{B}$ (defined by ranges of ϕ and θ in Section 2.1). In addition, it needs to reduce IA time, which is the main challenge of this work, as mentioned in Section 1.4. The largest SINR beam pair for UE and BS is estimated by transmitting synchronization signal (SS) blocks repeatedly by the BS and receiving them by the UE that reports back the SINR measurements to the BS. By the end of this procedure, both sides know the best beam that should be used out of its own codebook [19]. Two sweeping algorithms are discussed below.

2.3.1 Exhaustive Beam Sweeping

A conventional method to search for the best beam is exhaustive searching, where all possible combinations of beam pair from the BS and UE codebooks are checked [11]. In this algorithm, the BS uses the first beam from its codebook and sends SS blocks over the downlink (DL). The number of SS blocks should be equal to the number of beams

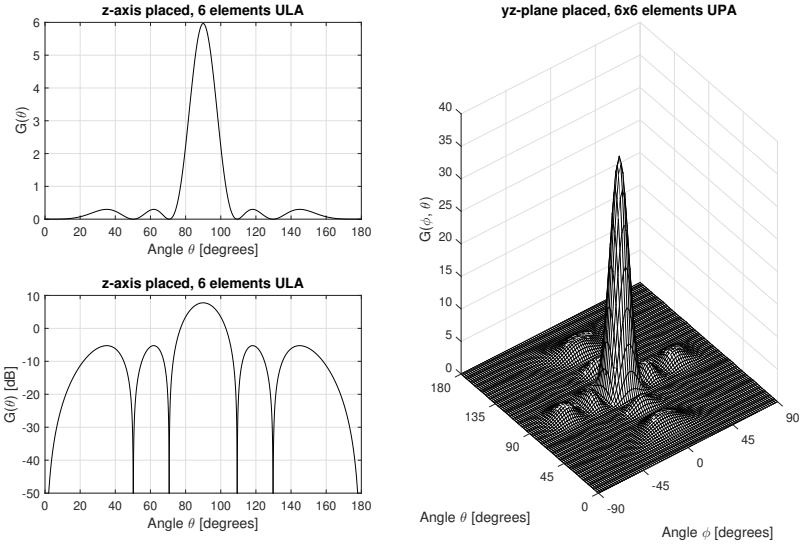

Figure 2.5: Dolph-Chebyshev synthesizer's radiation pattern, with the side-lobe level 13 dB less than the main-lobe peak.

at the UE codebook. The UE uses all beams from its codebook one by one to receive the SS blocks. The UE stores the beam which achieves the best SINR measurement and reports back over the uplink (UL) this measurement to the BS. The BS in turn stores that measurement with its own corresponding beam. This round is repeated for all beams in the BS codebook. Finally, the BS determines its best beam based on the reported SINR, and so does the UE. The procedure of exhaustive beam sweeping is illustrated in Figure 2.6. The total time slots needed for exhaustive search is [11]

$$T_{Ex} = D_{BS} \times (D_{UE} + 1) \tag{2.11}$$

where D_{BS} and D_{UE} are the number of beams in the BS and UE codebooks, respectively. The 1 added to D_{UE} in (2.11) is for the SINR reporting over the UL. It can be seen that the number of beams in the UE/BS codebooks are directly proportional to the IA time.
As seen in this algorithm, the UE repeats the same steps for each beam in the BS codebook. **As this thesis work targets the UE side only, the exhaustive search considers only one round (i.e., one beam in the BS codebook) and the UE sweeps all beams in its codebook to find the best beam.**

2.3.2 Iterative Beam Sweeping

In this algorithm, the codebook does not consist of only one set of beams that together cover the whole space $\mathscr{B}$. Instead, it consists of multiple sets of beams, where each set covers $\mathscr{B}$, but with different number of beams and different beam widths. For example, in the case of 3 sets, set 1 may have 4 wide beams covering $\mathscr{B}$. Then set 2 may have 16

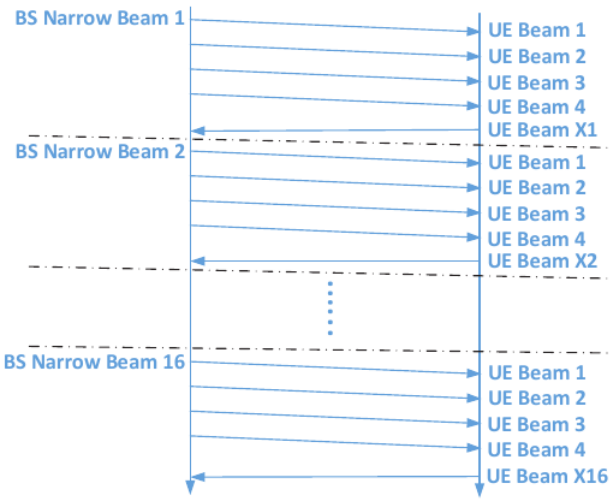

Figure 2.6: Exhaustive beam sweeping procedure. 16 beams in the BS codebook, and 4 beams in the UE codebook [Image source: 11].

narrower beams also covering $\mathscr{B}$, and finally set 3 may have 64 narrowest beams covering $\mathscr{B}$. Each set is referred to as a stage. Now by executing exhaustive sweeping using stage 1 beams, the best beam of stage 1 is found. Then in stage 2, it is enough to sweep (using exhaustive search again) stage 2 beams that fall in the sub-space covered by the best beam from stage 1. The same applies when moving to stage 3. The output of stage 3 is the best narrowest beam that can be used. This iterative technique can be applied to the codebooks at the BS as well as UE to reduce the number of measurements/time slots required to cover the space $\mathscr{B}$.

Figure 2.7 shows the procedure for a BS with four wide beams in stage 1 and 16 narrow beams in stage 2, and a UE with 4 beams and a single stage. In the first stage, the BS sends reference signals on each of the four beams. For each beam out of the four, the UE scans using its four beams. The best measurement the UE can find corresponds to a beam at the UE and a beam at the BS, so the UE reports to the BS over the UL the preferred beam at the BS side. In the second stage, the UE only listens to the preferred beam at its side, and the BS further divide the preferred wide beam at its side to 4 narrow beams, and sends reference signals on each one. The UE reports back to the BS every measurement of the four beams. Finally, the BS uses the best beam out of the four and the link is established. In this case, the required number of time slots for the two stages is [11]

$$T_{It} = D_{BS_{stage1}} \times (D_{UE} + 1) + (D_{BS_{stage2}} / D_{BS_{stage1}}) \times 2 \tag{2.12}$$

where $D_{BS_{stage1}}$ and $D_{BS_{stage2}}$ are the number of wide beams and narrow beams at the BS, respectively, and D_{UE} is the number of beams at the UE. It can be seen that the IA time is directly proportional to the number of beams and the number of stages in the UE/BS codebooks.

Once again, the UE repeats the same steps for each beam coming from the BS. **As this**

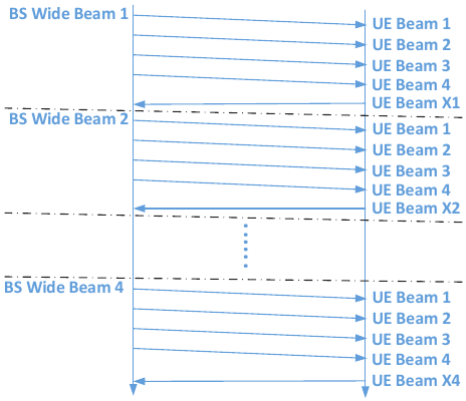

(a) Stage 1

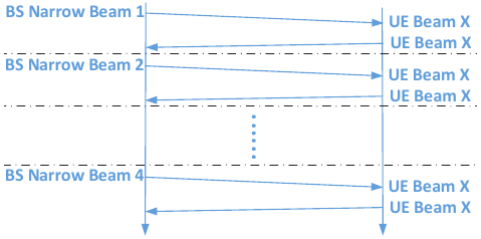

(b) Stage 2

Figure 2.7: (a) Iterative beam sweeping procedure. 4 wide beams in the BS codebook stage 1, and 4 beams in the UE codebook. (b) 4 narrow beams used from the BS codebook stage 2 that correspond to the selected wide beam in stage 1, and 1 beam used from UE codebook (The best from stage 1). [Images source: 11].

thesis work targets UE side only, the procedure will be reduced to only one beam coming from the BS, and the UE sweeps beams over different stages in its codebook to find its best corresponding beam.

Chapter 3

Methodology I: Codebook Design and Optimization

This chapter introduces the codebook design and the approach to reduce IA time. The approach leads to an optimization problem, which is solved using what is here called *"Slepian beam"*. The rest of the chapter derives the solution, lists some properties of the mentioned beam, and compares the obtained beam pattern with the three common beam synthesizers described in Chapter 2.

3.1 Codebook Design

As described in Chapter 2, a codebook is a predefined set of weighting vectors that generate some radiation patterns. The pattern main-lobe is shifted to point to a predefined set of angles that covers the whole space $\mathscr{B}$. The design of the codebook can be summarized as;

- Dividing $\mathscr{B}$ into discrete regions $\mathscr{B}_{q,p}$ that need to be covered. Each region is characterized by its center angles ϕ and θ. Regions may or may not overlap.
- Designing a radiation pattern that covers, in an efficient way, a single region. Create shifted versions of the pattern to cover all regions.

The way to use the codebook highly influences how the codebook should be designed. In Subsection 3.1.1 the sweeping algorithm that uses the codebook is decided. Based on that, the requirements on the codebook are stated. Then, Subsection 3.1.2 converts these requirements to a solvable optimization problem.

3.1.1 Sweeping Algorithm

Two sweeping algorithms have been discussed in Section 2.3. By comparing (2.11) with (2.12), it is clear that iterative sweeping achieves shorter IA time than exhaustive sweeping. For example, a BS with 16 beams and a UE with 4 beams need 80 time slots to do exhaustive beam searching. If the BS switches to a 2-stage hierarchical search with 4 beams per stage (i.e., the second stage has same beam number and width as the exhaustive search), it only needs 28 time slots. For this reason, iterative sweeping is considered in the design of the codebook. The number of stages and number of beams per stages are adjustable in the written MATLAB code.

It is also shown that the IA time is directly proportional to the number of beams in the UE codebook. One requirement on the codebook design is to try to reduce the number of beams by dividing the space $\mathscr{B}$ into regions that do not overlap. This means that each beam covers its own region - not only a specific angle - without overlapping regions. This leads to the requirement that radiation pattern should aim to efficiently cover a region and not only achieve a high peak at the main-lobe. In addition to that, the pattern is required not to cover other regions. The next section explains that more.

3.1.2 Formulating Beam Pattern Optimization Problem

The optimization problem introduced in (2.10) attempts to maximize the difference between the *peak point* of the main-lobe and the *peak point* of the highest side-lobe. This approach is good when it is guaranteed that the peak point of the beam's main-lobe is perfectly aligned to the incoming signal. This case requires a large (over-sampled) codebook with overlapped regions leading to a longer IA time and also requires a very efficient tracking algorithm.
Therefore, an optimization problem can be proposed here that optimizes the beam performance for a given region. The parameter that reflects the beam performance is chosen to be the mean capacity. According to [12], the mean capacity of a beam is

$$\overline{C} = \mathop{\mathbb{E}}_{\phi,\theta}\left\{ \log_2\left(1+\rho\|\mathbf{h}\|_2^2 G(\phi,\theta;\mathbf{v})\right) \mid \rho,\|\mathbf{h}\|_2^2 \right\} \tag{3.1}$$

where ρ is the transmitted signal power to noise power ratio, and $\|\mathbf{h}\|_2^2$ is the channel gain. Both are assumed constants as we are interested in studying the effect of the radiation pattern on the mean capacity.
The function $\log_2(1+x)$ is concave since it has a second derivative $-1/((1+x)^2\ln 2)$ which is always negative. Moreover the singularity at $x=-1$ is avoided as the radiation pattern is always non-negative[1]. Hence, Jensen's inequality can be applied to obtain an upper bound as below

$$\overline{C} \le \log_2\left(1+\mathop{\mathbb{E}}_{\phi,\theta}\left\{\rho\|\mathbf{h}\|_2^2 G(\phi,\theta;\mathbf{v})\right\} \mid \rho,\|\mathbf{h}\|_2^2\right) \tag{3.2}$$

The target region $\mathscr{B}_{q,p}$ is covered by the radiation pattern $G(\phi,\theta;\mathbf{v})$. Because the incoming signal can fall anywhere inside the target region, the received signal gets amplified by the gain of the beam pattern based on its angle of arrival (AoA). Assuming AoA has a uniform distribution over $\mathscr{B}_{q,p}$ and is zero outside, the expectation can be calculated as

$$\begin{aligned} \overline{C} &\le \log_2\left(1+\frac{P_s}{N_0}\mathop{\mathbb{E}}_{\phi,\theta}\left\{G(\phi,\theta;\mathbf{v})\right\}\right) \\ &= \log_2\left(1+\frac{P_s}{N_0}\frac{\iint_{\mathscr{B}_{q,p}} G(\phi,\theta;\mathbf{v})\,d\phi\,d\theta}{\iint_{\mathscr{B}_{q,p}} d\phi\,d\theta}\right) \end{aligned} \tag{3.3}$$

where the multiplication of the channel gain $\|\mathbf{h}\|_2^2$ and the transmitted signal power to noise power ratio ρ are replaced by the received signal power to noise power ratio P_s/N_0.

[1] As it is the square of the array factor, so the curve is always positive, with $(M-1)$ zeros.

The double integral in the numerator yields the total volume under the beam pattern surface bounded by $\mathscr{B}_{q,p}$. The double integral in the denominator yields a constant that represents the area of the region $\mathscr{B}_{q,p}$.
Using Parseval's theorem [20] under the constraint $\|\mathbf{v}\|_2^2 = 1$, the volume under the radiation pattern surface is constant over the space $\mathscr{B}_e = [-\pi,\pi) \times [-\pi,\pi)$, and for $d_v = d_h = \lambda/2$, where λ is the wavelength, the volume equals [12]

$$\iint_{\mathscr{B}_e} G(\phi,\theta;\mathbf{v}) d\phi d\theta = \int_{-\pi}^{\pi}\int_{-\pi}^{\pi} \left|\mathbf{v}^H \mathbf{a}(\phi,\theta)\right|^2 d\theta d\phi = (2\pi)^2 \|\mathbf{v}\|_2^2 = (2\pi)^2 \tag{3.4}$$

In [12] an ideal beam has been assumed that concentrates the constant volume integrated across $\mathscr{B}_e$ into the region of interest $\mathscr{B}_{q,p}$. This maximizes the upper bound given in (3.3). Furthermore, the beam pattern is constant inside $\mathscr{B}_{q,p}$, which makes the mean capacity $\overline{C}$ reach the upper bound (Jensen's equality holds). In other words, because the beam pattern is constant inside the region $\mathscr{B}_{q,p}$ from where the signal comes, the signal is amplified with the same gain. Besides, the beam is zero elsewhere, which suppresses any interference and avoids unnecessary overlaps with other regions. However, such a beam is not achievable in practice because it needs an infinite number of antenna elements[2]. The rest of [12] attempts to find the closest beam to the ideal one considering a limited number of antenna elements. Closeness is measured using the squared error.
For a limited number of antenna elements, neither the whole volume integrated over $\mathscr{B}_e$ can be concentrated inside $\mathscr{B}_{q,p}$, nor can the beam pattern be perfectly constant inside. In this thesis, the Slepian's *Prolate Spheroidal Wave Functions* [21], [22] which have been reported in [23] to have benefits in beamforming, are proposed as a solution that maximizes the volume concentration inside a given $\mathscr{B}_{q,p}$. Moreover, this solution is still applicable to a finite number of antenna elements. Maximizing the volume maximizes the upper bound given in (3.3). The rest of this chapter introduces the Slepian beam, and capacity analysis of the beam is presented in the next chapter.

3.2 Introducing Slepian Beam as a Solution of the Optimization Problem

Let's have a look at the integration in the numerator in (3.3). Substituting by (2.8) gives

$$\begin{aligned}\iint_{\mathscr{B}_{q,p}} G(\phi,\theta;\mathbf{v}) d\phi d\theta &= \iint_{\mathscr{B}_{q,p}} \left|\mathbf{v}_v^H \mathbf{a}_v(\theta)\right|^2 \left|\mathbf{v}_h^H \mathbf{a}_h(\phi,\theta)\right|^2 d\phi d\theta \\ &= \int_{\theta} \left|\mathbf{v}_v^H \mathbf{a}_v(\theta)\right|^2 \int_{\phi} \left|\mathbf{v}_h^H \mathbf{a}_h(\phi,\theta)\right|^2 d\phi d\theta \end{aligned} \tag{3.5}$$

In (3.5) $\mathbf{v}_h$ can be used to maximize the inner integration across ϕ, whereas $\mathbf{v}_v$ can be used to maximize the outer integration across θ. However, the inner integration will results in that the outer integration becomes a totally different expression compared to the expression one obtains when integrating the vertical ULA beam pattern. This makes it impossible to express (3.5) as the integration across two independent ULAs. For now, we only consider

[2]Fourier expansion of a rectangle shape pulse requires infinite number of terms and coefficients

a ULA placed over the vertical dimension, (3.5) can be reduced to

$$\int_{\theta}\left|\mathbf{v}_v^H\mathbf{a}_v(\theta)\right|^2 d\theta = \int_{\theta}\mathbf{v}_v^H\mathbf{a}_v(\theta)\mathbf{a}_v^H(\theta)\mathbf{v}_v d\theta = \mathbf{v}_v^H\Big(\int_{\theta}\mathbf{a}_v(\theta)\mathbf{a}_v^H(\theta)d\theta\Big)\mathbf{v}_v \tag{3.6}$$

Let $\psi_v = jkd_v\cos\theta$. The integrand is the following matrix

$$\mathbf{A}(\theta) = \mathbf{a}_v(\theta)\mathbf{a}_v^H(\theta) = \begin{bmatrix} 1 & e^{\psi_v} & e^{2\psi_v} & \dots & e^{(M_v-1)\psi_v} \\ e^{-\psi_v} & 1 & e^{\psi_v} & \dots & e^{(M_v-2)\psi_v} \\ e^{-2\psi_v} & e^{-\psi_v} & 1 & \dots & e^{(M_v-3)\psi_v} \\ \vdots & \vdots & \vdots & \ddots & \vdots \\ e^{(1-M_v)\psi_v} & e^{(2-M_v)\psi_v} & e^{(3-M_v)\psi_v} & \dots & 1 \end{bmatrix} \tag{3.7}$$

A closer look at one of the matrix elements - for instance the element $e^{\psi_v} = \cos(kd_v\cos\theta) + j\sin(kd_v\cos\theta)$ - shows that its integral does not have a known closed form because of the nested trigonometric functions.
Because of the two reasons above[3], a work around will be used, which is to move from the angular domain to the so called phase domain, which is introduced in the next subsection.

3.2.1 Moving from the Angular Domain to the Phase Domain

As in [12], we introduce two new parameters $s_v = \cos\theta$, and $s_h = \sin\theta\sin\phi$. As $\theta \in [0,\pi]$, then $s_v \in [-1,1]$. Similarly, as $\theta \in [0,\pi]$ and $\phi \in [\frac{-\pi}{2},\frac{\pi}{2}]$, then $s_h \in [-1,1]$. However, as s_h is a function of both θ and ϕ, this adds one more constraint as below

$$s_v = \cos\theta \quad \Longrightarrow \quad s_v^2 = \cos^2\theta$$

and

$$s_h = \sin\theta\sin\phi \quad \Longrightarrow \quad s_h^2 = \sin^2\theta\sin^2\phi \leq \sin^2\theta$$

Since $\sin^2\phi \leq 1$. This leads to,

$$s_h^2 + s_v^2 \leq \cos^2\theta + \sin^2\theta = 1 \tag{3.8}$$

The constraint in (3.8) further limits the bounds of s_v and s_h. Figure 3.1 shows the angular domain and the phase domain with its achievable region according to (3.8). We define this region as space $\mathscr{S}$. This will impact the design of the codebook, as to not shift the beams outside the space $\mathscr{S}$.
To make s_v and s_h independent under integration, we replace the achievable space $\mathscr{S}$ (the grey circle in Figure 3.1) with the surrounding square. This results only in the conditions $s_v \in [-1,1]$ and $s_h \in [-1,1]$. We now let $\mathscr{S}$ denote the space of the surrounding square instead of the grey circle in Figure 3.1.

[3]The first reason is because it is not possible to simplify the formula given in (3.5) to integrate across two independent ULAs. The second reason is because the integral of the matrix elements in (3.7) does not have a closed form.

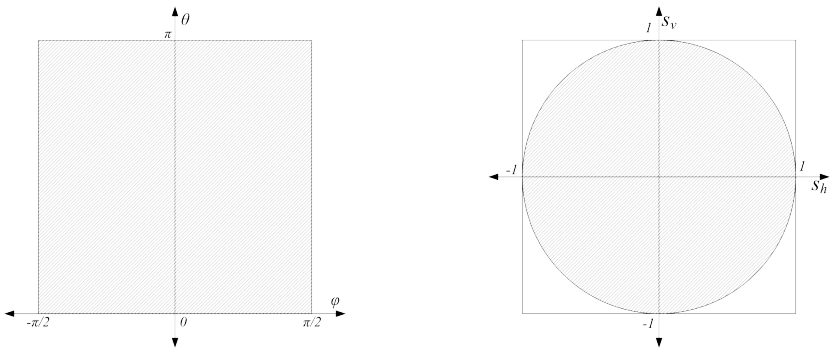

(a) Angular domain **(b)** Phase domain

Figure 3.1: Angular and phase domains. Grey areas indicate achievable regions.

3.2.2 Slepian Beam

The matrix $\mathbf{A}(\theta)$ in (3.7) can now be re-written as

$$\begin{aligned}\mathbf{A}(s_v) &= \mathbf{a}_v(s_v)\mathbf{a}_v^H(s_v) \\ &= \begin{bmatrix} 1 & e^{jkd_vs_v} & e^{2jkd_vs_v} & \dots & e^{(M_v-1)jkd_vs_v} \\ e^{-jkd_vs_v} & 1 & e^{jkd_vs_v} & \dots & e^{(M_v-2)jkd_vs_v} \\ e^{-2jkd_vs_v} & e^{-jkd_vs_v} & 1 & \dots & e^{(M_v-3)jkd_vs_v} \\ \vdots & \vdots & \vdots & \ddots & \vdots \\ e^{(1-M_v)jkd_vs_v} & e^{(2-M_v)jkd_vs_v} & e^{(3-M_v)jkd_vs_v} & \dots & 1 \end{bmatrix}\end{aligned} \tag{3.9}$$

Unlike $\mathbf{A}(\theta)$ in (3.7), integrals of the elements of $\mathbf{A}(s_v)$ in (3.9) - for instance $e^{jkd_vs_v} = \cos(kd_vs_v) + j\sin(kd_vs_v)$ - have closed form expressions. However, one must note:

1. Integrating across s_v cannot be considered as *integration by substitution*, because the latter requires the change of;
   (a) $d\theta$ by $(-ds_v/\sin\theta)$, as
   $$S_v = cos\theta \quad \Longrightarrow \quad \frac{ds_v}{d\theta} = -\sin\theta \quad \Longrightarrow \quad d\theta = \frac{-ds_v}{\sin\theta}$$
   (b) Integration boundary: For example if the integration is bounded by $[a,b]$, then the boundary should be changed to $[\cos^{-1}a, \cos^{-1}b]$.

   Although the second point is satisfied, the first one is not, as the appearance of θ makes the integration still unsolvable, so ds_v is just used. Although this is not the same integration problem as in the angular domain, it is still a good approximation, as will be seen later when verifying the results in the original angular domain.
2. As stated before, the integration in the angular domain has no closed form. However, it is bounded, so it can be evaluated numerically and saved as a look-up table. Still, this thesis will proceed in the phase domain to be able to gain insights[4] from the closed-form expressions that approximate the original ones very well.

[4]The main insight is how the matrix $\mathbf{A}_s(W_v)$ responds to change of the integration boundary.

The double integration introduced in (3.5) that needs to be maximized, can be written in the phase domain as

$$\begin{aligned}\iint G(s_v,s_h;\mathbf{v})ds_v ds_h &= \iint \left|\mathbf{v}_v^H \mathbf{a}_v(s_v)\right|^2 \left|\mathbf{v}_h^H \mathbf{a}_h(s_h)\right|^2 ds_v ds_h \\ &= \int \left|\mathbf{v}_v^H \mathbf{a}_v(s_v)\right|^2 ds_v \int \left|\mathbf{v}_h^H \mathbf{a}_h(s_h)\right|^2 ds_h \qquad (3.10)\\ &= \int G(s_v;\mathbf{v})ds_v \int G(s_h;\mathbf{v})ds \qquad (3.11)\end{aligned}$$

where (3.10) is derived based on that s_v and s_h are independent of each other, which makes the integrand consists of two independent functions, and as a result the integration of their product can be separated to the product of their integrations. This makes it possible to focus on optimizing each ULA separately, which simplifies the problem.
The integration across the vertical dimension introduced in (3.6) can now be written in the phase domain as

$$\mathbf{v}_v^H \Big(\int_{s_v} \mathbf{a}_v(s_v)\mathbf{a}_v^H(s_v)ds_v \Big)\mathbf{v}_v = \mathbf{v}_v^H \Big(\int_{s_v} \mathbf{A}(s_v)ds_v \Big)\mathbf{v}_v \qquad (3.12)$$

Now, let's define the region $\mathscr{S}_{q,p} = [-W_v, W_v] \times [-W_h, W_h]$, where $W_v \in [0,1]$ and $W_h \in [0,1]$. $\mathscr{S}_{q,p}$ is a sub-space of $\mathscr{S}$, and we consider it the region of interest. This sets the integration boundary for the vertical dimension in (3.12) to $[-W_v, W_v]$. Integrating $\cos(kd_v s_v) + j\sin(kd_v s_v)$ over a symmetric boundary around zero, results in that the imaginary part vanishes, as *sine* is an odd function. The real part integrates to $2\sin(kd_v W_v)/kd_v$. Moreover, separation distances are chosen to be $d_v = d_h = \lambda/2$, where λ is the wavelength. Hence, $kd_v = kd_h = \pi$. This leads to,

$$\mathbf{v}_v^H \Big(\int_{-W_v}^{W_v} \mathbf{A}(s_v)ds_v \Big)\mathbf{v}_v = \mathbf{v}_v^H \mathbf{A}_s(W_v)\mathbf{v}_v \qquad (3.13)$$

where,

$$\mathbf{A}_s(W_v) = \begin{bmatrix} 2W_v & \frac{2\sin(\pi W_v)}{\pi} & \frac{2\sin(2\pi W_v)}{2\pi} & \cdots & \frac{2\sin((M_v-1)kd_v W_v)}{(M_v-1)\pi} \\ \frac{2\sin(\pi W_v)}{\pi} & 2W_v & \frac{2\sin(\pi W_v)}{\pi} & \cdots & \frac{2\sin((M_v-2)kd_v W_v)}{(M_v-2)\pi} \\ \frac{2\sin(2\pi W_v)}{2\pi} & \frac{2\sin(\pi W_v)}{\pi} & 2W_v & \cdots & \frac{2\sin((M_v-3)kd_v W_v)}{(M_v-3)\pi} \\ \vdots & \vdots & \vdots & \ddots & \vdots \\ \frac{2\sin((M_v-1)\pi W_v)}{(M_v-1)\pi} & \frac{2\sin((M_v-2)\pi W_v)}{(M_v-2)\pi} & \frac{2\sin((M_v-3)\pi W_v)}{(M_v-3)\pi} & \cdots & 2W_v \end{bmatrix} \qquad (3.14)$$

The matrix $\mathbf{A}_s(W_v)$ is symmetric. For symmetric matrices [24]

- SVD and EVD coincide. i.e. the eigenvalues are the singular values.
- The eigenvalues are real and non-negative.
- The eigenvectors form a unitary matrix. This means the eigenvectors are orthonormal (i.e. orthogonal with unit norm).

Moreover, for $W_v = 1$ (i.e., full range), $\mathbf{A}_s(1) = 2\mathbf{I}_{M_v \times M_v}$. This shows that the total area under the curve shown in Figure 3.2 equals

$$\mathbf{v}_v^H \mathbf{A}_s(1)\mathbf{v}_v = \mathbf{v}_v^H 2\mathbf{I}_{M_v \times M_v}\mathbf{v}_v = 2\mathbf{v}_v^H \mathbf{v}_v = 2\|\mathbf{v}_v\|_2^2 = 2 \qquad (3.15)$$

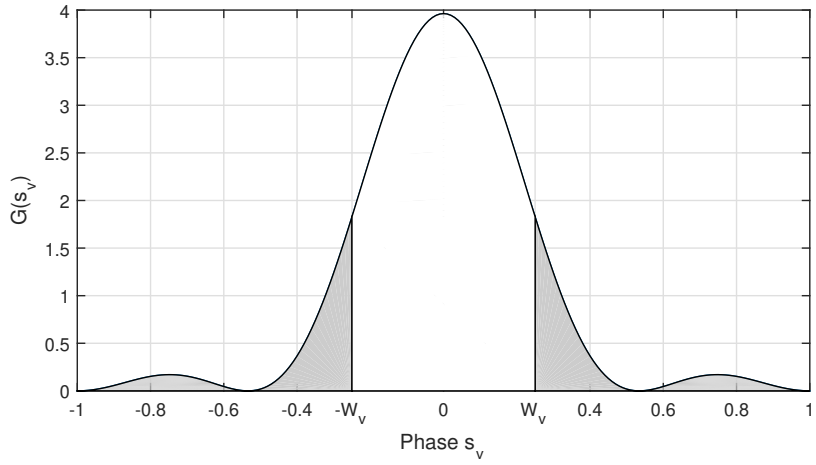

Figure 3.2: Arbitrary radiation pattern shows area under the radiation pattern for the target region [white], and outside [grey]. The white area needs to be maximized, and the grey area needs to be minimized.

This means, regardless of the shape of the radiation pattern, the area under the curve is preserved to 2. Moreover, because the area bounded by $[-W_v, W_v]$ (white region in Figure 3.2) given by (3.13) equals $\mathbf{v}_v^H \mathbf{A}_s(W_v)\mathbf{v}_v$, the area outside (grey region in Figure 3.2) is equal to the white area subtracted from the total area

$$\begin{aligned} \text{Area outside } [-W_v, W_v] &= 2 - \mathbf{v}_v^H \mathbf{A}_s(W_v)\mathbf{v}_v \\ &= \mathbf{v}_v^H 2\mathbf{I}_{M_v \times M_v}\mathbf{v}_v - \mathbf{v}_v^H \mathbf{A}_s(W_v)\mathbf{v}_v \\ &= \mathbf{v}_v^H \Big(2\mathbf{I}_{M_v \times M_v} - \mathbf{A}_s(W_v)\Big)\mathbf{v}_v \end{aligned} \tag{3.16}$$

Now, it is desired to find the weighting vector that maximizes the area in the target region (3.13), consequently minimizes the area outside (3.16). This maximizes the upper bound in (3.3), and can be formulated as an optimization problem

$$\mathbf{v}_v^{opt} = \underset{\mathbf{v}_v:\, \|\mathbf{v}_v\|_2^2 = 1}{\operatorname{argmax}} \frac{\mathbf{v}_v^H \mathbf{A}_s(W_v)\mathbf{v}_v}{\mathbf{v}_v^H \Big(2\mathbf{I}_{M_v \times M_v} - \mathbf{A}_s(W_v)\Big)\mathbf{v}_v} \tag{3.17}$$

This is a *Rayleigh quotient*, and can be maximized as following:
Decompose $\mathbf{A}_s(W_v) = \mathbf{U}\mathbf{\Lambda}\mathbf{U}^{-1} = \mathbf{U}\mathbf{\Lambda}\mathbf{U}^H$, where $\mathbf{U}^{-1} = \mathbf{U}^H$

$$\begin{aligned} \mathbf{v}_v^{opt} &= \underset{\mathbf{v}_v:\, \|\mathbf{v}_v\|_2^2 = 1}{\operatorname{argmax}} \frac{\mathbf{v}_v^H \mathbf{U}\mathbf{\Lambda}\mathbf{U}^H \mathbf{v}_v}{\mathbf{v}_v^H \Big(2\mathbf{I}_{M_v \times M_v} - \mathbf{U}\mathbf{\Lambda}\mathbf{U}^H\Big)\mathbf{v}_v} \\ &= \underset{\mathbf{v}_v:\, \|\mathbf{v}_v\|_2^2 = 1}{\operatorname{argmax}} \frac{\mathbf{v}_v^H \mathbf{U}\mathbf{\Lambda}\mathbf{U}^H \mathbf{v}_v}{\mathbf{v}_v^H \mathbf{U}\Big(2\mathbf{I}_{M_v \times M_v} - \mathbf{\Lambda}\Big)\mathbf{U}^H \mathbf{v}_v} \end{aligned}$$

Let $\mathbf{z} = \mathbf{U}^H \mathbf{v}_v \implies \mathbf{z}^H = \mathbf{v}_v^H \mathbf{U}$ and $\mathbf{v}_v = \mathbf{U}\mathbf{z}$

$$\mathbf{z}^{opt} = \underset{\mathbf{z}:\ \|\mathbf{U}\mathbf{z}\|_2^2=1}{\operatorname{argmax}} \frac{\mathbf{z}^H \mathbf{\Lambda} \mathbf{z}}{\mathbf{z}^H \Big(2\mathbf{I}_{M_v \times M_v} - \mathbf{\Lambda}\Big)\mathbf{z}}$$

Moreover, $\|\mathbf{U}\mathbf{z}\|_2^2 = \mathbf{z}^H \mathbf{U}^H \mathbf{U}\mathbf{z} = \mathbf{z}^H \mathbf{z} = \|\mathbf{z}\|_2^2$

$$\mathbf{z}^{opt} = \underset{\mathbf{z}:\ \|\mathbf{z}\|_2^2=1}{\operatorname{argmax}} \frac{\mathbf{z}^H \mathbf{\Lambda} \mathbf{z}}{\mathbf{z}^H \Big(2\mathbf{I}_{M_v \times M_v} - \mathbf{\Lambda}\Big)\mathbf{z}} \tag{3.18}$$

The vector that maximizes (3.18) is $\mathbf{z} = \begin{bmatrix} 1 & 0 & 0 & \cdots \end{bmatrix}^T$, that selects the maximum eigenvalue out of the diagonal matrix $\mathbf{\Lambda}$. Consequently,

$$\mathbf{v}_v^{opt} = \mathbf{U}\mathbf{z} = \begin{bmatrix} \mathbf{u}_1 & \mathbf{u}_2 & \cdots & \mathbf{u}_{M_v} \end{bmatrix} \begin{bmatrix} 1 & 0 & 0 & \cdots \end{bmatrix}^T = \mathbf{u}_1 \tag{3.19}$$

Hence, the weighting vector that maximizes the area inside the region of interest, is the eigenvector corresponding to the maximum eigenvalue of the matrix $\mathbf{A}_s(W_v)$, making the area inside the region of interest equal to the maximum eigenvalue λ_{max}, and the maximum value of the optimization problem in (3.17) is $\lambda_{max}/(2-\lambda_{max})$.
In the rest of this thesis, we name this weighting vector as the Slepian beam.

3.2.3 Properties of the Slepian Beam

This section discusses some of the Slepian beam properties, to illustrate how it behaves.

3.2.3.1 Scanning of Parameter W_v

Let's recall elements of the matrix $\mathbf{A}_s(W_v)$ as below,

$$\mathbf{A}_s(W_v)_{k,l} = \begin{cases} \frac{2\sin((l-k)\pi W_v)}{(l-k)\pi} & ,k \neq l \\ 2W_v & ,k = l, \quad \textit{where } k \textit{ and } l = 1,2,\ldots,M_v \end{cases}$$

When $W_v = 0$, then $\mathbf{A}_s(W_v) = \mathbf{0}_{M_v \times M_v}$. For such all-zero matrix, all eigenvalues are zeros. Hence, when $W_v = 0$, the eigenvector matrix is undetermined. However, for $W_v \to 0$, the Slepian beam converges to the DFT beam defined in Subsection 2.2.1. This can be shown as follows. For very small values of W_v, the following approximation is valid:
$\sin x \approx x$, for $x \to 0$. Hence,

$$\mathbf{A}_s(W_v) \to 2W_v \mathbf{1}_{M_v \times M_v} \tag{3.20}$$

which is a rank 1 matrix with the maximum eigenvalue ($\lambda_{max} = 2W_v M_v$), and all other eigenvalues are zeros. In such a case, the eigenvector corresponding to the maximum eigenvalue is $\mathbf{u}_1 = \frac{1}{\sqrt{M_v}} \mathbf{1}_{M_v \times 1}$, which is the same as the DFT beam defined in Subsection 2.2.1, pointing towards the broadside direction.
This can be justified as, for a very small W_v approaching zero, the width of the area where the beam pattern is maximally concentrated converges to a single point, and the area is

then maximized by maximizing the peak. As the DFT pattern has the maximum possible peak, the Slepian necessarily converges to it.

On the other hand, when $W_v = 1$, then $\mathbf{A}_s(W_v) = 2\mathbf{I}_{M_v \times M_v}$. For such a diagonal matrix, all eigenvalues equal 2 and the eigenvector matrix can be any unitary matrix. Hence, when $W_v = 1$, the eigenvector matrix is undetermined. However, when $W_v \to 1$, the Slepian beam converges to the binomial beam defined in Subsection 2.2.2. This can be concluded by observing how the zeros of the radiation pattern behave by scanning W_v. We recall that the radiation pattern is the square of the array factor, so both have the same zeros at the same locations. We quote the following line from [22, pp.1375] that describes the zeros of the *Discrete Prolate Spheroidal Wave Function* (DPSWF)

> *"The DPSWF $U_k(N,W;f)$ has exactly k zeros in the open interval $-W < f < W$ and exactly $N-1$ zeros in $^{-1}/_2 < f \leq {}^{1}/_2$."*

In our case, the function $U_k(N,W;f)$, where $k = 0,1,\ldots,N-1$ represents the array factor that results from using N array elements, Slepian width of W, and the eigenvector k of the matrix in (3.14) as a weighting vector, where $k = 0$ is the eigenvector corresponding to the maximum eigenvalue - which is the Slepian beam -, and $k = N-1$ is the eigenvector corresponds to the minimum eigenvalue. Back to our notation, this implies that the array factor of the Slepian beam always has $M_v - 1$ zeros inside the interval $s_v \in [-1,1)$. However, it has no zero in the interval $s_v \in (-W_v, W_v)$. In other words, all the zeros of the Slepian array factor are always outside the target region bounded by $(-W_v, W_v)$.
Now, for increasing W_v, the zeros will be shifted outwards as follows. For an odd number of zeros, one will be located at $s_v = 1$, then half of the remaining converge to $s_v = -1$, and the other half converge to $s_v = 1$. For an even number of zeros, half of them converge to $s_v = -1$, and the other half converge to $s_v = 1$.
We recall that, for the binomial beam, all zeros of the array factor/radiation pattern are located exactly at $\theta = 0$ and mirrored at $\theta = 180$, or in the phase domain they are located exactly at $s_v = 1$ and mirrored at $s_v = -1$. This leads to the conclusion that, for $W_v \to 1$, the array factor of the Slepian converges to the array factor of the binomial beam with the same number of antenna elements. This basically means that their DFTs converge to each other, which implies that the sequences (beam weights) also converge to each other.

Figure 3.3 shows graphically the parameter W_v scanning from 0 to 1. A ULA with 5 antenna elements is useded to generate the figure. A DFT beam has equal weights ($v_0 = v_1 = v_2 = v_3 = v_4 = 1/\sqrt{5} \approx 0.4472$), indicated in the figure by a circle. From Pascal triangle, the binomial beam weight ratios are [1 4 6 4 1], with norm of $\sqrt{70}$. Hence the weights of the binomial beam are ($v_0 = v_4 = \frac{1}{\sqrt{70}} \approx 0.1195; v_1 = v_3 = \frac{4}{\sqrt{70}} \approx 0.4781; v_2 = \frac{6}{\sqrt{70}} \approx 0.7171$), indicated in the figure by dotted lines. Finally, the weights of the Slepian beams scanning W_v from 0 to 1 are shown, and for $W_v \to 0$ they converge to the DFT, while for $W_v \to 1$ they converge to the binomial beam. Note that, the weights of the Slepian are symmetric, so in the figure, v_0 and v_4 coincide, and the same for v_1 and v_3.

Figures 3.4 and 3.5 show (in phase and angular domains, respectively) the radiation pattern of the Slepian beam for different selected values of W_v. For small values approaching 0, the pattern looks like the DFT, by increasing W_v the zeros move and get compressed towards the edges resulting in a wider main-lobe, with smaller side-lobes. Eventually, for

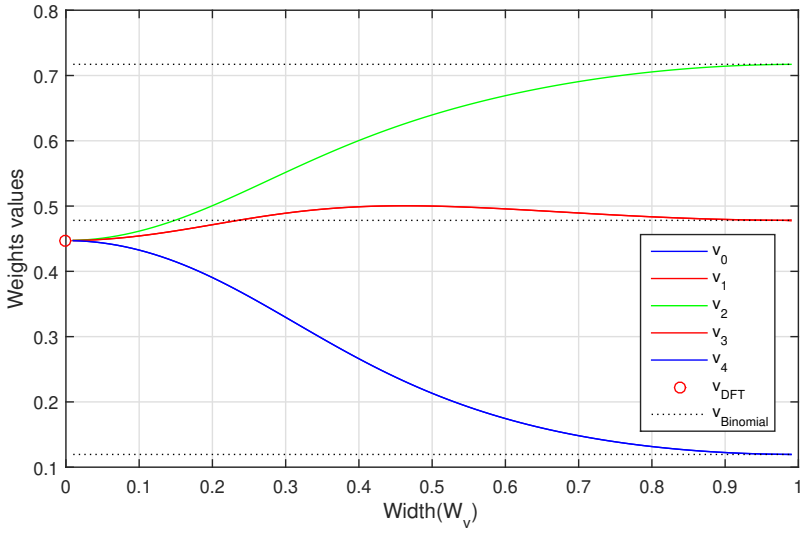

Figure 3.3: The weights of a 5 antenna elements Slepian beam scan from $W_v = 0$ where they converge to DFT, to $W_v = 1$ where they converge to binomial.

values approaching 1, the radiation pattern looks like the binomial as the zeros almost coincide at the edges. By comparing the two figures, it can be seen that the difference in radiation pattern shape is marginal between the phase domain and the angular domain.

3.2.4 Comparing the Slepian Beam with other Beam Synthesizers

The benefit of using the Slepian beam can be shown as follows. Assume an incoming signal with angle θ and received power P_s which is assumed to be constant. Moreover, the PDF of the $s_v = \sin\theta$ of the incoming signal is expected to be between $[-W_v, W_v]$, with a uniform[5] distribution over many realizations as showed in Figure 3.6. Furthermore, the same figure shows the distribution of an incoming interference signal, two cases are investigated. Case 1 assumes the interference is coming from outside the signal region uniformly, while case 2 assumes the interference is coming uniformly from the whole range. As seen in (3.19), the Slepian beam maximizes the area inside the signal region. In such uniform distribution, the average gain that the received signal will experience due to array gain equals the area divided by the total width ($\lambda_{max}/2W_v$). As Slepian beam maximizes the area (λ_{max}) for a target region ($2W_v$), hence it maximizes the average gain that multiplies the signal, and consequently it maximizes the capacity upper bound (3.3) in a noise limited scenario. For the interference region, considering case 1, a Slepian beam

[5] If s_v has a uniform distribution, then $\theta = \cos^{-1} s_v$ is not uniform. It makes more sense to assume that θ has uniform distribution. However, for convenience, here we choose to assume s_v is uniform because we are working in phase domain.

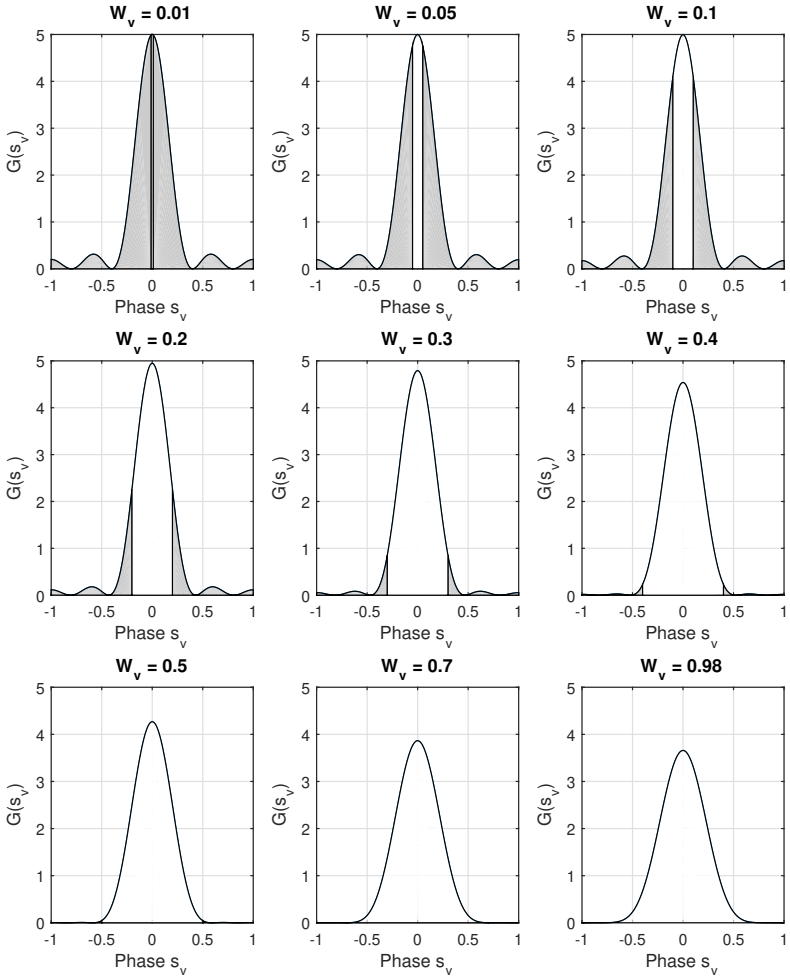

Figure 3.4: The radiation pattern of the Slepian beam of 5 antenna elements, scanned across selected values of W_v starting from DFT and ending with binomial. The patterns are drawn in the phase domain. The width of the targeted area [white area] is $2W_v$.

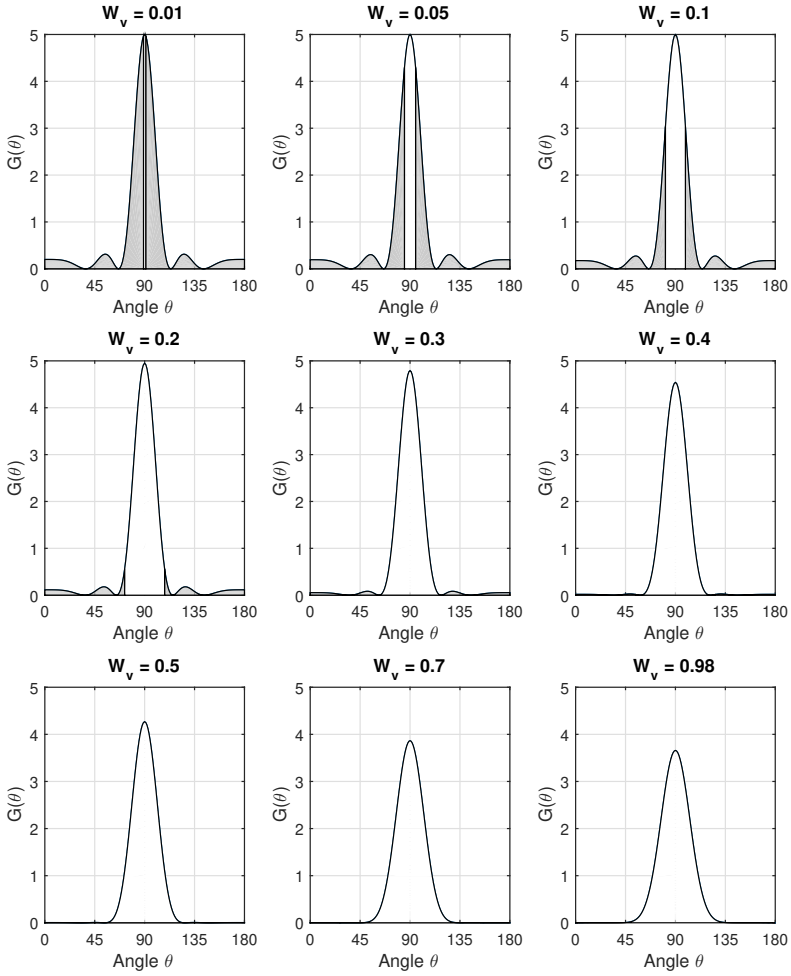

Figure 3.5: The radiation pattern of the Slepian beam of 5 antenna elements, scanned across selected values of W_v starting from DFT and ending with binomial. The patterns are drawn in the angular domain. The width of the targeted area [white area] is $2\cos^{-1}(W_v)$.

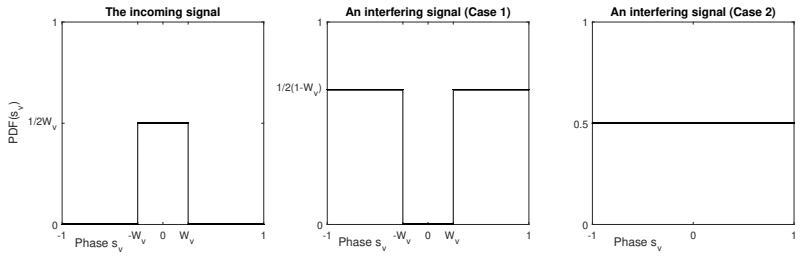

Figure 3.6: Phase distribution of the incoming signal [Left] and an interfering signal. There are two cases of interference distribution [Mid, Right].

also minimizes the area of the outside region[6], hence minimizes the average gain that multiplies the interference, consequently it maximizes[7] the capacity upper bound in an interference limited scenario. However, considering case 2 of interference distribution, the average gain that multiplies the interference will always be constant, and equals to unity[8]. So it is a constant term added to the noise power, and this case can be considered as a noise limited scenario. The next three subsections compare by the use of figures the Slepian beam synthesizer with DFT, binomial and Chebyshev beam synthesizers.

3.2.4.1 Slepian and DFT

The DFT beam does not have many degrees of freedom, only the number of activated antenna elements can change the width/peak (Figure 3.7a) conserving the total area by normalization. Consider that it is required to divide the range of S_v to five equal sub-regions, and use a beam to scan each individually. Using DFT, a beam with 5 antenna elements is used, and compared against a Slepian beam with 5 antenna elements and width $W_v = 1/5 = 0.2$. Both beams are depicted in Figure 3.8 in linear and logarithmic scales for comparison. One can notice that the Slepian beam has a slightly lower peak, but the main-lobe is more flat inside the area of interest. In the interference region, it can be seen that the Slepian is below the DFT (smaller side-lobes). All plots are converted to the angular domain. We recall that the Slepian beam converges to the DFT beam for $W_v \to 0$.

3.2.4.2 Slepian and Binomial

The binomial beam also does not have many degrees of freedom, only the number of activated antenna elements can change the width/peak (Figure 3.7b) preserving the total area by normalization. Consider that it is required to divide the range of S_v to six equal sub-regions, and use a beam to scan each individually. A binomial beam with 6 antenna elements is compared against a Slepian beam with the same number of antenna elements and $W_v = 1/6 = 0.1667$. Both beams are depicted in Figure 3.9 in linear and logarithmic scales. One can notice that the Slepian beam has a higher peak, and higher area concentrated

[6]Since the total area under the curve is always fixed.

[7]This must be side by side with the maximization of the signal region.

[8]The area under the curve is 2 (3.15), divided by the total width which is 2, results in a unity.

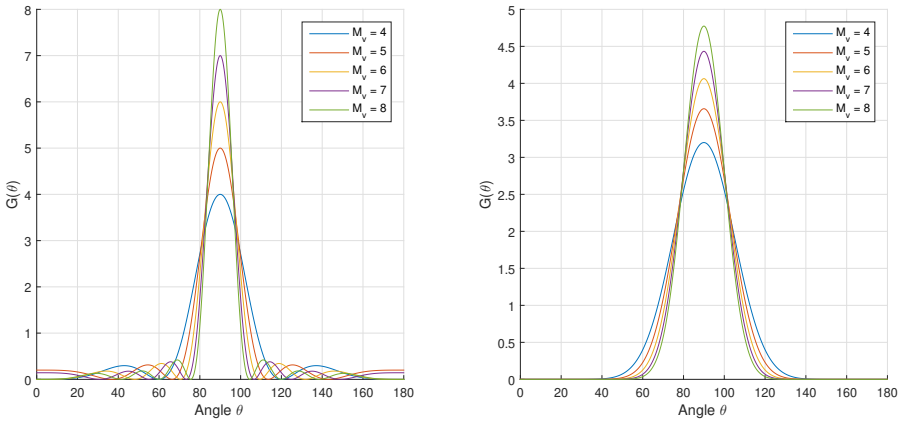

(a) DFT beams **(b)** Binomial beams

Figure 3.7: Radiation patterns of a ULA that uses DFT/binomial beams for different numbers of antenna elements.

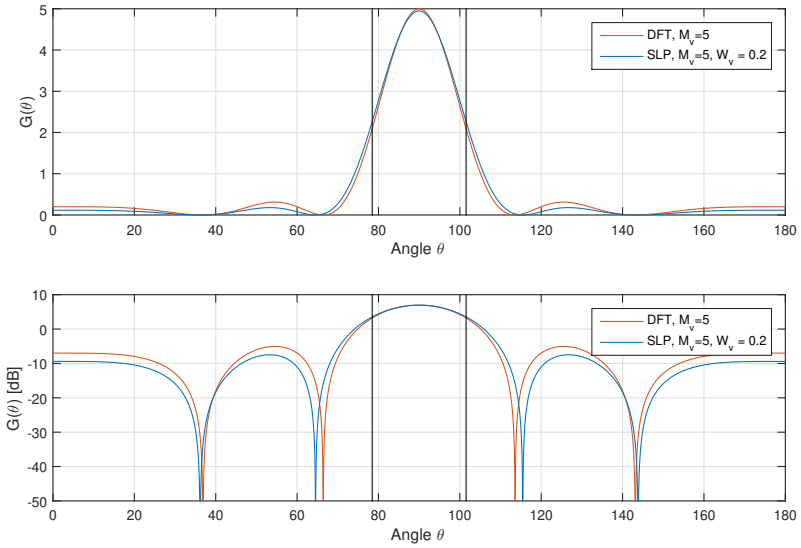

Figure 3.8: Radiation patterns of a ULA that uses Slepian/DFT beams.

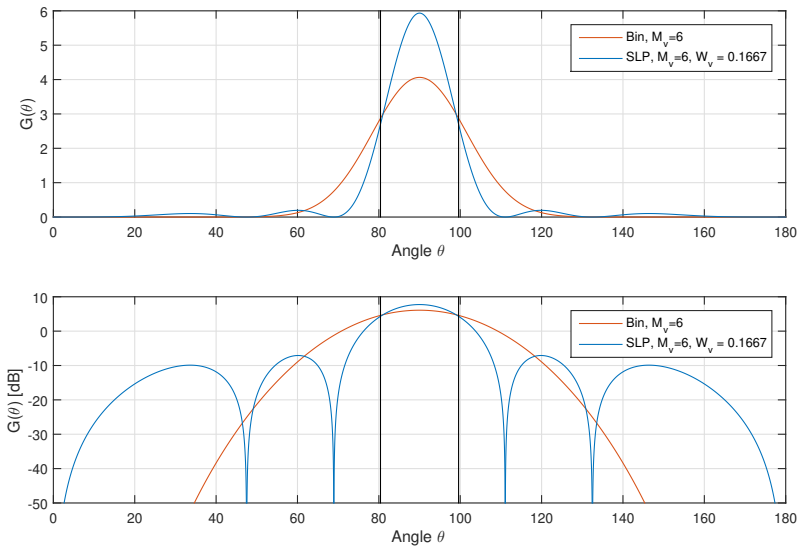

Figure 3.9: Radiation patterns of a ULA that uses Slepian/binomial beams.

inside the region of interest. On the other hand, the binomial leaks too much area outside although it has no side-lobes. All plots are converted to the angular domain. We recall that the Slepian beam converges to the binomial beam for $W_v \to 1$.

3.2.4.3 Slepian and Chebyshev

The Chebyshev beam has the number of activated antenna elements as a degree of freedom, in addition to attenuation parameter α, which is the ratio between the main-lobe's peak to the side-lobe peaks (all side-lobes have the same level) in Decibels. Figure 3.10 shows a Chebyshev beam for the same number of elements, but different values of attenuation parameter. Normalization ensures the conservation of the total area for different numbers of antenna elements, while the attenuation parameter does not affect that.
The next three figures show how the Slepian concentrates the pattern in a better way. Figure 3.11 compares the two beams using a ULA of 7 antenna elements. Careful inspection shows the main-lobe of the Slepian has a slightly higher level, consequently the sides-lobes slightly shrink. Figure 3.12 compares the two beams using a ULA of 10 antenna elements. It is clearer in this case that the Chebyshev main-lobe cannot go as high as the Slepian, as the latter leaks area from the main-lobe and makes the total area inside the side-lobes higher than the Slepian. Although the first side-lobe level of the Slepian is still higher than that of the Chebyshev, all the subsequent side-lobe levels are lower. Figure 3.13 shows the same comparison but for a 16 elements ULA. For such -relatively high- number of antenna elements, it is easier to see that the Slepian concentrates more area inside the region of interest than the Chebyshev, leading to lower total area in the side-lobes. In the

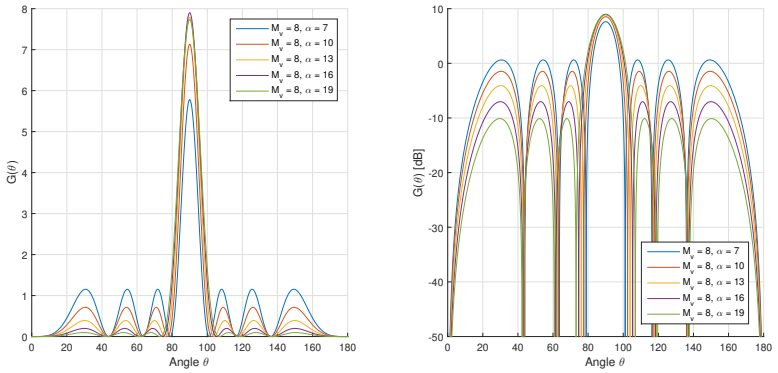

Figure 3.10: Radiation patterns of a ULA that uses Chebyshev beams for different attenuation factor values.

three figures mentioned above, comparison in the logarithmic scale is used to give a clearer view, and the width of the signal region is always set to be 1 divided by the number of antenna elements. For a fair comparison, α has been selected[9] so that it achieves its highest capacity upper bound, however, the Slepian still gives a higher[10] upper bound. For a small number of antenna elements, the difference between the upper bounds of Chebyshev and Slepian is small, but it increases with an increased number of antenna elements.

The discussion above is important to explain where the expected difference in the achieved capacity comes from. In the following chapter, more figures show the performance of the Slepian beam by comparing the capacity and capacity upper bound which confirms the above deductions. Finally, we mention that all plots are converted to the angular domain.

3.3 Selection of Free Parameters

In the previous section, it has been shown that the Slepian beam can scan from narrow region (approaches DFT), to wide region (approaches binomial) using the variable W_v. However, there is one more degree of freedom, which is the number of activated antenna elements. Hence for a specific region of interest, a Slepian beam covering the region is determined by two parameters - number of active antenna elements and the parameter W_v. The higher the number of active antenna elements the higher the area concentrated inside the region (due to higher λ_{max}). However, this does not necessarily mean more flatness of the pattern inside, so the mean capacity is not necessarily closer to the upper bound in (3.3). Figure 3.14 shows the radiation pattern of Slepian beams for 4-8 antenna elements. The smaller the number the less area concentration inside, but also better flatness. To select which is better for the capacity, another metric is introduced that measures the closeness to the flat ideal beam mentioned in Subsection 3.1.2. The metric used is the squared error.

[9] Using numerical computation, α that achieves the highest capacity upper bound is selected.
[10] This will be shown in Chapter 4 by figures.

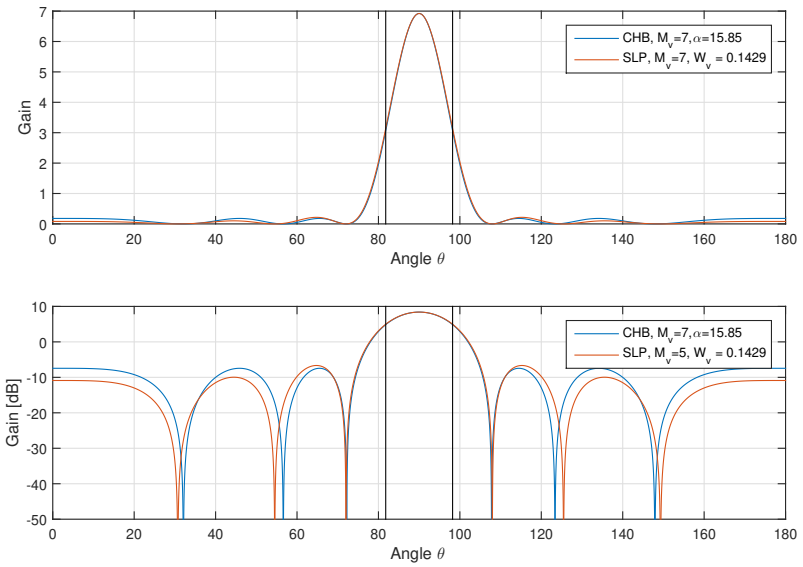

Figure 3.11: Radiation patterns of a ULA that uses Slepian/Chebyshev beams (7 antenna elements).

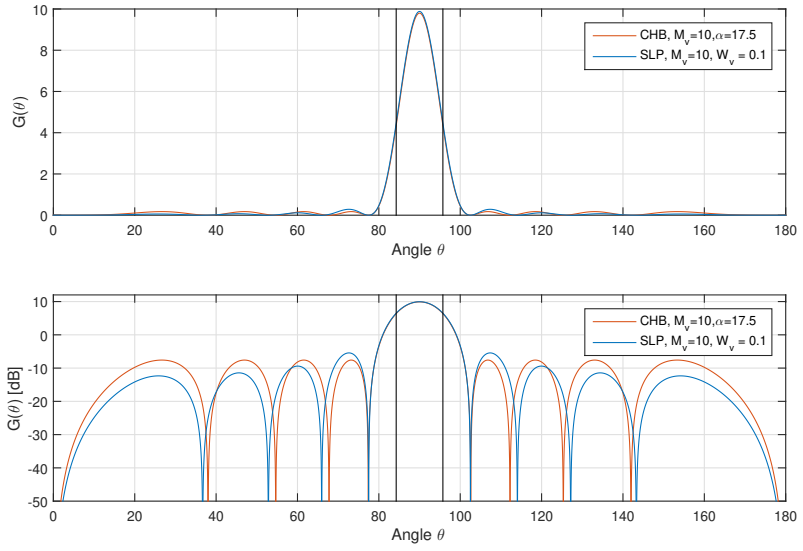

Figure 3.12: Radiation patterns of a ULA that uses Slepian/Chebyshev beams (10 antenna elements).

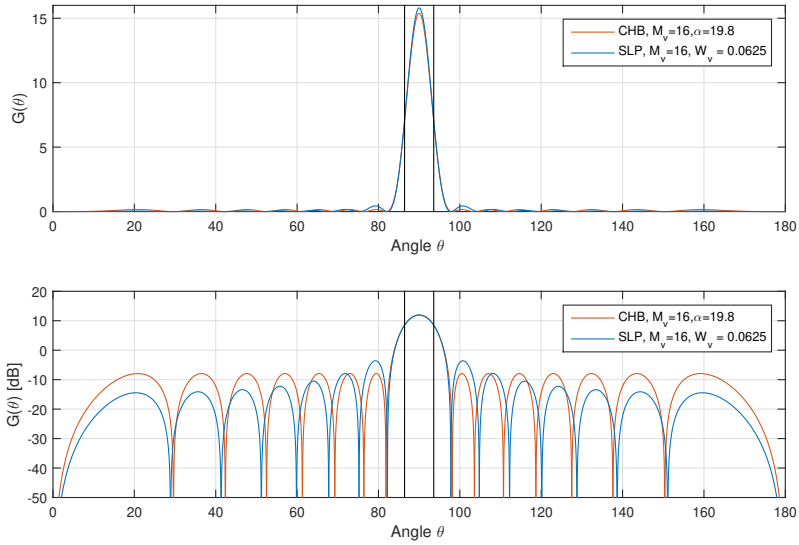

Figure 3.13: Radiation patterns of a ULA that uses Slepian/Chebyshev beams (16 antenna elements).

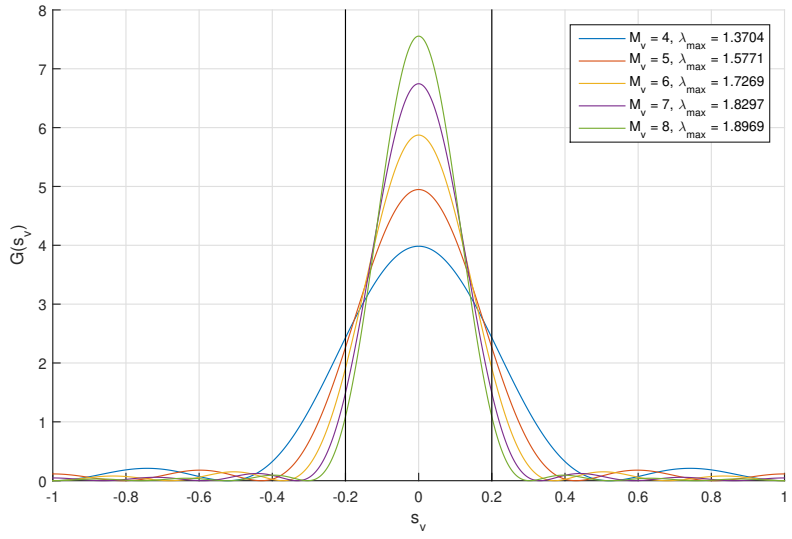

Figure 3.14: Radiation patterns of a ULA that uses Slepian beams for $W_v = 0.2$, and different number of antenna elements. λ_{max} is showed for each.

3.3.1 Minimum Squared Error as a Metric

The squared error (SE) is by definition the square of subtraction between the ideal beam pattern for a target area, and another beam pattern that is under comparison [12]. Our approach is calculating the SE for the Slepian beam pattern for various numbers of antenna elements (M_v,M_h) and widths (W_v,W_h), and the Slepian beam pattern with the minimum SE (MSE) is selected. For efficient calculation, this thesis introduces a closed form for SE that makes the calculation tractable. This is an improvement compared to [12] where *Orthogonal Matching Pursuit* (OMP) Algorithm was employed to compute each candidate beam satisfying some constrains and the final beam accomplishing the MSE minimization objective was chosen.
Assume the radiation pattern of the ideal beam has a constant flat pattern Q, covering the region $[-W_h, W_h] \times [-W_v, W_v]$ and is zero outside. In order to ensure the total volume is preserved and equal to 4, $Q = 1/(W_v W_h)$ is used. The squared error can be calculated as

$$\begin{aligned}
\text{SE} &\triangleq \int_{-1}^{1}\int_{-1}^{1}\Big(G^{\text{ideal}} - G(s_v, s_h; \mathbf{v})\Big)^2 ds_v ds_h \\
&= \int_{-1}^{1}\int_{-1}^{1}\Big(G(s_v, s_h; \mathbf{v})\Big)^2 ds_v ds_h - 2\int_{-1}^{1}\int_{-1}^{1} G^{\text{ideal}} G(s_v, s_h; \mathbf{v}) ds_v ds_h \\
&\quad + \int_{-1}^{1}\int_{-1}^{1}\Big(G^{\text{ideal}}\Big)^2 ds_v ds_h \\
&= \int_{-1}^{1}\int_{-1}^{1}\Big(G(s_v, s_h; \mathbf{v})\Big)^2 ds_v ds_h - 2Q\int_{-W_v}^{W_v}\int_{-W_h}^{W_h} G(s_v, s_h; \mathbf{v}) ds_v ds_h \\
&\quad + Q^2(2W_v)(2W_h)
\end{aligned} \tag{3.21}$$

where in the second term in (3.21), the integration boundaries have been reduced because G^{ideal} is zero outside these boundaries, and the third term is just an integration of a constant. Now let's separate integration over s_v and s_h as in (3.11)

$$\begin{aligned}
\text{SE} &= \int_{-1}^{1}\Big(G(s_v; \mathbf{v}_v)\Big)^2 ds_v \int_{-1}^{1}\Big(G(s_h; \mathbf{v}_h)\Big)^2 ds_h \\
&\quad -2Q\int_{-W_v}^{W_v} G(s_v; \mathbf{v}_v) ds_v \int_{-W_h}^{W_h} G(s_h; \mathbf{v}_h) ds_h + 4Q^2 W_v W_h
\end{aligned}$$

The integration of the integrals in the second term is given by (3.13), and when the Slepian beam is used they equal the maximum eigenvalue of the matrix (3.14). The integration of the first term, and since the integration boundaries are $[-1, 1]$, will end up as the sum of the products of beam weights following a certain sequence as shown in Appendix A equation (A.1). The integrated closed form of the squared error is

$$\begin{aligned}
\text{SE} &= 2\Bigg(\sum_{a=0}^{M_v-1} v_{v,a} \sum_{b=0}^{M_v-1} v_{v,b} \sum_{c=|a-b|}^{M_v-1} v_{v,c}.v_{v,(c-|a-b|)}\Bigg). \\
&\quad 2\Bigg(\sum_{a=0}^{M_h-1} v_{h,a} \sum_{b=0}^{M_h-1} v_{h,b} \sum_{c=|a-b|}^{M_h-1} v_{h,c}.v_{h,(c-|a-b|)}\Bigg) \\
&\quad -2Q\lambda_{max}\Big(\mathbf{A}_s(W_v)\Big).\lambda_{max}\Big(\mathbf{A}_s(W_h)\Big) + 4Q^2 W_v W_h
\end{aligned} \tag{3.22}$$

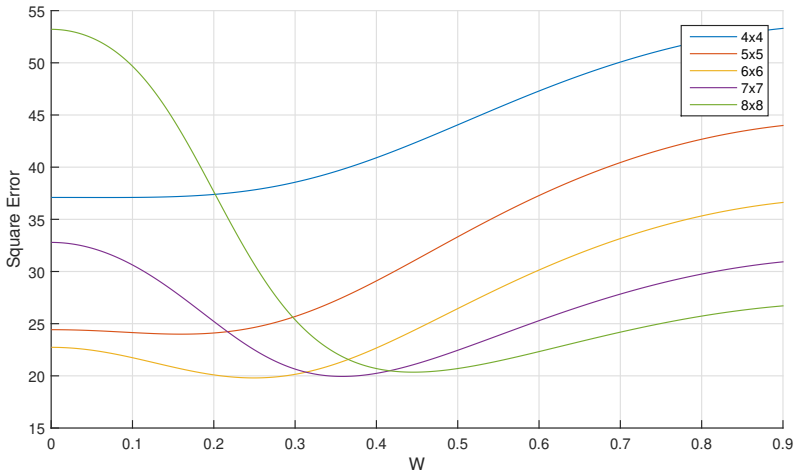

Figure 3.15: Minimum SE of a UPA that uses Slepian beams for $W_v = W_h = W = 0.2$, and different number of activated antenna elements.

The formula in (3.22) is computationally tractable, and can be used to scan/compare Slepian beam patterns for different numbers of antenna elements and widths. Figure 3.15 shows square error versus W of a UPA employing a Slepian beam, where $W_h = W_v = W$. Each dimension is divided into 5 sub-region (i.e., the area to be covered is 0.2 of each dimension) so the optimum values that concentrate most of the beam energy inside are $W_h = W_v = 0.2$. At this point ($W = 0.2$) in the figure, the number of activated antenna elements per dimension that achieves the lowest SE is as follows: 6, 5, 7, 4 then 8. However, it seems the minimum point of all curves (the MSE) happens at the number of elements per dimension being equal to 6, and $W_v = W_h = 0.25$ not 0.2. The reason is that the Slepian optimization problem maximizes the beam energy inside the target area but does not consider flatness of the radiation pattern curve. The MSE can be a good measure for scanning different combinations of widths and numbers of active antenna elements together to find the Slepian beam that covers the area of 0.2 in the best possible way (i.e., comes closest to the ideal beam pattern).

Figures 3.16 and 3.17 respectively show the Slepian beam pattern with 6 activated antenna elements and $W_v = W_h = 0.25$, and 8 activated antenna elements and $W_v = W_h = 0.2$. The former looks more "flat" than the latter that uses all antenna elements and concentrates the energy within that area. The same procedure can be done for a DFT beam as well, considering that the MSE metric is good in creating flat beams within a region.

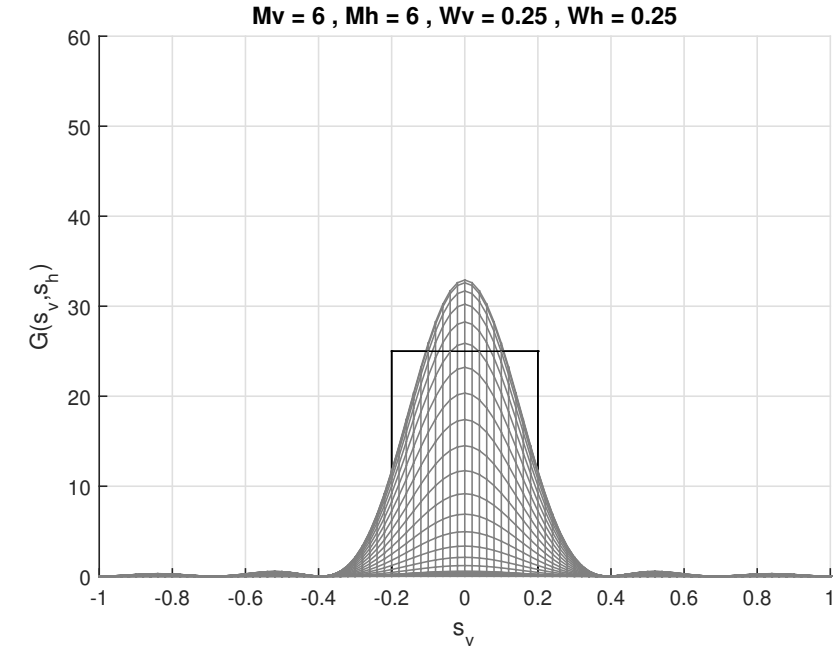

(a) Side view

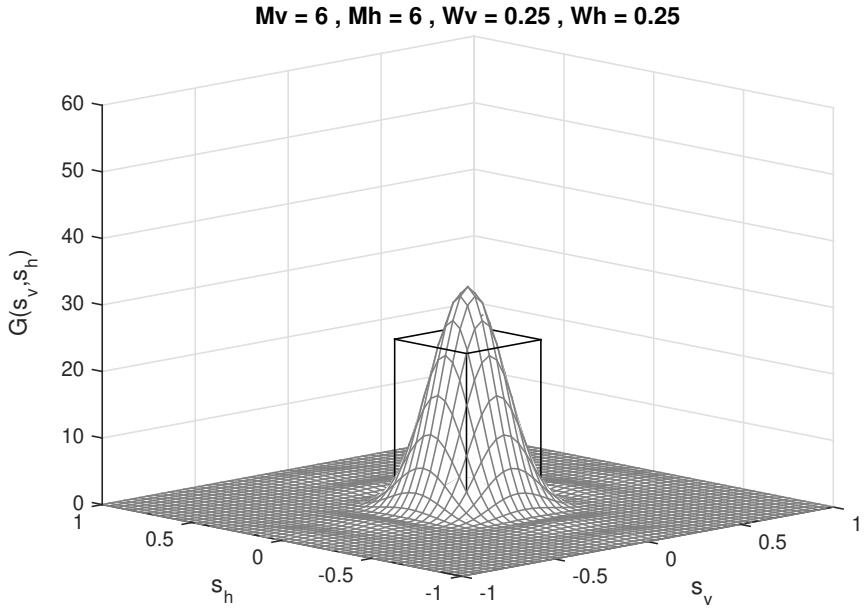

(b) 3D view

Figure 3.16: UPA that uses Slepian, with 6 antenna elements activated on each dimension, and $W_v = W_h = 0.25$, intended to cover a region 0.2 on each direction. The region is indicated by lines.

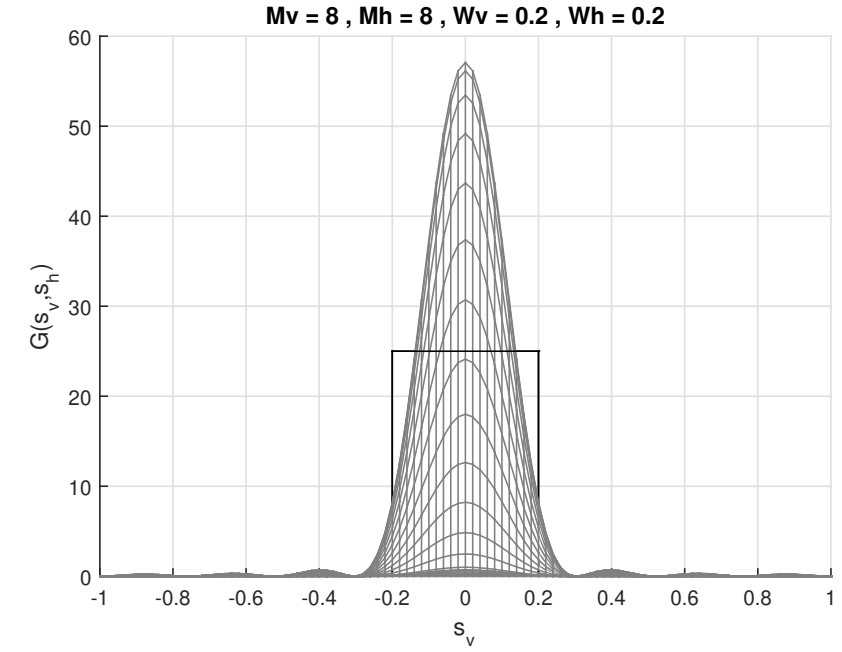

(a) Side view

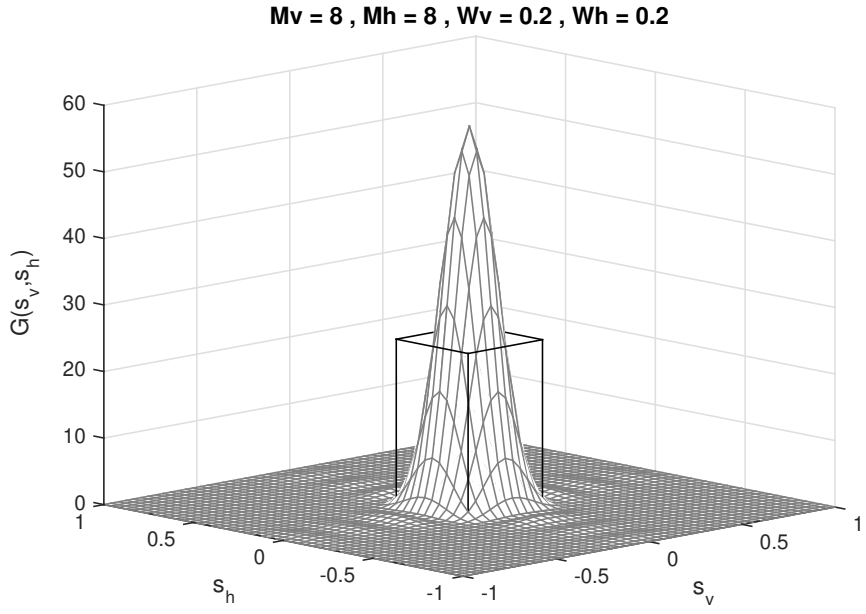

(b) 3D view

Figure 3.17: UPA that uses Slepian, with 8 antenna elements activated on each dimension, and $W_v = W_h = 0.2$, intended to cover a region 0.2 on each direction. The region is indicated by lines.

Chapter 4

Methodology II: Capacity Analysis

This chapter introduces the analysis on the capacity obtained when using beamforming, and shows some numerical simulations for the Slepian beam and other beams discussed in this thesis. Assume an incoming desired signal with received power P_s, and N number of interference signals with power $P_{I,n}$ each, where $n = 1,2,3,\ldots,N$. The desired signal comes from angle θ_0, and the interference signals come from angles θ_n, where $n = 1,2,3,\ldots,N$. We let $s_0 = \cos\theta_0$ denote the phase of the desired incoming signal, and $s_n = \cos\theta_n$ denote the phase of interference signals where $n = 1,2,3,\ldots,N$. The subscript $(_v)$ denoting *vertical* is omitted in this chapter for convenience, however, it must be noted that all the calculations below are done in the vertical domain, but the approach is equally applicable for the horizontal domain.
As a starting example, let s_0 have the uniform[1] distribution

$$f(s_0) \in \mathscr{U}(-W,W)$$

where $f(s_0)$ is the PDF of s_0, which is also shown in Figure 3.6 [Left]. Furthermore, we assume that s_n belongs to the following distribution

$$f(s_n) \in \begin{cases} \mathscr{U}(-1,-W) \cup \mathscr{U}(W,1) & \text{(Case 1)} \\ \mathscr{U}(-1,1) & \text{(Case 2)} \end{cases}$$

which are both shown in the same figure (Figure 3.6 [Mid] and [Right], respectively). As we are interested in studying the effect of the radiation pattern on the capacity, both P_s and $P_{I,n}$ are assumed to be constants.
The mean capacity can be calculated as

$$\overline{C} = \mathbb{E}\left\{ \log_2\left(1 + \frac{P_s \mathbf{v}^H \mathbf{A}(s_0)\mathbf{v}}{N_0 + \mathbf{v}^H\Big(P_{I,1}\mathbf{A}(s_1) + \cdots + P_{I,n}\mathbf{A}(s_n)\Big)\mathbf{v}}\right)\right\} \tag{4.1}$$

where $\mathbf{v}$ is the used beam.
Now let's define $S_R = \mathbf{v}^H \mathbf{A}(s_0)\mathbf{v}$ as the radiation pattern inside the *Signal Region*, which represents the section of the radiation pattern curve (The solid line section of the curve in

[1] If s_0 (also s_n) has a uniform distribution, then $\theta_0 = \cos^{-1} s_0$ is not uniform. It makes more sense to assume that θ_0 has uniform distribution. However, for convenience, here we choose to assume s_0 is uniform because we are working in the phase domain.

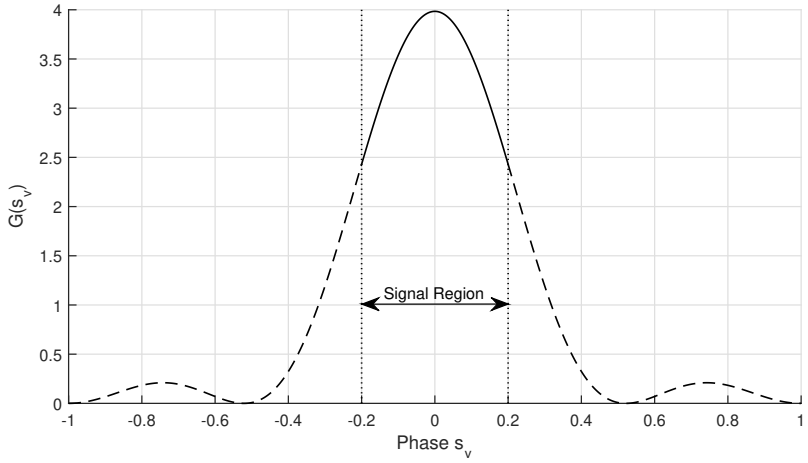

Figure 4.1: An arbitrary beam showing signal/interference regions.

Figure 4.1) that falls inside the region where the signal is expected to come from. For the uniform distribution of s_0 proposed above, the expectation of S_R for the Slepian beam is

$$\mathbb{E}\{S_R\} = \frac{1}{2W}\lambda_{max}(\mathbf{A}_s(W)) \tag{4.2}$$

Moreover, we define $I_{R,n} = \mathbf{v}^H \mathbf{A}(s_n)\mathbf{v}$, where $n = 1,2,\ldots,N$, as the radiation pattern inside the *Interference Regions*, which represents the section of the radiation pattern curve that falls inside the region where the interference is expected to come from. For the uniform distribution (Case 1) of s_n, $I_{R,n}$ is the dashed line section of the curve in Figure 4.1. The expectation of $I_{R,n}$ in this case for the Slepian beam is

$$\mathbb{E}\{I_{R,n}\} = \frac{1}{2(1-W)}\left(2 - \lambda_{max}\Big(\mathbf{A}_s(W)\Big)\right) \quad \ldots \text{Case 1} \tag{4.3}$$

For the uniform distribution (Case 2) of s_n, $I_{R,n}$ is the whole curve in Figure 4.1, the expectation of $I_{R,n}$ in this case for the Slepian beam is

$$\mathbb{E}\{I_{R,n}\} = \frac{1}{2}\lambda_{max}(\mathbf{A}_s(1)) = \frac{1}{2}2 = 1 \qquad \ldots \text{Case 2} \tag{4.4}$$

Note that the three expected values above are not assumed always, and not used later nor vital for calculations. However, they are given here as examples for more insights into how sections of the radiation pattern are averaged.

From (4.1), the mean capacity can be expressed as:

$$\overline{C} = \int\cdots\int f(s_0,s_1,\ldots,s_n)\log_2\left(1 + \frac{P_s S_R}{N_0 + P_{I,1}I_{R,1} + \cdots + P_{I,n}I_{R,n}}\right) ds_0 ds_1 \ldots ds_n \tag{4.5}$$

where $s_0,\ldots,s_n$ can be considered as independent variables, so their joint probability function $f(s_0,s_1,\ldots,s_n)$ is the multiplication of individual PDFs of each variable.
The integration in (4.5) is hard to evaluate. Instead, the next sections discuss its bounds.

4.1 Mean Capacity Bounds

As can be seen in (4.5), since the integration is hard to evaluate, it is more convenient and tractable to evaluate and analyze its bounds rather than the true mean capacity. Jensen's inequality is used to upper and lower bound the capacity. Jensen's inequality states

$$\mathbb{E}\{g(x)\} \leq g(\mathbb{E}\{x\}) \quad \text{For concave } g(x) \tag{4.6}$$
$$\mathbb{E}\{g(x)\} \geq g(\mathbb{E}\{x\}) \quad \text{For convex } g(x) \tag{4.7}$$

4.1.1 Upper Bound

To upper bound (4.1) we consider the term added to 1 inside the log as the variable x in (4.6). Moreover, the radiation pattern points are always non-negative[2], so x is non-negative. The function $\log_2(1+x)$ has a second derivative $-1/((1+x)^2\ln 2)$ that is always negative for non-negative x, indicating concavity. Using Jensen's inequality, (4.1) is upper bounded as below

$$\begin{aligned}
\overline{C} &\leq \log_2\left(1+\mathbb{E}\left\{\frac{P_sS_R}{N_0+P_{I,1}I_{R,1}+\cdots+P_{I,n}I_{R,n}}\right\}\right) \\
&= \log_2\left(1+\mathbb{E}\{P_sS_R\}\,\mathbb{E}\left\{\frac{1}{N_0+P_{I,1}I_{R,1}+\cdots+P_{I,n}I_{R,n}}\right\}\right) \\
&= \log_2\left(1+\mathbb{E}\{P_sS_R\}\,\mathbb{E}\left\{\frac{1}{N_0+I_R}\right\}\right)
\end{aligned} \tag{4.8}$$

where $I_R = P_{I,1}I_{R,1}+\cdots+P_{I,n}I_{R,n}$

4.1.2 Lower Bound

To lower bound (4.1) we consider the term added to 1 inside the log as a variable $1/x$, that replaces x in (4.7). Moreover, the radiation pattern points are always non-negative[2], so x is non-negative. The function $\log_2(1+1/x)$ has a second derivative $(2x+1)/((1+x)^2x^2\ln 2)$ which is always positive for non-negative x, indicating convexity. Using Jensen, (4.1) is lower bounded as below;

$$\begin{aligned}
\overline{C} &\geq \log_2\left(1+\frac{1}{\mathbb{E}\left\{\frac{N_0+P_{I,1}I_{R,1}+\cdots+P_{I,n}I_{R,n}}{P_sS_R}\right\}}\right) \\
&= \log_2\left(1+\frac{1}{\mathbb{E}\{\frac{1}{P_sS_R}\}\,\mathbb{E}\{N_0+P_{I,1}I_{R,1}+\cdots+P_{I,n}I_{R,n}\}}\right) \\
&= \log_2\left(1+\frac{1}{\mathbb{E}\{\frac{1}{P_sS_R}\}\,\mathbb{E}\{N_0+I_R\}}\right) \qquad (4.9) \\
&= \log_2\left(1+\frac{1}{\mathbb{E}\{\frac{1}{P_sS_R}\}(N_0+\mathbb{E}\{I_{R,1}\}\sum_n P_{I,n})}\right) \qquad (4.10)
\end{aligned}$$

[2] As it is the square of the array factor, so the curve is always positive, with $(M-1)$ zeros.

where $\mathbb{E}\{I_{R,n}\}$ are equal for all n, so $I_{R,1}$ is used as a common factor.
Although the upper and lower bounds given in (4.8) and (4.9) respectively, may be evaluated by calculating $\mathbb{E}\{1/x\}$ as shown in Appendix B for the uniform distribution case independently of the weighting vector, the solution is dependent on the number of antenna elements and the final formula is complicated and does not give any insight. Moreover, for general distributions of the desired signal and the interfering signals, the bounds become analytically intractable. Therefore, another approach is proposed in the next section.

4.1.3 Approximation

This approach combines the two tricks used to upper and lower bound the mean capacity. First, we separate the expectation operators in the mean capacity expression as

$$\begin{aligned}\overline{C} &= \mathbb{E}\left\{\log_2\left(1+\frac{P_s S_R}{N_0+P_{I,1}I_{R,1}+\cdots+P_{I,n}I_{R,n}}\right)\right\} \\ &= \underset{I_R}{\mathbb{E}}\left\{\underset{S_R}{\mathbb{E}}\left\{\log_2\left(1+\frac{P_s S_R}{N_0+P_{I,1}I_{R,1}+\cdots+P_{I,n}I_{R,n}}\right)\right\}\right\} \end{aligned} \tag{4.11}$$

where the expectation operators are separated as s_0 and s_n are considered independent variables. Then we proceed to upper bound as in Subsection 4.1.1,

$$\overline{C} \leq \underset{I_R}{\mathbb{E}}\left\{\log_2\left(1+\frac{\mathbb{E}\{P_s S_R\}}{N_0+P_{I,1}I_{R,1}+\cdots+P_{I,n}I_{R,n}}\right)\right\} \triangleq \overline{C}_{UB}$$

Now we lower bound the obtained upper bound above as in Subsection 4.1.2,

$$\begin{aligned}\overline{C}_{UB} &\geq \log_2\left(1+\frac{\mathbb{E}\{P_s S_R\}}{\mathbb{E}\{N_0+P_{I,1}I_{R,1}+\cdots+P_{I,n}I_{R,n}\}}\right) \\ &= \log_2\left(1+\frac{\mathbb{E}\{P_s S_R\}}{\mathbb{E}\{N_0+I_R\}}\right) \qquad (4.12) \\ &= \log_2\left(1+\frac{\mathbb{E}\{P_s S_R\}}{N_0+\mathbb{E}\{I_{R,1}\}\sum_n P_{I,n}}\right) \triangleq \overline{C}_{Approx} \qquad (4.13)\end{aligned}$$

The order of the separated expectation operators in (4.11) does not matter, as it leads to the same results in (4.13) if reversed. In other words, lower bounding the upper bound, leads to the same result as upper bounding the lower bound.
The approximation formula of the true mean capacity obtained in (4.13) is of the same form as the optimization problem (3.17), and can be maximized in the same way using the Slepian beam, resulting in the following two expressions for the two interference cases described previously

$$\overline{C}_{Approx} = \log_2\left(1+\frac{\frac{P_s}{2W}\lambda_{max}(\mathbf{A}_s(W))}{N_0+\frac{1}{2(1-W)}\left(2-\lambda_{max}\left(\mathbf{A}_s(W)\right)\right)\sum_n P_{I,n}}\right) \quad \text{Case 1} \tag{4.14}$$

$$\overline{C}_{Approx} = \log_2\left(1+\frac{\frac{P_s}{2W}\lambda_{max}(\mathbf{A}_s(W))}{N_0+\sum_n P_{I,n}}\right) \quad \text{Case 2} \tag{4.15}$$

It is necessary to remember here that these equations are valid in case of the uniform distribution of signal and interference introduced in the beginning of this chapter. In the

most general case, when the distribution of signal and interference are arbitrary functions, then the approximation in (4.13) still represents a Rayleigh quotient but with different matrices (no longer the sinc matrices given in (3.14)). In this case, the solution is a *generalized* Slepian beam, not necessarily the exact "classical" Slepian beam described in this thesis, with its properties being valid for that specific distribution.
As (4.14) and (4.15) suggest, the Slepian beam maximizes the approximated mean capacity. In the next section, we investigate how close this approximation is to the true mean capacity.

4.1.4 Relation between Upper/Lower Bounds and the Approximation

To check how the approximation is related to the upper/lower bounds we use equations (4.8), (4.9) and (4.12) and rewrite them as below

$$\begin{aligned}
\text{UB} &= \log_2\left(1+\mathbb{E}\{P_sS_R\}\,\mathbb{E}\left\{\frac{1}{N_0+I_R}\right\}\right)\\
\text{LB} &= \log_2\left(1+\frac{1}{\mathbb{E}\left\{\frac{1}{P_sS_R}\right\}\mathbb{E}\{N_0+I_R\}}\right)=\log_2\left(\frac{\frac{1}{\mathbb{E}\{\frac{1}{P_sS_R}\}}+\mathbb{E}\{N_0+I_R\}}{\mathbb{E}\{N_0+I_R\}}\right)\\
\overline{C}_{Approx} &= \log_2\left(1+\frac{\mathbb{E}\{P_sS_R\}}{\mathbb{E}\{N_0+I_R\}}\right)=\log_2\left(\frac{\mathbb{E}\{P_sS_R\}+\mathbb{E}\{N_0+I_R\}}{\mathbb{E}\{N_0+I_R\}}\right)
\end{aligned}$$

To check how the approximation is related to the lower bound, we subtract them as below

$$\begin{aligned}
\overline{C}_{Approx}-\text{LB} &= \log_2\left(\frac{\mathbb{E}\{P_sS_R\}+\mathbb{E}\{N_0+I_R\}}{\mathbb{E}\{N_0+I_R\}}\cdot\frac{\mathbb{E}\{N_0+I_R\}}{\frac{1}{\mathbb{E}\left\{\frac{1}{P_sS_R}\right\}}+\mathbb{E}\{N_0+I_R\}}\right)\\
&= \log_2\left(\frac{\mathbb{E}\{P_sS_R\}+\mathbb{E}\{N_0+I_R\}}{\frac{1}{\mathbb{E}\left\{\frac{1}{P_sS_R}\right\}}+\mathbb{E}\{N_0+I_R\}}\right)
\end{aligned}$$

A function $g(x)=1/x$ is a convex function for non-negative x, so (4.7) holds, i.e.,

$$\mathbb{E}\{g(x)\}\geq g(\mathbb{E}\{x\})\quad\Longrightarrow\quad\mathbb{E}\left\{\frac{1}{P_sS_R}\right\}\geq\frac{1}{\mathbb{E}\{P_sS_R\}}\quad\Longrightarrow\quad\mathbb{E}\{P_sS_R\}\geq\frac{1}{\mathbb{E}\left\{\frac{1}{P_sS_R}\right\}}$$

This means the numerator inside the $\log_2$ function is always larger than the denominator. Hence the term inside the $\log_2$ function is always ≥ 1, hence

$$\begin{aligned}
\overline{C}_{Approx}-\text{LB}&\geq\log_2(1)=0\\
\overline{C}_{Approx}&\geq\text{LB}
\end{aligned}\tag{4.16}$$

Similarly, we investigate how the approximation is related to the upper bound as below

$$\text{UB}-\overline{C}_{Approx}=\log_2\left(\frac{1+\mathbb{E}\{P_sS_R\}\,\mathbb{E}\left\{\frac{1}{N_0+I_R}\right\}}{1+\mathbb{E}\{P_sS_R\}\frac{1}{\mathbb{E}\{N_0+I_R\}}}\right)$$

Again, a function $g(x) = 1/(x+a)$ is a convex function for non-negative x and a, then;

$$\mathbb{E}\{g(x)\} \geq g(\mathbb{E}\{x\}) \quad \Longrightarrow \quad \mathbb{E}\left\{\frac{1}{N_0+I_R}\right\} \geq \frac{1}{\mathbb{E}\{N_0+I_R\}}$$

This means the numerator inside the $\log_2$ function is always larger than the denominator. Hence the term inside the $\log_2$ function is always ≥ 1, and

$$\text{UB} - \overline{C}_{Approx} \geq \log_2(1) = 0$$

$$\text{UB} \geq \overline{C}_{Approx} \tag{4.17}$$

From (4.16) and (4.17)

$$\text{UB} \geq \overline{C}_{Approx} \geq \text{LB} \tag{4.18}$$

This means the approximation itself is still bounded by the upper and lower bounds, same as the true mean capacity. This also means the approximation is always closer to the true mean capacity than at least one of the bounds - the worst - if not both.
In the next section, we will show curves of the mean capacity, upper and lower bounds simulated numerically, and compare them to the approximated formula.

4.2 Comparison of Capacity Bounds

Figure 4.2 shows the mean capacity, mean capacity upper bound and mean capacity lower bound as a function of the interference power. They are calculated numerically[3], and compared to the approximation calculated both numerically and using closed forms given in (4.14) for case 1. For this figure, the number of antenna elements used is $M = 6$, the desired signal power $P_s = 1$, noise power $N_0 = 0.04$ and there is one interfering signal ($N = 1$) with power $P_{I,1}$ ranging from 0 to 0.5. Due to the numerical precision, the upper bound that is calculated numerically is slightly shifted downwards causing the approximation to exceed the upper bound at the beginning, however, this is not true in general as shown in the previous subsection, but just a precision error of the numerical calculations. Apart from that, it can be seen that the approximation acts as expected, bounded by the upper and lower bounds, and follows the mean capacity. Another observation is that the approximation coincides with the upper bound at $P_{I,1} = 0$. This can be seen analytically in (4.11). In the case of no interference, the expectation across the interference region $\mathbb{E}_{I_R}$ is not needed, and we end up only upper bounding the mean capacity. Finally, it can be seen that, for small values of interference power relative to signal power, the bounds and the approximation are very tight, however, increasing interference power gradually increases the gap between the mean capacity and the bounds/approximation.
Figure 4.3 shows curves of mean capacity, upper and lower bounds of the Slepian beam as well as DFT and Dolph-Chebyshev beams (marked SLP, DFT and CHB, respectively). For this figure, the number of antenna elements used is $M = 3$, the desired signal power $P_s = 1$, noise power $N_0 = 0.05$ and there is no interference (i.e., $P_I = 0$), known as a noise limited

[3] By numerically we mean discretization of the radiation pattern curve with acceptable rate and substituting all the points in the corresponding formula/function before averaging all the results. When there are two variables inside the expectation, Monte Carlo method is used to cover all possible combinations of the points of the two variables.

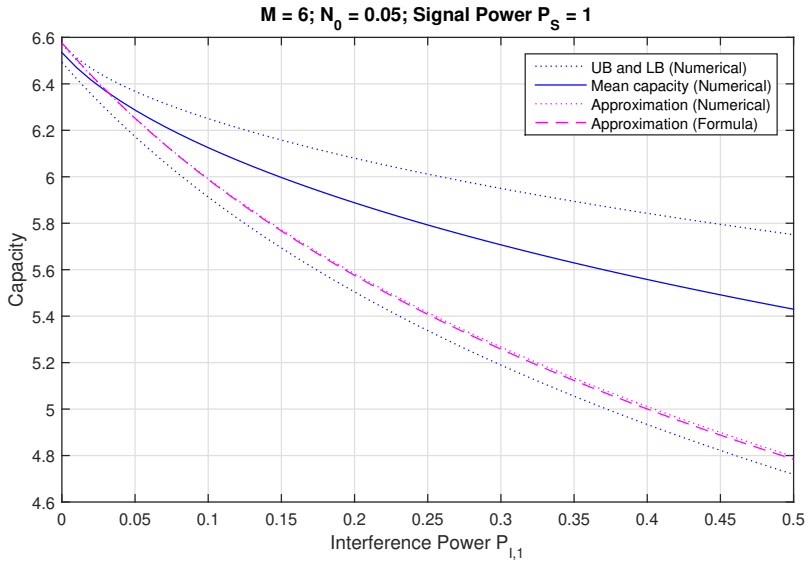

Figure 4.2: Capacity and capacity bounds (UB, LB and approximation) of the Slepian versus interference power.

scenario. The total region to be covered is divided into three sub-regions, hence $W = 0.333$ is the Slepian width that maximizes the approximation. As discussed previously, in the case of a noise limited scenario, the approximation coincides with the upper bound. The x-axis scans the width (W) in the case of Slepian, and the attenuation parameter α in the case of Dolph-Chebyshev. In the case of DFT, the x-axis does not scan anything as the DFT is not tuneable. The aim of this figure is to ensure that analytical analysis and insights agree with numerical calculations. This can be realized as below:
Firstly, all lower bounds of SLP, DFT and CHB beams are calculated using the formula in Appendix B. As stated before, the formula is independent of the weighting vector so that it works for all of the three beams. The curves coincide with the numerically calculated ones. Secondly, the approximation formula of the Slepian (the upper bound in the case of a noise limited scenario) coincides with the numerically calculated result, and is maximized at $W = 0.333$, exceeding the upper bound of DFT, and slightly higher than the upper bound of the CHB. The upper bound of the DFT is calculated both numerically and using a formula given in Appendix C, whereas the upper bound of the CHB is calculated only numerically. Thirdly, for $W \to 0$, the Slepian converges to the DFT. This can be seen as the upper/lower bounds and mean capacity curves of the SLP all converge to the upper/lower bounds and mean capacity curves of the DFT, respectively. For $W \to 1$ the SLP converges to the binomial beam, and so does the CHB at high values of attenuation parameter ($\alpha \to \infty$), as a result it can be seen that both converge to each other with increasing x-axis.
For all beams, the upper bound, lower bound and mean capacity follow each other, and how tight they are depends on how flat the beam pattern is inside the signal region. The more flat it is the tighter the bounds. A good measure of flatness of the pattern is the variance of its points inside signal region and interference region. The smaller the variance

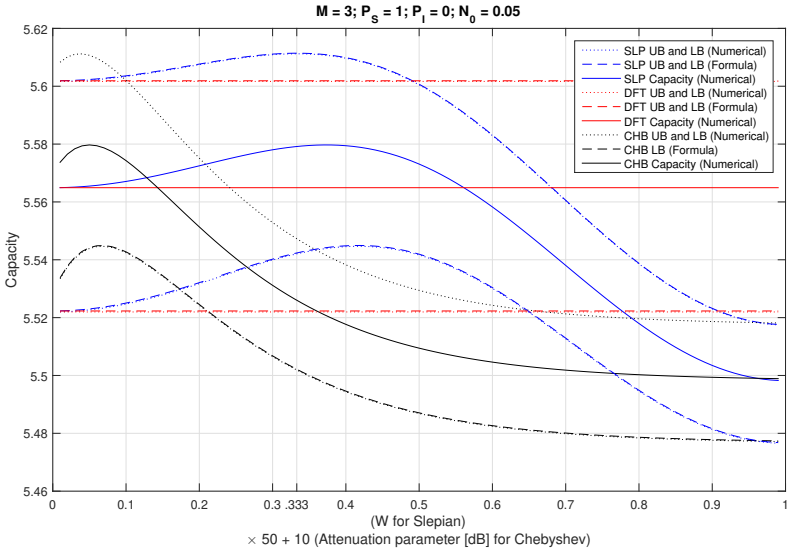

Figure 4.3: Comparison between capacity of Slepian beam and different beam synthesizers in a noise limited scenario.

is the tighter the bounds.

Finally, although the Slepian upper bound is maximized at $W = 0.333$, the capacity maximum peak is a little shifted (approx at $W = 0.3667$) and the lower bound maximum is also shifted (approx at $W = 0.43$). The SLP capacity at its maximum exceeds the DFT capacity, and is the same as CHB capacity. Although SLP is expected to perform better than CHB, this could not be seen here because the small number of antenna elements makes the gain unnoticeable. However, at higher number of antenna elements it is noticeable, as will be seen in the next figure.

Figure 4.4 uses the same configuration as the previous one, except for the number of antenna elements ($M = 8$). It is noticeable here that the upper bound, lower bound and mean capacity of SLP exceed those of CHB, unlike in the previous figure.

Figure 4.5 shows an interference limited scenario. In this figure, the number of antenna elements used is $M = 5$, the desired signal power $P_s = 1$, noise power $N_0 = 0.1$ and one interfering signal is assumed ($N = 1$) with power $P_{I,1} = 0.6$. In the presence of interference, the SLP capacity approximation is not the upper bound anymore, and can be seen as a different curve in the figure. The total region that needs to be covered is divided into 5 sub-regions. Hence $W = 0.2$ is the Slepian width that maximizes the approximation.

At the selected value of $W = 0.2$, the corresponding capacity of SLP exceeds both the DFT capacity and the global maximum of the CHB capacity, showing benefit from using Slepian over both DFT and CHB beams. However, the maximum peak of the SLP capacity happens at a shifted width (approx at $W = 0.34$) with even more gain than those of DFT and CHB. However, this thesis does not study exactly where this peak is located (i.e., which width achieves this peak), and it is suggested to use $W = 0.2$, which still gives better capacity result than those of the other beams. This investigation is left for future work.

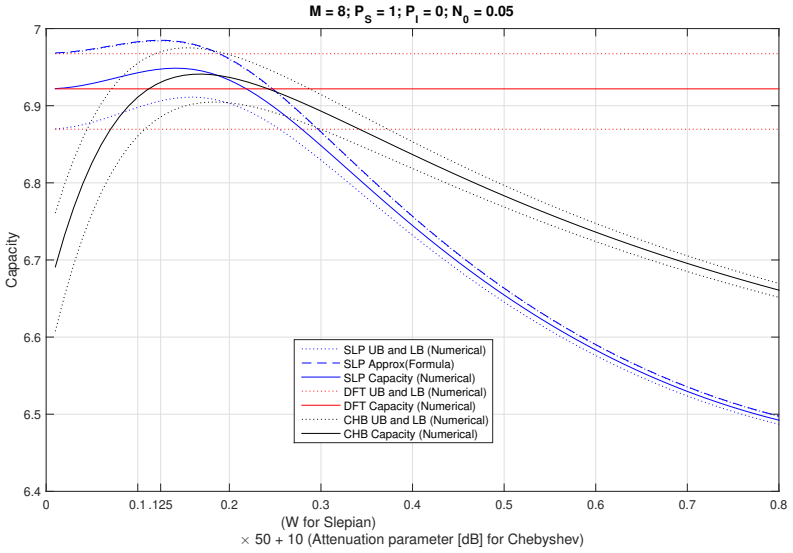

Figure 4.4: Comparison between capacity of Slepian beam and different beam synthesizers in a noise limited scenario.

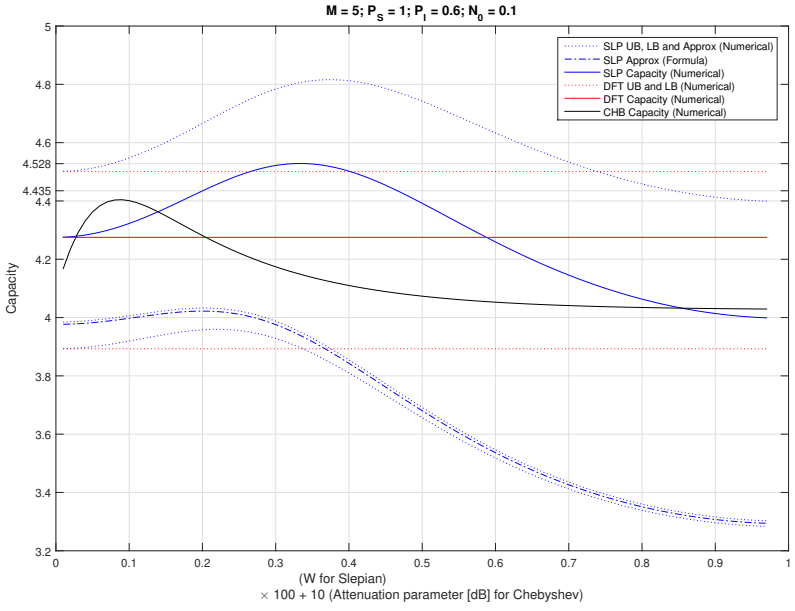

Figure 4.5: Comparison between capacity of Slepian beam and different beam synthesizers in an interference limited scenario.

4.3 Outage Capacity

$C_{out,q}$ ($q\%$ outage capacity) is defined as the information rate that is guaranteed for $(100-q)\%$ of the realizations, i.e., $Pr(C \leq C_{out,q}) = q\%$ [25]. Using this definition, we can start as the following

$$Pr(C \geq C_{out,q}) = 1 - \frac{q}{100} \tag{4.19}$$

Now we plug in the left hand side, the capacity formula given in (4.1) but omit the expectation operator as we are working with the capacity and not its mean

$$\begin{aligned} Pr\left(\log_2 \left(1 + \frac{P_s \mathbf{v}^H \mathbf{A}(s_0)\mathbf{v}}{N_0 + \mathbf{v}^H \Big(\sum_n P_{I,n} \mathbf{A}(s_n) \Big) \mathbf{v}} \right) \geq C_{out,q} \right) &= 1 - \frac{q}{100} \\ Pr\left(\left(\frac{P_s \mathbf{v}^H \mathbf{A}(s_0)\mathbf{v}}{N_0 + \mathbf{v}^H \Big(\sum_n P_{I,n} \mathbf{A}(s_n) \Big) \mathbf{v}} \right) \geq 2^{C_{out,q}} - 1 \right) &= 1 - \frac{q}{100} \end{aligned}$$

Let $\tilde{c} = 2^{C_{out,q}} - 1$, and as before $S_R = \mathbf{v}^H \mathbf{A}(s_0)\mathbf{v}$ is the radiation pattern inside the signal region, and $I_{R,n} = \mathbf{v}^H \mathbf{A}(s_n)\mathbf{v}$ where $n = 1, 2, \ldots, N$ is the radiation pattern inside the interference region.

$$\begin{aligned} Pr\left(P_s S_R \geq \tilde{c} \Big(N_0 + \Big(\sum_n P_{I,n} I_{R,n} \Big) \Big) \right) &= 1 - \frac{q}{100} \\ Pr\left(\Big(P_s S_R - \tilde{c} \Big(\sum_n P_{I,n} I_{R,n} \Big) \Big) \geq \tilde{c} N_0 \right) &= 1 - \frac{q}{100} \end{aligned}$$

As long as $C_{out,q} > 0$ then $\tilde{c} > 0$. Using Markov-Chebyshev inequality, stating that $Pr(X \geq a) \leq \frac{\mathbb{E}\{X\}}{a}$ for any $a > 0$, we get

$$\begin{aligned} Pr\left(\Big(P_s S_R - \tilde{c} \Big(\sum_n P_{I,n} I_{R,n} \Big) \Big) \geq \tilde{c} N_0 \right) &\leq \frac{\mathbb{E}\left\{ P_s S_R - \tilde{c} \Big(\sum_n P_{I,n} I_{R,n} \Big) \right\}}{\tilde{c} N_0} \\ &= \frac{P_s \mathbb{E}\{S_R\} - \tilde{c} \Big(\sum_n P_{I,n} \mathbb{E}\{I_{R,n}\} \Big)}{\tilde{c} N_0} \end{aligned} \tag{4.20}$$

We know from Chapter 3 that the Slepian beam maximizes $\mathbb{E}\{S_R\}$, and minimizes $\mathbb{E}\{I_{R,n}\}$ in interference distribution of case 1, otherwise $\mathbb{E}\{I_{R,n}\}$ is constant in case 2. In both cases, the Slepian beam pushes the upper bound of the outage capacity in (4.20) to its maximum, giving more margin to the probability that the capacity is higher than the outage capacity. In case of general distributions of the desired and interference signals, the *generalized* Slepian beam mentioned in Subsection 4.1.3 maximizes the upper bound in (4.20).

Chapter 5
Simulation Results

This chapter provides system level simulation results relating to the proposed Slepian beam concept presented earlier in this thesis. Two algorithms have been written in MATLAB and are incorporated in the *System Simulator* for performance assessment. The algorithms are:

- Beam sweeping algorithm
- Codebook generation algorithm

The beam sweeping algorithm implements the hierarchical search method. The codebook generation algorithm uses the MSE metric to design beam pattern that is then shifted to cover the whole phase region.

5.1 Simulation Environment

This section describes the simulation setup and operation of the *System Simulator* [26] used to generate the figures depicted in this chapter. The *System Simulator* simulates 19 sites, with 3 cells per site. Simulation is performed by randomly dropping UEs into the system and assigning each UE to its nearest cell in terms of RF distance. RF distance is defined as the gain that is between a cell and the UE, which consists of the path loss, the antenna gain and Rayleigh fading. Once each UE is assigned to a cell (for simplicity, we only consider a single UE per cell), all cells transmit simultaneously to their assigned UEs during a single time unit (e.g. a single 10 ms frame in 3GPP NR) – hence, we assume a full buffer traffic model. These simultaneous transmissions cause interference at the UEs. The transmitted packets from each cell consist basically of a transmission power (according to the simulation setup in Table 5.1) and a beam chosen by the cell that is directed toward its intended UE. A packet from a cell is propagated to all UEs in the system, through the UMa LOS channels between that cell and all the UEs, which results in that each UE observes its desired signal together with interfering signals from all other cells in the system. In order to reduce complexity, we focus on a single UE that is attached to a cell in the middle of the system, which corresponds to the wrap around methodology when performing system simulations. The signal at this UE is received with receive beamforming, from which the SINR can be calculated. In total, we have 2000 independent repetitions of this procedure, i.e., we have 2000 independent drops, which gives a total of 2000 SINR values.
The beam weights applied to the antenna array must satisfy two hardware constraints: per antenna power constraint and amplitude quantization. The per antenna power constraint

limits our beam weights to have at most an amplitude equal to 1 on each antenna element. The amplitude quantization constraint limits the possible values that the amplitude can take, and in our setting the amplitudes are of the form $10^{-k/20}$, where $k \geq 0$ is an integer. The value of k is chosen such that $10^{-k/20}$ is as close as possible to the true value of the beam amplitude at a specific antenna. This choice results in that we have a 1 dB resolution on the power of each beam weight amplitude.

Table 5.1: Simulation setup. [Table source: [16] modified as per our needs]

Parameter	**Values**
Scenarios	UMa - LOS
Sectorization	3 sectors per cell site: 30, 150 and 270 degrees 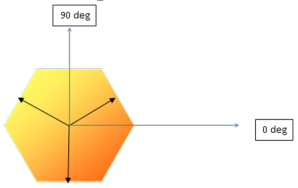
BS antenna configurations	$M_g = N_g = 1$; (M,N,P) = (8, 8, 1), $d_V = 0.5\lambda$
BS port mapping	The 64 elements are mapped to a single CRS port
BS antenna electrical downtilting	6 degrees downward tilt of boresight vector
Antenna virtualization	DFT and Slepian beams
BS Tx power	46 dBm
UT antenna configurations	$M_g = N_g = 1$; (M,N,P) = (4, 4, 1), $d_V = 0.5\lambda$
UT distribution	Uniform within the hexagon inscribing all sites
UT attachment	Based on pathloss and antenna gain
UT noise figure	7 dB
Fast fading channel	Fast fading channel is not modeled
Carrier Frequency	5 GHz, 28 GHz, 60GHz
Wrapping method for UMa and UMi	geographical distance based wrapping (mandatory)
BS height	25 meter
UE height	1.5 meter

5.2 Simulation Figures

The rest of this chapter presents simulation results according to the simulation assumptions outlined in Table 5.1, where the 3GPP wireless channel model [16] is used. The performance is evaluated with the cumulative distribution function (CDF) of SINR and spectral efficiency. The following information apply to all the figures in this chapter:

- f_c stands for carrier frequency.
- ISD stands for inter-site distance.
- At the BS, the beam chosen from the BS codebook is the one with the largest beamforming gain towards the LOS path.
- The spectral efficiency showed in the figures is calculated as $Spectral\ Efficiency\ [bits/s/Hz] = \log_2(1 + SINR)$

5.2.1 Exhaustive/Hierarchical Beam Sweeping

This subsection compares and comments on the simulation results obtained using exhaustive and hierarchical beam sweeping methods discussed in Section 2.3. The exhaustive beam sweeping method measures all beams one by one in one stage, while the hierarchical method measures wide beams, then narrower and narrower beams over multiple stages. In our simulations, two stages are considered for hierarchical beam sweeping. In early stages, wide beams may collect interference causing the algorithm not to select the beam region where the optimal narrow beam is located. This may cause mis-detection and eventually when the algorithm finishes, the selected beam direction may not be optimal. This issue does not exist in the exhaustive beam sweeping method because it uses the narrowest beams directly. Therefore, the performance of the exhaustive beam sweeping method is expected to be higher than the hierarchical one. However, this assumed increase in the probability of mis-detection is not studied in this thesis analytically. Moreover, the simulation results show that this loss in performance is negligible.

Figure 5.1 shows the CDF of the SINR for both the DFT and Slepian beams, using Exhaustive and Hierarchical beam sweeping. Exhaustive beam sweeping performs slightly better than Hierarchical beam sweeping. In this figure, each stage of the Hierarchical sweeping method consists of 4 beams covering the space. This is increased to 9 beams in Figure 5.2 leading to less loss in performance between Exhaustive and Hierarchical. This can be explained as following: increasing the number of beams in each stage reduces the collected interference and reduces the probability of mis-detection, especially in the first stage of the Hierarchical searching. In Figure 5.1 the $q\%$ outage SINR ($SINR_{out,q}$) is $\simeq$ 1dB higher for Exhaustive than Hierarchical when using DFT beams. This can be seen for $q = 0$ up to 90%, above that this difference starts to shrink. On the other hand, when using Slepian beams, $SINR_{out,q}$ almost coincides for Exhaustive and Hierarchical, with the former showing slight increase (< 0.5dB) for $q = 50 - 90\%$. Interestingly, using Slepian-Hierarchical gives the same $SINR_{out,q}$ as DFT-Exhaustive for $q = 0$ up to 50%, above that Slepian-Hierarchical shows improvement of up to 1.5dB compared to DFT-Exhaustive. For instance, the figure shows $SINR_{out,60}$ is 10dB for Slepian-Hierarchical and 9dB for DFT-Exhaustive. This translates into that 40% of the time Slepian-Hierarchical's received SINR is at least 10dB, whereas DFT-Exhaustive's received SINR is at least 9dB. In Figure 5.2, the difference in $SINR_{out,q}$ is unnoticeable between Exhaustive and Hierarchical when using DFT or Slepian beams. Moreover, using Slepian offers $\simeq$ 1dB increase compared to DFT for high q (higher than 50%).

On the other hand, the gain in IA time is as follows. For a 4×4 UPA at the UE, exhaustive sweeping using a 16-beam codebook requires 16 different measurements. However, the number of measurements is reduced to 8 when using hierarchical sweeping with two stages and 4 beams per stage. Hence, a saving of 50% in IA time can be achieved with hierarchical search, while both have roughly the same performance as shown in Figure 5.1. Similarly, for a 4×4 UPA at the UE, exhaustive sweeping using an 81-beam over-sampled codebook requires 81 different measurements. However, the number of measurements is reduced to only 18 when using hierarchical sweeping with two stages and 9 beams per stage. Hence, the saving is $100 \times (1 - {}^{18}/_{81}) = 78\%$, while both have roughly the same performance as shown in Figure 5.2.

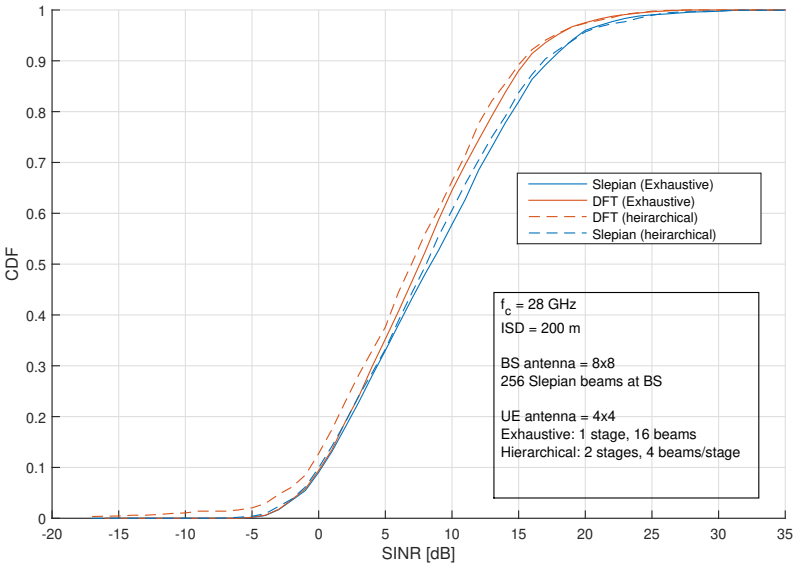

Figure 5.1: CDF of received SINR using exhaustive/hierarchical beam sweeping using DFT/Slepian beams, and a 16-beams codebook is used at the UE.

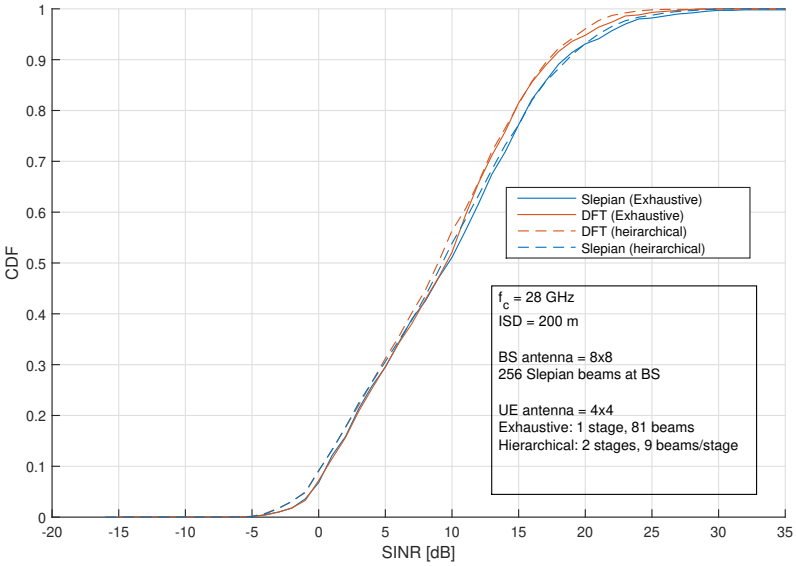

Figure 5.2: CDF of received SINR using exhaustive/hierarchical beam sweeping with DFT/Slepian beams, and an 81-beam codebook is used at the UE.

5.2.2 Slepian/DFT at UE

This subsection shows the benefit of using Slepian beam over DFT beam at the UE in terms of ergodic spectral efficiency. In Figure 5.3, two-stage hierarchical beam sweeping is used at the UE with Slepian and DFT beams, while the BS uses 64 DFT beams, which are increased to 256 DFT beams in Figure 5.4. The comparison is held in both figures for different numbers of beams per stage at the UE (4, 9 and 16 beams/stage). This shows how the Slepian beam at the UE has more potential to achieve higher ergodic spectral efficiency for different beam configurations than the DFT beam. In addition, it also shows how the performance is increased as the number of beams per stage increases. Figure 5.5 shows the performance of the latter case (256 DFT beams at the BS), but using SINR instead of ergodic spectral efficiency.

The capacity performance of Slepian/DFT with two-stage Hierarchical sweeping at the UE is given in Figure 5.3. For 4 beams/stage, Slepian achieves $\simeq$ 1bits/s/Hz higher than DFT. This difference is reduced to $\simeq$ 0.5bits/s/Hz for 9 beams/stage, and $\leq$ 0.5bits/s/Hz for 16 beams/stage. This reduction in difference can be explained as the increasing of the number of beams per stage leads to the over-sampling of the angular space, allowing the beam to better align with the incoming signal. This improves the performance of the DFT beam as the incoming signal comes closer to the beam peak - which is the highest possible peak -. However, DFT still cannot perform better than Slepian that suppresses interference. In general, over-sampling the space increases the ergodic spectral efficiency for both beams. In the figure, Slepian 16 beams/stage is $\simeq$ 0.5bits/s/Hz higher than 9 beams/stage, and the latter is $\simeq$ 0.5bits/s/Hz higher than 4 beams/stage. Comparing to DFT, Slepian 4 beams/stage is better than DFT 4 beams/stages, and has almost the same performance as DFT 9 beams/stage. Slepian 9 beams/stage performs better than DFT 4, 9 and 16 beams/stage. This implies that the Slepian beams using less number of beams/stage than DFT not only significantly reduce the IA time, but also achieve significantly better performance than the DFT beams. Slepian 16 beams/stage perform better than all other configurations in this simulation. Some typical values from the figure: 50% of the time, Slepian 16 beams/stage guarantees $\simeq$ 2.9bits/s/Hz, Slepian 9 beams/stage and DFT 16 beams/stage guarantees $\simeq$ 2.6bits/s/Hz, Slepian 4 beams/stage and DFT 9 beams/stage guarantees $\simeq$ 2.4bits/s/Hz and DFT 4 beams/stage guarantees $\simeq$ 1.5bits/s/Hz.

In Figure 5.4, the number of beams at the BS is increased to 256 DFT beams. This makes the BS Angle of Departure (AoD) more aligned to the LOS direction, delivering higher power. However, this doesn't affect the BS beamwidth, so the incoming LOS cluster at the UE is expected to have the same angular scattering as for the previous case (64 DFT beams at the BS). In this figure, Slepian 4 beams/stage achieves $\leq$ 1.5bits/s/Hz higher than DFT 4 beams/stage. This difference shrinks to $\leq$ 1bits/s/Hz for 9 and 16 beams/stage. The gain of increasing beams/stage is almost the same when using Slepian and DFT. This gain is $\simeq$ 1.5bits/s/Hz and $\simeq$ 0.25bits/s/Hz when increasing from 4 to 9, and from 9 to 16 beams/stage, respectively. In general, all curves are shifted to the right (i.e., higher spectral efficiency) compared to the case of 64 DFT beams at the BS in Figure 5.3. Again, we notice here that Slepian 9 beams/stages performs better than DFT 16 beams/stage. Typical values from the figure for 50% outage spectral efficiency: Slepian 16 beams/stage guarantees $\simeq$ 5.6bits/s/Hz, Slepian 9 beams/stage guarantees $\simeq$ 5.3bits/s/Hz and Slepian 4

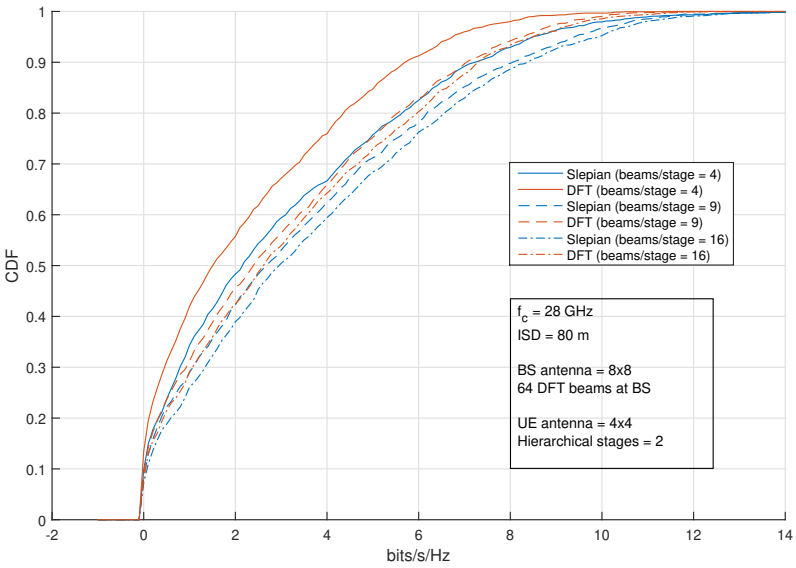

Figure 5.3: CDF of ergodic spectral efficiency of Slepian/DFT beams at the UE with hierarchical sweep 4/9/16 beams/stage. 64 DFT beams at the BS.

beams/stage guarantees $\simeq$ 4.2bits/s/Hz. For DFT, 16 beams/stage guarantees $\simeq$ 5bits/s/Hz, 9 beams/stage guarantees $\simeq$ 4.8bits/s/Hz and 4 beams/stage guarantees $\simeq$ 3.4bits/s/Hz.

Figure 5.5 shows received SINR instead of ergodic spectral efficiency to give the feeling of how the link budget is affected. All the observations in the previous paragraph are valid here, we just list corresponding values of SINR. Slepian 4 beams/stage achieves $3-5$dB higher SINR than DFT 4 beams/stage. This difference shrinks to $\leq$ 3dB for 9 and 16 beams/stage. The gain of increasing the number of beams/stage is almost the same when using Slepian and DFT. This gain is $\simeq$ 4dB and $\simeq$ 1dB when increasing from 4 to 9, and from 9 to 16 beams/stage, respectively. Typical values from the figure for 50% guaranteed SINR are: For Slepian, 16 beams/stage guarantees $\simeq$ 16.5dB, 9 beams/stage guarantees $\simeq$ 15.5dB and 4 beams/stage guarantees $\simeq$ 12dB. For DFT, 16 beams/stage guarantees $\simeq$ 14.5dB, 9 beams/stage guarantees $\simeq$ 14dB and 4 beams/stage guarantees $\simeq$ 9.5dB.

5.2.3 Slepian/DFT at UE and BS

The previous subsection discussed how using the Slepian beam at the UE improves the performance. Although the codebook at the BS is not in the scope of this thesis, this subsection shows even more improvement in performance by employing the Slepian beam at the BS too. In Figure 5.6, two-stage hierarchical beam sweeping is used at the UE with Slepian and DFT beams, whereas the BS uses 64 Slepian beams, which are increased to 256 Slepian beams in Figure 5.7. The comparison is made in both figures for different

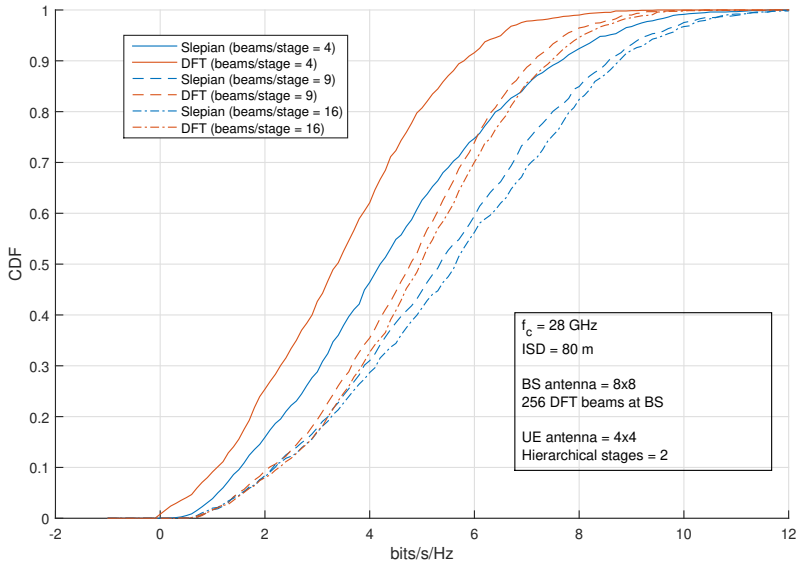

Figure 5.4: CDF of ergodic spectral efficiency of Slepian/DFT beams at the UE with hierarchical sweep 4/9/16 beams/stage. 256 DFT beams at the BS.

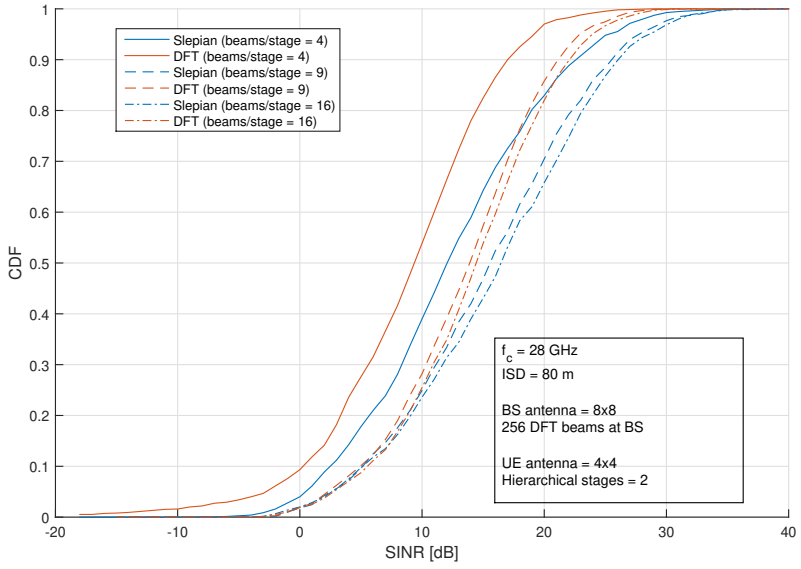

Figure 5.5: CDF of received SINR of Slepian/DFT beams at the UE with hierarchical sweep 4/9/16 beams/stage. 256 DFT beams at the BS.

numbers of beams per stage at the UE. Slepian beams at the UE and BS have even more potential to achieve higher ergodic spectral efficiency at different beam configurations than the DFT at any/both of them. Figure 5.8 shows the performance of the latter case (265 Slepian beams showed in Figure 5.7), but using SINR instead of spectral efficiency. Figure 5.9 shows four curves of CDF of spectral efficiency when using Slepian/DFT at the UE/BS. The best combination in performance is Slepian at both sides, and the least is DFT at both sides. In this figure, the BS uses 64 beams, and the UE uses 2 stages, 4 beams/stage.

Comparing Figures 5.3 and 5.6, in Figure 5.6 the curves are shifted to the right (better performance). Slepian/DFT with two-stage hierarchical sweeping at the UE offers the following results. For 4 beams/stage, Slepian achieves $\simeq$ 1.2bits/s/Hz higher capacity than DFT. This difference is reduced to $\simeq$ 1bits/s/Hz for 9 beams/stage, and $\leq$ 0.5bits/s/Hz for 16 beams/stage. For the Slepian beam, 16 beams/stage gives $\simeq$ 0.25bits/s/Hz higher capacity than 9 beams/stage, and the latter is $\simeq$ 1bits/s/Hz higher than 4 beams/stage. Comparing to DFT, Slepian 4 beams/stage is better than DFT 4 beams/stages, and it almost has same performance as DFT 9 beams/stage. Slepian 9 beams/stage performs better than DFT 4/9/16 beams/stage, with $\simeq$ 0.8bits/s/Hz higher capacity than the latter, and $\simeq$ 2.2bits/s/Hz than the former. Slepian 16 beams/stage performs better than all other configurations in this simulation. Some typical values from the figure are: 50% of the time, Slepian 9/16 beams/stage guarantees $\simeq$ 4.5bits/s/Hz, Slepian 4 beams/stage guarantees $\simeq$ 3.4bits/s/Hz (higher than the same case but with DFT at the BS, which was $\simeq$ 2.9bits/s/Hz). For DFT, 16/9/4 beams/stage guarantee $\simeq$3.9/3.7/2.4 bits/s/Hz, respectively.

In Figure 5.7, the number of Slepian beams at the BS is increased to 256. We also compare this figure with the corresponding Figure 5.4. In Figure 5.7, Slepian 4 beams/stage achieves $\simeq$ 1.5bits/s/Hz higher capacity than DFT 4 beams/stage. This difference shrinks to $\leq$ 1bits/s/Hz and $\leq$ 0.75bits/s/Hz for 9 and 16 beams/stage, respectively. The gain of increasing beams/stage is now lower using Slepian than DFT. For Slepian, this gain is $\simeq$ 0.7bits/s/Hz and $\simeq$ 0.5bits/s/Hz when increasing from 4 to 9, and from 9 to 16 beams/stage, respectively. For DFT, the gain is $\simeq$ 1.2bits/s/Hz and $\simeq$ 0.5bits/s/Hz when increasing from 4 to 9, and from 9 to 16 beams/stage, respectively. In general, all curves are very slightly shifted right or not at all (i.e., slight or no improvement in spectral efficiency) than in the case of 64 Slepian beams at the BS in Figure 5.6. Typical values from the figure for 50% outage spectral efficiency are: Slepian 16 beams/stage guarantees $\simeq$ 5.6bits/s/Hz, Slepian 9 beams/stage guarantees $\simeq$ 5.3bits/s/Hz and Slepian 4 beams/stage guarantees $\simeq$ 4.5bits/s/Hz, which are the same as 64 Slepian beams at the BS - except that 4 beams/stage is slightly improved -, suggesting no improvement by over-sampling at the BS. For DFT, 16 beams/stage guarantees $\simeq$ 5.1bits/s/Hz, 9 beams/stage guarantees $\simeq$ 4.7bits/s/Hz and 4 beams/stage guarantees $\simeq$ 3.5bits/s/Hz, with each of the three cases having $\simeq$ 0.1bits/s/Hz increase relative to 64 Slepian beams at the BS.

In Figure 5.8 we show received SINR instead of ergodic spectral efficiency to get the feeling of how much the link budged is affected. All the observations in the previous paragraph are valid here, we just list some corresponding values of SINR. Slepian 4 beams/stage achieves $3-6$dB higher SINR than DFT 4 beams/stage. This difference shrinks to $\leq$ 3dB 9 and 16 beams/stage. The gain of increasing beams/stage is now lower using Slepian than DFT. For Slepian, this gain is $\simeq$ 2dB and $\simeq$ 1dB when increasing from 4 to 9, and from 9

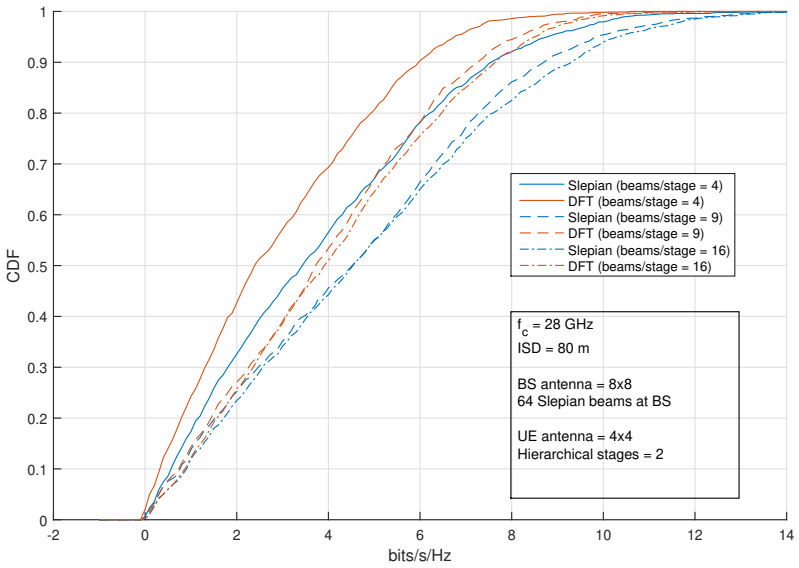

Figure 5.6: CDF of ergodic spectral efficiency of Slepian/DFT beams at the UE with hierarchical sweeping 4/9/16 beams/stage. 64 SLP beams at the BS.

to 16 beams/stage, respectively. For DFT, the gain is $\simeq$ 4dB and $\simeq$ 1dB when increasing from 4 to 9, and from 9 to 16 beams/stage, respectively. Typical values from the figure for 50% guaranteed received SINR are given as follows. For Slepian, 16 beams/stage guarantees $\simeq$ 16.5dB, 9 beams/stage guarantees $\simeq$ 15.5dB and 4 beams/stage guarantees $\simeq$ 13dB. For DFT, 16 beams/stage guarantees $\simeq$ 15dB, 9 beams/stage guarantees $\simeq$ 14dB and 4 beams/stage guarantees $\simeq$ 10dB.

Figure 5.9 shows the ergodic capacity performance for 64-beam codebook at the BS, and hierarchical two-stage codebook with 4 beams/stage at the UE. Slepian at the UE and BS shows up to $\simeq$ 2bits/s/Hz capacity increase compared to DFT at the UE and BS, which is close to 100% increase for this antenna configuration. Slepian at the UE and BS shows on average $\simeq$ 1.2bits/s/Hz capacity increase than DFT at either the UE or BS, which is close to 50% increase for this antenna configuration. For Slepian at the UE with DFT at the BS, the capacity converges to the case of Slepian at both sides at high values of q, whereas it converges to the case of DFT at both sides at low values of q. For DFT at the UE with Slepian at the BS, the capacity converges to the case of DFT at both sides at high values of q, whereas it converges to the case of Slepian at both sides at low values of q. Some typical values from the figure for 50% outage spectral efficiency are: Slepian beams at both sides offers $\simeq$ 3.5bits/s/Hz, DFT beams at both sides provides $\simeq$ 1.5bits/s/Hz, Slepian at the BS and DFT at the UE gives $\simeq$ 2.4bits/s/Hz, and DFT at the BS and Slepian at the UE facilitates $\simeq$ 2.1bits/s/Hz.

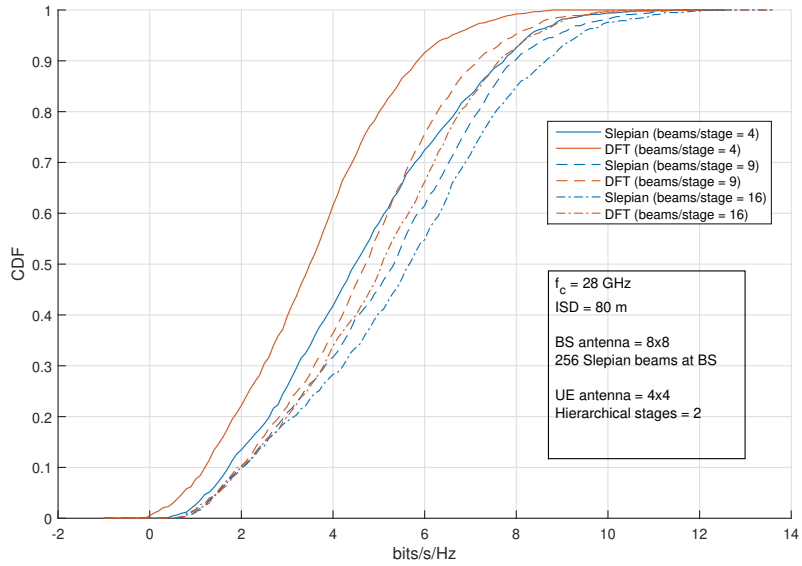

Figure 5.7: CDF of ergodic spectral efficiency of Slepian/DFT beams at the UE with hierarchical sweeping 4/9/16 beams/stage. 256 SLP beams at the BS.

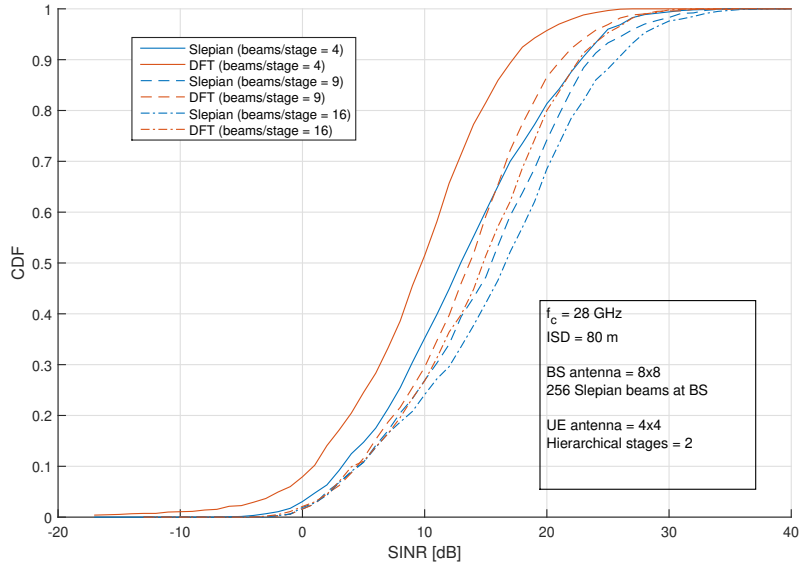

Figure 5.8: CDF of received SINR of Slepian/DFT beams at the UE with hierarchical searching 4/9/16 beams/stage. 256 SLP beams at the BS.

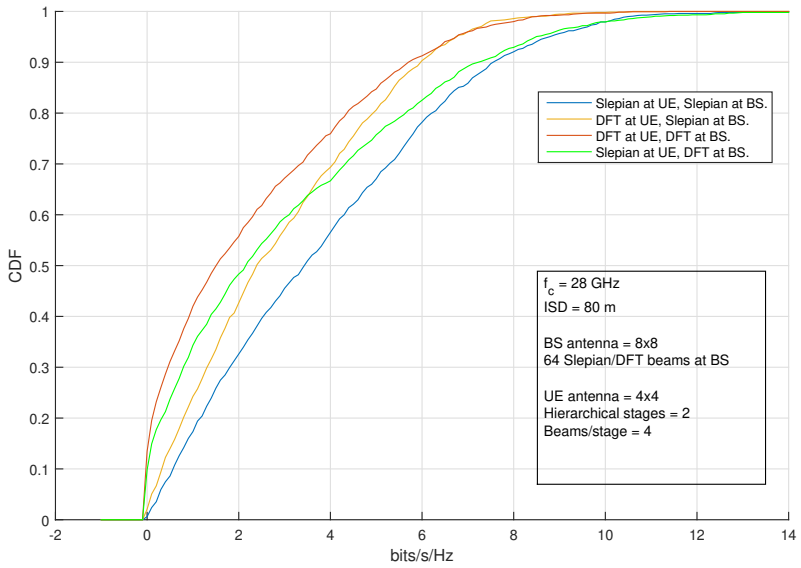

Figure 5.9: CDF of ergodic spectral efficiency of Slepian/DFT beams at the UE/BS. 64 beams at the BS. Two-stages hierarchical sweeping at the UE.

5.2.4 Inter-Site Distance Effect

Inter-site distance (ISD) is the average distance between a site and its neighboring sites, and is directly related to the interference levels. The longer the distance, the lower the interference levels and vice versa. Moreover, we have discussed that although the Slepian beam shows better performance than DFT in a noise limited scenario, it shows even better performance in an interference limited scenario. Two values of ISD have been selected in the simulation to represent highly interfered network (ISD = 80 meter) and low interference network (ISD = 200 meter). Figures 5.10 and 5.11 show the gain obtained by using Slepian beams over DFT beams in those two cases, respectively. The performance is compared using the CDF of the received SINR. It can be observed that the gain obtained by using Slepian over DFT shrinks for larger ISD distance.

Figure 5.10 shows the highly interfered network. A gain of 3-5 dB is obtained when using Slepian over DFT for 4 beams/stage. A gain of 0-4 dB is obtained when using Slepian over DFT for 9 beams/stage. Typical values from the figure for 50% outage received SINR are: 9.5dB for DFT 4 beams/stage, 14dB for DFT 9 beams/stage, 12dB for Slepian 4 beams/stage, and 15.5dB for Slepian 9 beams/stage.

Figure 5.11 shows the low interference network. A gain of 1-2 dB is obtained when using Slepian over DFT for 4 beams/stage. A gain of 0-1 dB is obtained when using Slepian over DFT for 9 beams/stage. Typical values from the figure for 50% outage

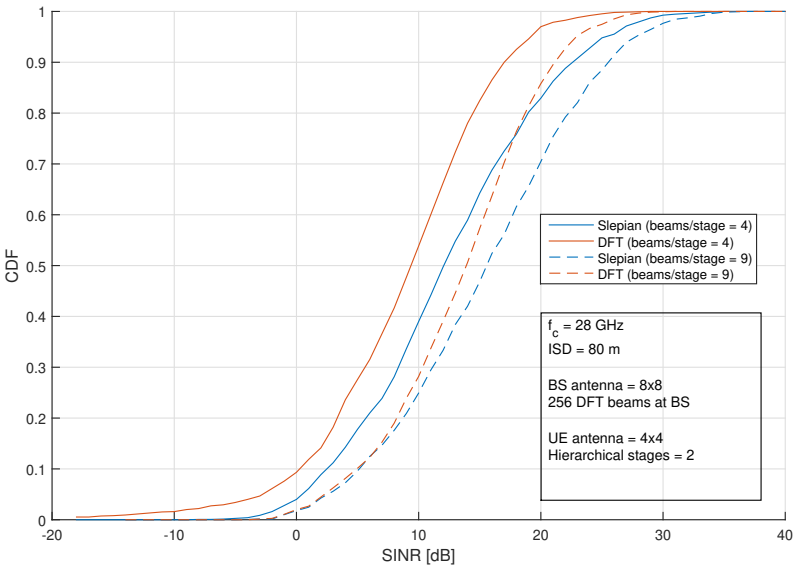

Figure 5.10: CDF of received SINR of Slepian/DFT beams at the UE and 256 DFT beams at the BS in a network with ISD = 80 meters.

received SINR are: 7dB for DFT 4 beams/stage, 9dB for DFT 9 beams/stage, 8dB for Slepian 4 beams/stage, and 9.5dB for Slepian 9 beams/stage. The gain obtained by using Slepian over DFT shrinks in this case compared to the highly interfered case. However, the absolute values in highly interfered case are higher than this case because of the higher density of sites, which results in that the UE is closer to its site and therefore experiences less path loss.

5.2.5 Carrier Frequency Effect

To see how the carrier frequency affects the gain obtained using Slepian beams over DFT beams, simulation results for downlink carrier frequencies f_c = 5 GHz and f_c = 28 GHz are shown in Figures 5.12 and 5.13, respectively. It is important to mention that the separation distance between the antenna elements is kept to half of the wavelength in both cases. Moreover, both simulations were run for LOS the case. The results suggest that there is no significant difference from using a different carrier frequency. This is due to the LOS channel assumption used in the simulation regardless of the carrier frequency. The only thing that changes with carrier frequency is the gain of each channel. As can be seen, the gain changes due to carrier frequency do not have a significant impact in this case (LOS regardless carrier frequency). Finally, it is noted that the same observations apply when the simulation was run at the carrier frequency f_c = 60 GHz.

Figures 5.12 and 5.13 are roughly the same with these typical values for 50% outage

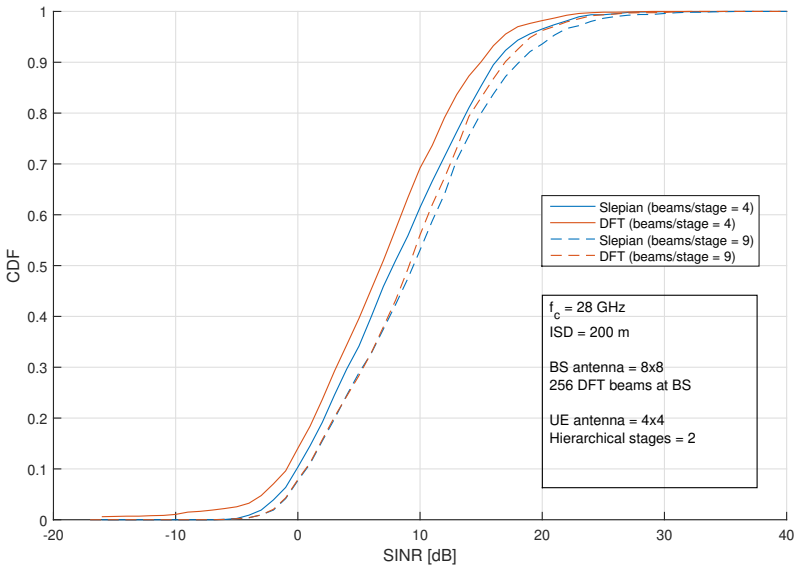

Figure 5.11: CDF of received SINR of Slepian/DFT beams at the UE and 256 DFT beams at the BS in a network with ISD = 200 meters.

spectral efficiency. Slepian beams codebook at the UE with 4/9/16 beams/stage gives $\simeq$ 4.2 - 5.3 - 5.6 bits/s/Hz. DFT beams codebook at the UE with 4/9/16 beams/stage offers $\simeq$ 3.3 - 4.75 - 4.95 bits/s/Hz.

5.3 Simulation Results Summary

The figures in this chapter show that we have basically achieved the initial goal of the thesis. In almost all cases, given a fixed IA time, Slepian beams achieve higher rate/SINR. Similarly, given a fixed rate/SINR, the IA time is shorter with Slepian beams. Furthermore, for some antenna configurations, Slepian achieves higher rate/SINR and shorter IA time than DFT, at the same time. In addition, in the case of a system with high interference, the benefit becomes larger than for a system with low interference.

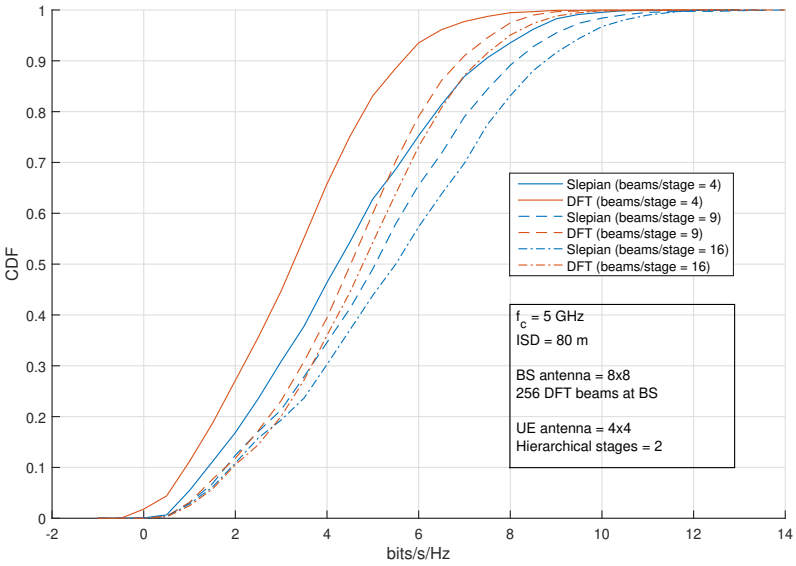

Figure 5.12: CDF of ergodic spectral efficiency of Slepian/DFT beams at the UE and 256 DFT beams at the BS, at downlink f_c = 5 GHz.

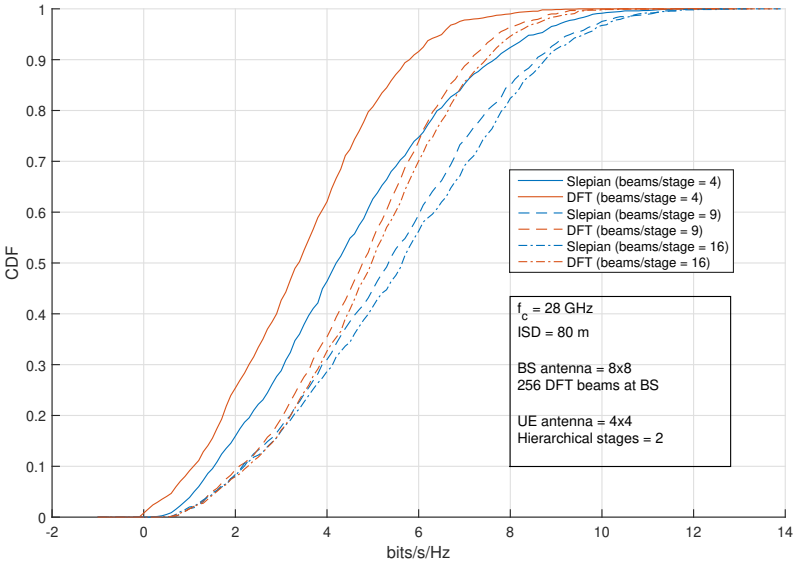

Figure 5.13: CDF of ergodic spectral efficiency of Slepian/DFT beams at the UE and 256 DFT beams the BS, at downlink f_c = 28 GHz.

Chapter 6

Conclusion and Future Work

6.1 Conclusion

Key challenges for the feasibility of 5G mmWave cellular systems are the rapid channel dynamics and the need to maintain alignment between the communication end-points. In this regard, it is important to properly design efficient initial access and tracking procedures, to periodically identify the optimal beam pair with which a base station and a user equipment communicate [27].

In this thesis, the approach of designing a beam that targets a region instead of a single direction is employed. Such a beam gives faster initial access and reduces overhead on the tracking procedure. Based on that, we proposed the Slepian beam that concentrates the maximum possible beamforming gain inside a target region, consequently minimizes the gain outside since the total gain energy is fixed. This increases the average gain that amplifies the desired signal, as well as mitigates interference signals that come from outside the target region. Properties of the Slepian beam are discussed, which show how the beam behaves when the target region is a single direction, the whole region or in between. Squared error as a metric is proposed and used as a criteria for selection of appropriate parameters that generate a beam pattern shape closer to an ideal beam pattern shape. A closed form expression for the squared error is given that makes the calculation tractable. Various codebooks with different sizes that use the Slepian beam, in conjunction with iterative/hierarchical searching algorithm are designed and tested in the *System Simulator*. The effect of the radiation pattern on the mean capacity is analyzed, and upper/lower bounds of the mean capacity in addition to an approximation are formulated. The formula of the capacity approximation shows that the Slepian beam or a generalized Slepian beam are the solutions to its maximization problem.

The proposed analysis supports that the Slepian beam performs better than widely used beams (compared against DFT, Binomial and Dolph-Chebyshev), especially in the presence of interference. This is explained as Slepian beam maximizes the directivity gain energy inside the angular sector where the desired signal is expected to come from, and minimizes it outside, mitigating any undesired signal(s). The gain in capacity/SINR differs depending on the antenna configuration at both the UE and BS. However, in general it is significant compared with the DFT and less significant for Dolph-Chebyshev. Simulation results also verify the same conclusion, showing that using the Slepian codebook at UE and/or BS

achieves higher SINR and data rates compared to the DFT codebook. Moreover, when using the Slepian codebook, both exhaustive and hierarchical searching algorithms roughly perform the same. In that case, using hierarchical is preferred because it significantly reduces the IA time. This gain obtained using the Slepian codebook is the initial goal of this thesis. The gain can be expressed in any of the following two equivalent statements:

- Faster IA time given a certain SINR/rate target.
- Larger SINR/rate given a certain IA time.

Simulation results show that in highly interfered network, the gap in performance between the Slepian codebook and DFT codebook is larger. This means that the Slepian codebook is especially suitable in the presence of high interference.

6.2 Future Work

Some research points may be considered as future work:

- As mentioned in item 2 in the list showen in Subsection 3.2.2, the weighting vectors may be re-generated in the angular domain by numerically integrating the matrix given in (3.7) at certain boundaries, which depends on the decided codebook size (number of entries and number of stages). This will generate beams in the angular domain that describe the real physical space.
- As shown in Figure 4.5, Slepian beam using the width W that maximizes the approximation performs better than the DFT and Dolph-Chebyshev, but the Slepian maximum performance happens at another width (let's call it W^{opt}) shifted from W. The value of the shift is expected to depend on;
  - Standard deviation of the radiation pattern (how flat the radiation pattern is) inside signal region S_R, as well as interference region I_R.
  - Signal power P_s as it directly multiplies the variable S_R, and interference power P_I as it directly multiplies the variable I_R.

  a study on how to calculate/approximate this shift can lead to better selection of parameter W.
- Is the optimal Slepian beam (using W^{opt}) the beam that ultimately maximizes capacity and achieves best performance for a certain number of antenna elements? Or is there some other beam(s) that can perform better than the Slepian beam? This is still an open question that may be interesting to do further studies in.
- Further evaluate the Slepian codebook gain with other channel models and simulation scenarios.

Appendix A

Integration of the Square of a Radiation Pattern in the Phase Domain

For more readability, the subscript ($_v$) denoting *vertical* is removed here. However, the same procedure applies to both vertical and horizontal dimensions.

$$
\begin{aligned}
\textbf{Int} &= \int_{-1}^{1} \Big(G(s;\mathbf{v})\Big)^2 ds = \int_{-1}^{1} \left(\left|\mathbf{v}^H \mathbf{a}(s)\right|^2\right)^2 ds \\
&= \int_{-1}^{1} \Bigg(\Big(v_0^* + v_1^* e^{-j\pi s} + v_2^* e^{-2j\pi s} + \cdots + v_{M-1}^* e^{-(M-1)j\pi s}\Big) \\
&\quad \Big(v_0 + v_1 e^{j\pi s} + v_2 e^{2j\pi s} + \cdots + v_{M-1} e^{(M-1)j\pi s}\Big)\Bigg)^2 ds \\
&= \int_{-1}^{1} \Big(v_0^* v_0 + v_0^* v_1 e^{j\pi s} + v_0^* v_2 e^{2j\pi s} + \cdots + v_0^* v_{M-1} e^{(M-1)j\pi s} \\
&\quad + v_1^* v_0 e^{-j\pi s} + v_1^* v_1 + v_1^* v_2 e^{j\pi s} + \cdots + v_1^* v_{M-1} e^{(M-2)j\pi s} \\
&\quad + v_2^* v_0 e^{-2j\pi s} + v_2^* v_1 e^{-j\pi s} + v_2^* v_2 + \cdots + v_2^* v_{M-1} e^{(M-3)j\pi s} \\
&\quad \cdots \\
&\quad + v_{M-1}^* v_0 e^{-(M-1)j\pi s} + v_{M-1}^* v_1 e^{-(M-2)j\pi s} + v_{M-1}^* v_2 e^{-(M-3)j\pi s} + \ldots \\
&\quad + v_{M-1}^* v_{M-1}\Big)^2 ds
\end{aligned}
$$

It can be seen that any exponential term will vanish after the integration (integration of $e^{\pm j\pi n}$ yields zero for $n = 1, 2, \ldots$), so after expanding the square, one can focus only on terms that are free of exponential terms.

$$
\begin{aligned}
\textbf{Int} &= \int_{-1}^{1} \Big(v_0^* v_0 v_0 v_0^* + v_0^* v_0 v_1 v_1^* + v_0^* v_0 v_2 v_2^* + \cdots + v_0^* v_0 v_{M-1} v_{M-1}^* \\
&\quad + v_0^* v_1 v_0 v_1^* + v_0^* v_1 v_1 v_2^* + v_0^* v_1 v_2 v_3^* + \cdots + v_0^* v_1 v_{M-2} v_{M-1}^* \\
&\quad + v_0^* v_2 v_0 v_2^* + v_0^* v_2 v_1 v_3^* + v_0^* v_2 v_2 v_4^* + \cdots + v_0^* v_2 v_{M-3} v_{M-1}^* \\
&\quad \cdots \\
&\quad + v_0^* v_{M-1} v_0 v_{M-1}^*\Big) ds
\end{aligned}
$$

By observing the sequence, one can write the general formula as below

$$\mathbf{Int} \quad = \quad 2\left(\sum_{a=0}^{M-1} v_a^* \sum_{b=0}^{M-1} v_b \sum_{c=|a-b|}^{M-1} v_c . v_{c-|a-b|}^*\right) \tag{A.1}$$

where the 2 comes from integrating all the constants from -1 to 1.

Appendix **B**

Integration of the Inverse of a Radiation Pattern in the Phase Domain

This appendix shows the evaluation of the expectation of an inverse of a radiation pattern $\mathbb{E}\{\frac{1}{S_R}\}$ for a uniform distribution of s of the incoming signal, which is needed to integrate (4.8) and (4.9).

$$\textbf{Int} = \int_{-W}^{W} \frac{1}{\mathbf{v}^H \mathbf{a}(s)\mathbf{a}^H(s)\mathbf{v}} ds$$

To integrate this, the number of elements should be known, giving - for real weights - a rational function of terms of $(\cos(s))$, however s does not appear explicitly. This can be reduced to an integral of a rational function of t using variable substitution [28] as follows

$$t = \tan(kd\frac{s}{2}), \qquad ds = \frac{2}{kd(1+t^2)}dt, \qquad \cos(kds) = \frac{1-t^2}{1+t^2}$$

Similarly, using trigonometric identities

$$\begin{aligned}
\cos(2kds) &= \frac{1-6t^2+t^4}{(1+t^2)^2} \\
\cos(3kds) &= \frac{1-15t^2+15t^4-t^6}{(1+t^2)^3} \\
\cos(4kds) &= \frac{1-28t^2+70t^4-28t^6+t^8}{(1+t^2)^4} \\
&\vdots
\end{aligned}$$

and the new integration boundaries will be $\pm B = \pm\tan(kd\frac{W}{2})$. Finally, this rational function of t with real coefficients can be integrated in terms of rational functions, logarithm functions and arctangent functions.
Example for $(M = 3)$

$$\begin{aligned}
\textbf{Int} &= \int_{-W}^{W} \frac{1}{\mathbf{v}^H \mathbf{a}(s)\mathbf{a}^H(s)\mathbf{v}} ds \quad | M = 3 \\
&= \int_{-W}^{W} \frac{1}{1+(2v_0v_1+2v_1v_2)\cos(kds)+(2v_0v_2)\cos(2kds)} ds
\end{aligned}$$

let $c_1 = 2v_0v_1 + 2v_1v_2$, and $c_2 = 2v_0v_2$

$$\begin{aligned}
\textbf{Int} &= \int_{-B}^{B} \frac{1}{1 + c_1\frac{1-t^2}{1+t^2} + c_2\frac{1-6t^2+t^4}{(1+t^2)^2}} \cdot \frac{2}{kd(1+t^2)} dt \\
&= \int_{-B}^{B} \frac{(1+t^2)}{(1+t^2)^2 + c_1(1-t^2)(1+t^2) + c_2(1-6t^2+t^4)} \cdot \frac{2}{kd} dt \\
&= \int_{-B}^{B} \frac{(1+t^2)}{(1+2t^2+t^4) + c_1(1-t^4) + c_2(1-6t^2+t^4)} \cdot \frac{2}{kd} dt \\
&= \int_{-B}^{B} \frac{(1+t^2)}{(1+c_1+c_2) + (2-6c_2)t^2 + (1-c_1+c_2)t^4} \cdot \frac{2}{kd} dt
\end{aligned}$$

$$\begin{aligned}
\text{let } a &= 1 + c_1 + c_2 \\
b &= 2 - 6c_2 \\
c &= 1 - c_1 + c_2 \\
r &= \sqrt{b^2 - 4ac}
\end{aligned}$$

$$= \frac{4}{kd} \cdot \frac{\frac{r-b+2c}{\sqrt{b-r}} \tan^{-1}\left(\sqrt{\frac{2c}{b-r}} \tan(kd\frac{W}{2})\right) + \frac{r+b-2c}{\sqrt{b+r}} \tan^{-1}\left(\sqrt{\frac{2c}{b+r}} \tan(kd\frac{W}{2})\right)}{(\sqrt{2c})r}$$

Appendix C

Mean Capacity Upper Bound of the DFT Beam in the Phase Domain

In (4.8), if a DFT is used instead of the Slepian beam and in the case of no interference, the expectation across the radiation pattern inside the signal region for the uniform distribution of the phase s of the incoming signal can be calculated as below

$$\begin{aligned}
\mathbb{E}\{S_{R_{DFT}}\} &= \frac{1}{2W}\frac{1}{\sqrt{M}}\mathbf{1}_{1\times M}\mathbf{A}(W)\frac{1}{\sqrt{M}}\mathbf{1}_{M\times 1} \\
&= \frac{1}{2WM}\sum_{j}\sum_{i}\mathbf{A}_{i,j}(W) \\
&= \frac{1}{2WM}\left(2WM + 4\sum_{i=1}^{M-1}(M-i)\frac{\sin(kdWi)}{kdi}\right) \\
&= 1 + \frac{2}{WM}\sum_{i=1}^{M-1}(M-i)\frac{\sin(kdWi)}{kdi} \qquad \text{(C.1)}
\end{aligned}$$

where (C.1) is the average of a DFT beam bounded by $[-W,W]$ in the phase domain. Substituting in the upper bound equation gives

$$\begin{aligned}
\overline{C}_{DFT} &\leq \log_2\left(1 + \frac{\mathbb{E}\{P_s S_{R_{DFT}}\}}{N_0}\right) \\
&= \log_2\left(1 + \frac{P_s}{N_0}\left(1 + \frac{2}{WM}\sum_{i=1}^{M-1}(M-i)\frac{\sin(kdWi)}{kdi}\right)\right) \qquad \text{(C.2)}
\end{aligned}$$

References

[1] R. Tafazolli, "ETSI Future Mobile Summit", European Telecommunications Standards Institute (ETSI), Tech. Rep., 2013. [Online]. Available: https://docbox.etsi.org/Workshop/2013/201311_FUTUREMOBILESUMMIT/03_UNIofSURREY_TAFAZOLLI.pdf (visited on 05/28/2019).

[2] "i2010 Information Space Innovation & Investment in R&D Inclusion", European Commission, Tech. Rep. IP/07/453, 2007. [Online]. Available: http://europa.eu/rapid/press-release_IP-07-453_en.htm (visited on 05/28/2019).

[3] "Ericsson Mobility Report", Ericsson, Tech. Rep., 2018. [Online]. Available: https://www.ericsson.com/assets/local/mobility-report/documents/2018/ericsson-mobility-report-june-2018.pdf (visited on 05/28/2019).

[4] W. Roh, J. Seol, J. Park, B. Lee, J. Lee, Y. Kim, J. Cho, K. Cheun, and F. Aryanfar, "Millimeter-wave Beamforming as an Enabling Technology for 5G Cellular Communications: Theoretical Feasibility and Prototype Results", *IEEE Communications Magazine*, vol. 52, no. 2, pp. 106–113, 2014, ISSN: 0163-6804. DOI: 10.1109/MCOM.2014.6736750.

[5] M. Shafi, J. Zhang, H. Tataria, A. F. Molisch, S. Sun, T. S. Rappaport, F. Tufvesson, S. Wu, and K. Kitao, "Microwave vs. Millimeter-Wave Propagation Channels: Key Differences and Impact on 5G Cellular Systems", *IEEE Communications Magazine*, vol. 56, no. 12, pp. 14–20, 2018, ISSN: 0163-6804. DOI: 10.1109/MCOM.2018.1800255.

[6] H. T. Friis, "A Note on a Simple Transmission Formula", *Proceedings of the IRE*, vol. 34, no. 5, pp. 254–256, 1946, ISSN: 0096-8390. DOI: 10.1109/JRPROC.1946.234568.

[7] A. A. Pistolkors, "The Radiation Resistance of Beam Antennas", *Proceedings of the Institute of Radio Engineers*, vol. 17, no. 3, pp. 562–579, 1929, ISSN: 0731-5996. DOI: 10.1109/JRPROC.1929.221705.

[8] C. Jeong, J. Park, and H. Yu, "Random Access in Millimeter-wave Beamforming Cellular Networks: Issues and Approaches", *IEEE Communications Magazine*, vol. 53, no. 1, pp. 180–185, 2015, ISSN: 0163-6804. DOI: 10.1109/MCOM.2015.7010532.

[9] M. Giordani, M. Mezzavilla, C. N. Barati, S. Rangan, and M. Zorzi, "Comparative Analysis of Initial Access Techniques in 5G mmWave Cellular Networks", in *2016 Annual Conference on Information Science and Systems (CISS)*, 2016, pp. 268–273. DOI: 10.1109/CISS.2016.7460513.

[10] M. Giordani, M. Mezzavilla, and M. Zorzi, "Initial Access in 5G mmWave Cellular Networks", *IEEE Communications Magazine*, vol. 54, no. 11, pp. 40–47, 2016, ISSN: 0163-6804. DOI: 10.1109/MCOM.2016.1600193CM.

[11] L. Wei, Q. Li, and G. Wu, "Exhaustive, Iterative and Hybrid Initial Access Techniques in mmWave Communications", in *2017 IEEE Wireless Communications and Networking Conference (WCNC)*, 2017, pp. 1–6. DOI: 10.1109/WCNC.2017.7925666.

[12] J. Song, J. Choi, and D. J. Love, "Common Codebook Millimeter Wave Beam Design: Designing Beams for Both Sounding and Communication With Uniform Planar Arrays", *IEEE Transactions on Communications*, vol. 65, no. 4, pp. 1859–1872, 2017, ISSN: 0090-6778. DOI: 10.1109/TCOMM.2017.2665497.

[13] S. Sun, T. S. Rappaport, R. W. Heath, A. Nix, and S. Rangan, "Mimo for Millimeter-wave Wireless Communications: Beamforming, Spatial Multiplexing, or both?", *IEEE Communications Magazine*, vol. 52, no. 12, pp. 110–121, 2014, ISSN: 0163-6804. DOI: 10.1109/MCOM.2014.6979962.

[14] O. E. Ayach, S. Rajagopal, S. Abu-Surra, Z. Pi, and R. W. Heath, "Spatially Sparse Precoding in Millimeter Wave MIMO Systems", *IEEE Transactions on Wireless Communications*, vol. 13, no. 3, pp. 1499–1513, 2014, ISSN: 1536-1276. DOI: 10.1109/TWC.2014.011714.130846.

[15] A. Alkhateeb, O. El Ayach, G. Leus, and R. W. Heath, "Channel Estimation and Hybrid Precoding for Millimeter Wave Cellular Systems", *IEEE Journal of Selected Topics in Signal Processing*, vol. 8, no. 5, pp. 831–846, 2014, ISSN: 1932-4553. DOI: 10.1109/JSTSP.2014.2334278.

[16] TR38.901, *Study on Channel Model for Frequencies from 0.5 to 100 GHz*, 15.0.0, 3GPP, 2018. [Online]. Available: https://portal.3gpp.org/desktopmodules/Specifications/SpecificationDetails.aspx?specificationId=3173 (visited on 05/28/2019).

[17] M. Gustafsson, "ETEN10:7 Antenna Technology, Array Antennas I", Department of Electrical and Information Technology, LTH, Lund University, Lecture notes 7, 2017. [Online]. Available: https://www.eit.lth.se/course/eten10 (visited on 05/28/2019).

[18] ——, "ETEN10:8 Antenna Technology, Array Antennas II, Pattern Synthesis", Department of Electrical and Information Technology, LTH, Lund University, Lecture notes 8, 2017. [Online]. Available: https://www.eit.lth.se/course/eten10 (visited on 05/28/2019).

[19] M. Giordani, M. Polese, A. Roy, D. Castor, and M. Zorzi, "A Tutorial on Beam Management for 3GPP NR at mmWave Frequencies", *IEEE Communications Surveys Tutorials*, vol. 21, no. 1, pp. 173–196, 2019, ISSN: 1553-877X. DOI: 10.1109/COMST.2018.2869411.

[20] S. Hur, T. Kim, D. Love, J. V. Krogmeier, T. A. Thomas, and A. Ghosh, "Millimeter Wave Beamforming for Wireless Backhaul and Access in Small Cell Networks", *IEEE Transactions on Communications*, vol. 61, Jun. 2013. DOI: 10.1109/TCOMM.2013.090513.120848.

[21] D. Slepian and H. O. Pollak, "Prolate Spheroidal Wave Functions, Fourier Analysis and Uncertainty — I", *The Bell System Technical Journal*, vol. 40, no. 1, pp. 43–63, 1961, ISSN: 0005-8580. DOI: 10.1002/j.1538-7305.1961.tb03976.x.

[22] D. Slepian, "Prolate Spheroidal Wave Functions, Fourier Analysis, and Uncertainty — V: the Discrete Case", *The Bell System Technical Journal*, vol. 57, no. 5, pp. 1371–1430, 1978, ISSN: 0005-8580. DOI: 10.1002/j.1538-7305.1978.tb02104.x.

[23] D. Kapetanovic, "Beam Codebook Evaluations with System Simulation", Huawei Technologies Sweden AB (Huawei Lund Research Center), Emdalavägen 10, 22369 Lund Sweden, Internal Report, 2018, Un-Published.

[24] F. Rusek, "EITN10:1 Matrix and Probability Theory", Department of Electrical and Information Technology, LTH, Lund University, Lecture notes 1, 2018. [Online]. Available: https://www.eit.lth.se/course/eitn10 (visited on 05/28/2019).

[25] A. Paulraj, R. Nabar, and D. Gore, *Introduction to Space-Time Wireless Communications*. CAMBRIDGE UNIVERSITY PRESS, 2008, ch. 4, ISBN: 978-1-107-44741-7. DOI: www.cambridge.org/9780521065931.

[26] D. Kapetanovic, "*System Simulator* Manual", Huawei Technologies Sweden AB (Huawei Lund Research Center), Emdalavägen 10, 22369 Lund Sweden, Internal Document, 2019.

[27] M. Giordani, M. Polese, A. Roy, D. Castor, and M. Zorzi, "Standalone and Non-Standalone Beam Management for 3GPP NR at mmWaves", *IEEE Communications Magazine*, vol. 57, no. 4, pp. 123–129, 2019, ISSN: 0163-6804. DOI: 10.1109/MCOM.2019.1800384.

[28] A. Jeffrey, "Indefinite Integrals of Trigonometric Functions", in *Handbook of Mathematical Formulas and Integrals*, 3rd ed. Elsevier Inc., 2004, ch. 9, p. 197, ISBN: 978-0-12-382256-7. DOI: https://doi.org/10.1016/B978-0-12-382256-7.X5000-3.